Article

One Earth

Global flux of perfluoroalkyl acids from glaciers in a warming climate

Graphical abstract

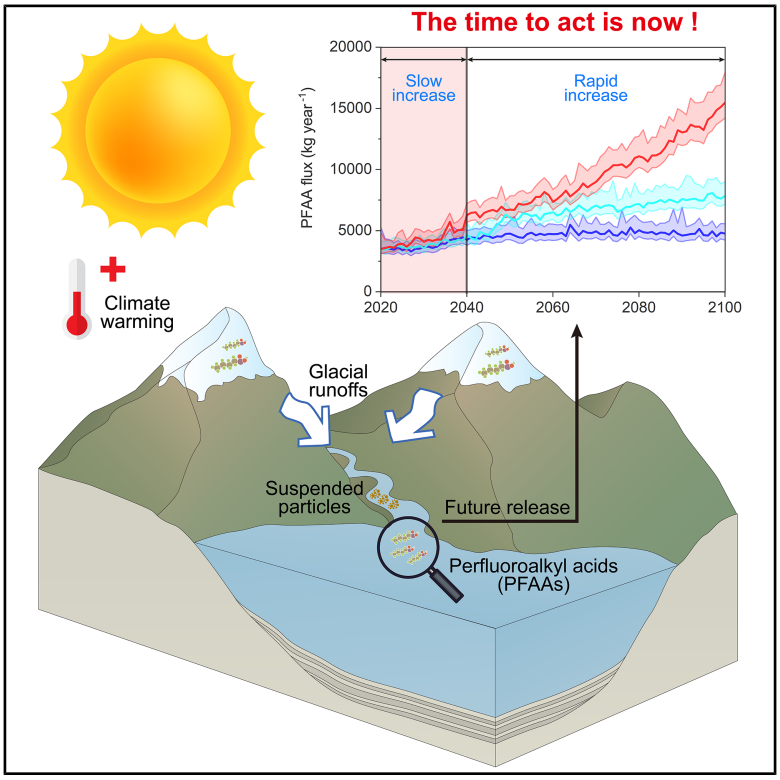

Highlights

- Global glacial release flux of PFAAs is estimated to be about 3,500 kg per year
- PFAAs carried in suspended particles in glacial meltwater should not be ignored
- Arctic fjords and glaciers in the southern Tibetan Plateau are of highest concern
- The release flux of PFAAs in Arctic and Asian glaciers will increase exponentially

Authors

Yunqiao Zhou, Boyuan Hu, Xiaoping Wang, ..., Dongfeng Li, Kevin C. Jones, Derek C.G. Muir

Correspondence

wangxp@itpcas.ac.cn (X.W.), jjfu@rcees.ac.cn (J.F.)

In brief

Global warming is accelerating the release of perfluoroalkyl acids (PFAAs) from melting glaciers, yet their release fluxes remain poorly quantified on a global scale. This study combines field and literature data with machine learning and a glacier mass balance model to estimate PFAA fluxes from glaciers worldwide. By quantifying fluxes in both dissolved and particle-bound phases under three warming scenarios, the study identifies regional hotspots of concern and defines a critical time window for action. These findings shed light on PFAA cycling in the cryosphere and inform policy responses.

Zhou et al., 2025, One Earth *8*, 101453
December 19, 2025
https://doi.org/10.1016/j.oneear.2025.101453

CellPress

Please cite this article in press as: Zhou et al., Global flux of perfluoroalkyl acids from glaciers in a warming climate, One Earth (2025), https://doi.org/10.1016/j.oneear.2025.101453

One Earth

CellPress

Article

Global flux of perfluoroalkyl acids from glaciers in a warming climate

Yunqiao Zhou,[1,13] Boyuan Hu,[2,3,13] Xiaoping Wang,[1,4,14,*] Jianjie Fu,[2,3,5,*] Ian T. Cousins,[6] Xi Bi,[7] Lanxiang Wang,[1,4] Mengke Chen,[1,4] Chuanfei Wang,[1] Huike Dong,[1] Shaoting Ren,[1] Zimeng Wang,[8] Taicheng An,[9] Dongfeng Li,[10] Kevin C. Jones,[11] and Derek C.G. Muir[12]

[1]State Key Laboratory of Tibetan Plateau Earth System, Resources and Environment, Institute of Tibetan Plateau Research, Chinese Academy of Sciences, Beijing 100101, China
[2]State Key Laboratory of Environmental Chemistry and Ecotoxicology, Research Center for Eco-Environmental Sciences, Chinese Academy of Sciences, Beijing 100085, China
[3]School of Environment, Hangzhou Institute for Advanced Study, University of Chinese Academy of Sciences, Hangzhou 310024, China
[4]University of Chinese Academy of Sciences, Beijing 100049, China
[5]School of Ecology and Environment, Tibet University, Lhasa 850000, China
[6]Department of Environmental Science, Stockholm University, 10691 Stockholm, Sweden
[7]School of Economics and Management, China University of Petroleum (Beijing), Beijing 102249, China
[8]Department of Environmental Science and Engineering, Fudan University, Shanghai 200433, China
[9]School of Environmental Science and Engineering, Institute of Environmental Health and Pollution Control, Guangdong University of Technology, Guangzhou 510006, China
[10]Key Laboratory for Water and Sediment Sciences, Ministry of Education, College of Environmental Sciences and Engineering, Peking University, Beijing 100871, China
[11]Lancaster Environment Centre, Lancaster University, LA1 4YQ Lancaster, UK
[12]Aquatic Contaminants Research Division, Environment & Climate Change Canada, Burlington, ON L7S 1A1, Canada
[13]These authors contributed equally
[14]Lead contact
*Correspondence: wangxp@itpcas.ac.cn (X.W.), jjfu@rcees.ac.cn (J.F.)
https://doi.org/10.1016/j.oneear.2025.101453

SCIENCE FOR SOCIETY Perfluoroalkyl acids (PFAAs) are industrial pollutants that circulate globally and accumulate in cold regions, including glaciers. They pose significant ecological and human health risks and are known for their extreme persistence. As glaciers melt, a process accelerated by global warming, PFAAs previously stored in ice are released into the environment. Our study quantifies PFAA fluxes from global glaciers, identifying key release hotspots including the Arctic and South and Central Asia. These hotspots include important fisheries in Arctic fjords and drinking water supplied from Himalayan glaciers. Controlling PFAA pollution in these regions will thus require reducing PFAA pollution at the source and mitigating global warming to slow glacial melting. This calls for an interdisciplinary collaboration bringing together scientists, local communities, and policymakers to develop effective mitigation strategies on these dual threats.

SUMMARY

Climate warming is accelerating glacier melting, releasing human-made chemicals that have been trapped in glaciers for decades. Among these are perfluoroalkyl acids (PFAAs), highly persistent and toxic pollutants that threaten aquatic ecosystems, fisheries, and human health. Despite global efforts to curb PFAA emissions, their continued release from melting glaciers represents a legacy source that remains unquantified on a global scale. Here, we combine field and literature data with machine learning and a glacial mass balance model to estimate current and future PFAA fluxes via both dissolved and particle-bound phases. We find that global glaciers release approximately 3,500 kg of PFAAs annually, with suspended particles contributing around 12% of this amount. Projected trends suggest future release potential will rapidly boom through 2040 under extreme climate warming. These findings fill a critical gap in the global PFAA budget and underscore the urgency of coordinated action on both legacy pollutant management and climate mitigation.

Please cite this article in press as: Zhou et al., Global flux of perfluoroalkyl acids from glaciers in a warming climate, One Earth (2025), https://doi.org/10.1016/j.oneear.2025.101453

INTRODUCTION

In the Anthropocene, chemical pollution has become a defining challenge as novel entities for planetary health.[1–3] Among these, per- and polyfluoroalkyl substances (PFASs), known as "forever chemicals" due to their extreme persistence, have attracted widespread attention.[4,5] PFASs are a large class of human-made chemicals that have been widely used in industrial and consumer products since the mid-20th century.[6] Perfluoroalkyl acids (PFAAs) are the best-studied subgroup of PFASs, including compounds listed for phase-out under the Stockholm Convention due to a series of adverse effects.[7,8] Alarmingly, even in remote regions, the concentrations of perfluorooctanoic acid (PFOA) in rainwater greatly exceed health advisory levels (4 pg L^{-1}),[9] indicting that the planetary boundary for PFAA pollution has been exceeded worldwide.[10]

Glaciers in the remote cryosphere are critical reservoirs for PFAAs. PFAAs can undergo long-range atmospheric transport and subsequently deposit onto glacial surfaces through both dry and wet deposition processes due to the cold-trapping effect.[11] Measurable concentrations of PFAAs have been detected in glaciers in the Arctic,[12] Antarctica,[13] and high-altitude alpine regions,[14,15] ranging from hundreds to thousands of picograms per liter. As "forever chemicals," PFAAs can persist in glaciers for decades, even after their primary emissions are controlled,[16,17] posing long-term threats to fragile ecosystems, particularly in sensitive regions such as the Arctic and the Tibetan Plateau.

Previously trapped PFAAs in glaciers are being released under the warming climate,[18,19] creating an emerging threat to proglacial ecosystems. Signals of PFAA meltwater sources have been identified in the contaminant profiles of sediment cores and in the biota from proglacial environments,[20,21] indicating the re-release of these previously accumulated chemicals. Once released, PFAAs can undergo biomagnification via the food chain from benthic invertebrates to top predators,[22,23] thereby threatening aquatic diversity, fisheries, and even human health. For example, high concentrations (~500 ng mL^{-1}) were found in blood serum from East Greenland Inuit who rely on traditional marine food, despite relatively low environmental concentrations (0.0005 ng mL^{-1}).[24]

Despite growing recognition of this emerging threat, several knowledge gaps remain. Most notably, we lack a comprehensive estimate of the magnitudes and spatial patterns of PFAA fluxes from glaciers on a global scale. Existing studies are limited to a few sampling sites. To date, only two studies report the release flux of PFAAs downstream: one reporting an annual flux of 1.6 ± 0.7 kg in the Canadian High Arctic,[25] and another estimating about 0.5 kg $year^{-1}$ from a single glacier on the central Tibetan Plateau.[26] The lack of global flux data limits our understanding of how glacial melt contributes to global PFAA budget and hinders the identification of pollution hotspots.

Furthermore, current assessments of PFAA transport focus on dissolved phase while overlooking the contribution of suspended particles generated through glacial erosion and permafrost thawing.[17,18] These suspended particles, mobilized at increasing rates under accelerated glacial melting, may serve as important vectors for PFAAs, especially for more toxic long-chain compounds.[19,20] As climate warming accelerates erosion and sediment mobilization, the omission of particle-bound transport may result in underestimation of total PFAA fluxes and associated health risks.

Here, we address these critical knowledge gaps by quantifying current and future flux of PFAAs released from glaciers worldwide via both dissolved phase and particle-bound particles. Our analysis includes a global dataset of field data from Tibetan glaciers and literature data from global glaciers, the application of machine learning (ML) and a glacial mass balance model, and the prediction of release fluxes through the end of the 21st century. Our findings reveal that approximately 3,500 kg of PFAAs are released from global glaciers per year, with the Arctic and South and Central Asia identified as major export regions. Suspended particles contribute around 12% of the total flux, highlighting their non-negligible impact. The release flux is projected to increase rapidly through 2040, leaving a narrow time window for effective actions. Our estimates and predictions are crucial for a better understanding of the role of glacial melting on PFAA cycling in the global cryosphere.

RESULTS

Methods summary

To evaluate the global flux of PFAAs from glaciers, we posed three research questions. (1) What are the magnitudes and spatial patterns of PFAA release fluxes from glaciers on a global scale? (2) What is the role of the particle-bound phase in total PFAA export? (3) How might these fluxes change under future climate scenarios?

To answer these questions, we first conducted field sampling on seven glaciers across the Tibetan Plateau, measuring 13 individual PFAAs in both dissolved phase and suspended particles. These field data were integrated into a global dataset comprising 739 samples from 49 glaciers across eight major glacial regions worldwide. Due to the scarcity of concentrations in suspended particles, we developed predictive models for log-transformed particle-water partition coefficients ($\log K_d$), using both traditional curve-fitting and ML approaches. $\log K_d$ values were predicted based on environmental parameters (e.g., water temperature and particulate organic carbon) and molecular descriptors of PFAAs. The best-performing ML model was finally selected from multiple candidates based on its accuracy and stability.

We then coupled the predicted $\log K_d$ with glacial runoff volumes derived from glacial mass balance model to quantify annual release flux of PFAAs via both dissolved phase and suspended particles. For regions with high export fluxes, we further identified pollution hotspots using threshold-based spatial analysis of PFAA concentrations in water and sediment. Finally, we integrated climate projections under three shared socioeconomic pathways (SSP126, SSP245, and SSP585) to simulate global glacial PFAA exports from 2020 to 2100. This integrative framework enables a comprehensive assessment of current and future glacier-sourced PFAA fluxes on a global scale.

PFAAs in glacial meltwaters of the Tibetan Plateau

To characterize the current status of PFAAs in high-altitude glacial regions, we measured 13 individual PFAAs (Table S1) in meltwater and associated suspended particles from seven glacier regions across the Tibetan Plateau. Figure 1 illustrates the upstream-to-downstream arrangement of sampling sites, along with average

Please cite this article in press as: Zhou et al., Global flux of perfluoroalkyl acids from glaciers in a warming climate, One Earth (2025), https://doi.org/10.1016/j.oneear.2025.101453

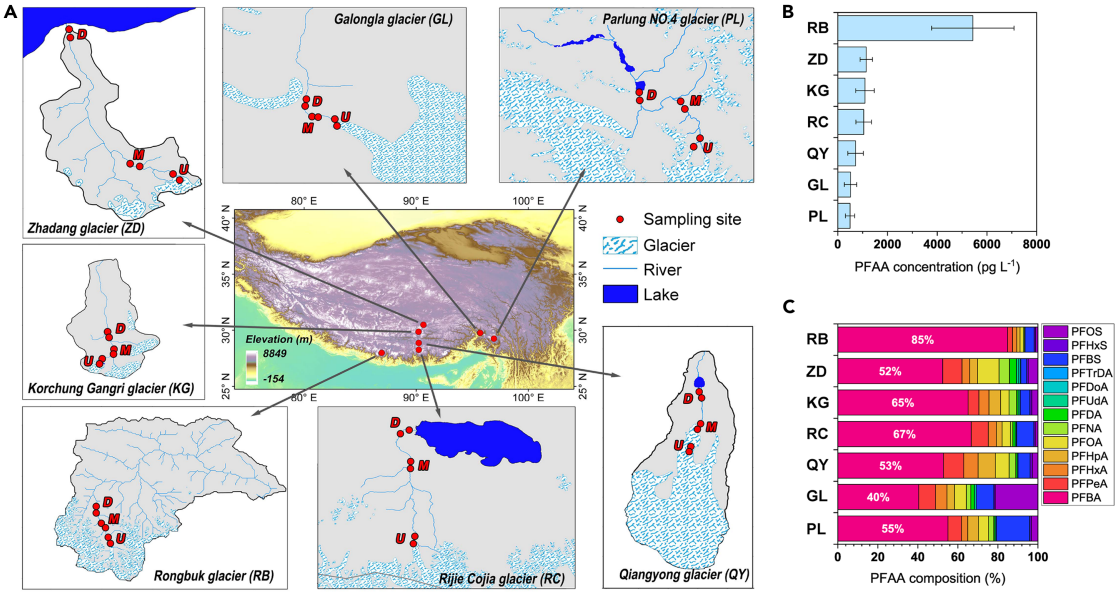

Figure 1. Sampling sites and average concentrations and compositions of 13 perfluoroalkyl acids in seven glacial regions of the Tibetan Plateau

Sampling sites from upstream to downstream (A) and average concentrations (B) and compositions (C) of 13 perfluoroalkyl acids (PFAAs) in seven glacial regions of the Tibetan Plateau. Error bars in (B) represent the standard deviation of all PFAA concentrations within each glacial region. The seven glacial regions are RB, Rongbuk glacier; KG, Korchung Gangri glacier; ZD, Zhadang glacier; GL, Galongla glacier; PL, Parlung No. 4 glacier; QY, Qiangyong glacier; and RC, Rijie Cojia glacier. U, M, and D in (A) represent upstream, midstream, and downstream sites, respectively.

concentrations and compositions of Σ_{13}PFAAs. The highest concentration (5,430 pg L^{-1}) was observed in the Rongbuk glacial region of Mount Everest (Figure 1B), while concentrations at the other sites were generally below 1,200 pg L^{-1}. Across all sites, short-chain PFAAs, consisting of <C8 perfluoroalkyl carboxylic acids (PFCAs) and <C6 perfluoroalkyl sulfonic acids (PFSAs), dominated the PFAA profiles, accounting for 68%–96% of the total concentrations (Figure 1C).

PFAAs released through glacier ablation can be transported downstream either in the dissolved phase or adsorbed onto suspended particles. We found that concentrations of most short-chain PFAAs in the dissolved phase increased from upstream to downstream sites (Figure S1), likely due to their higher solubility and mobility in water. In contrast, long-chain PFAAs (≥C8 PFCAs and ≥C6 PFSAs) adsorbed onto suspended particles exhibited the opposite trend, with their concentrations decreasing from upstream to downstream (Figure S1). In other words, long-chain PFAAs associated with suspended particles tend to accumulate in the headwater regions. The opposing spatial trends of PFAA concentrations during transport (Figure S1) indicate the crucial need for accurate PFAA concentrations in both dissolved and particle-bound phase in glacier-fed systems.

Occurrence of PFAAs in global glacial regions

To place Tibetan data in a broader context, we compiled a global database of Σ_{13}PFAA concentrations from more than 49 glaciers, including field data from this study (n = 59) and previous research (n = 680) (Table S2). Figure 2 presents the locations of these glacial sites across eight major glacial regions, and corresponding average Σ_{13}PFAA concentrations (bold numbers) at each region. Pie charts depict the relative composition of individual PFAAs at each region.

Across the global dataset, PFAA concentrations in glacial meltwater (Table S3) ranged from several hundred to several thousand picograms per liter, exhibiting distinct regional variation (Figure 2). Although the data exhibited fluctuations, the average concentrations of Σ_{13}PFAAs were relatively high (4,486 pg L^{-1}) in glacial regions in Arctic Canada (ACG) (Figure 2) (i.e., Lake Hazen watershed, see Table S2), and those near the Greenland Sea exhibited much lower levels (297 pg L^{-1}). Similar to the Tibetan Plateau, short-chain PFAAs predominated in most regions, accounting for 62%–80% of the total concentrations in areas such as ACG, Central Europe (CEG), and South and Central Asia (SCAG) (Figure 2, pie charts).

However, field data on PFAAs associated with suspended particles remain scarce in global glacial regions. To overcome this limitation, we applied the particle-water partition coefficient (K_d) to bridge the field-measured dissolved PFAA concentrations to particle-bound concentrations.

Predicting particle-water partition coefficient

The K_d describes the distribution of PFAAs between the dissolved and particle-bound phases. However, K_d values are highly variable and influenced by environmental parameters and molecular descriptors of PFAAs. Therefore, we selected key influencing factors, including temperature (T_w), particulate organic carbon (POC), log$K_{ow\text{-}ionic}$, and PFAA type, for predicting logK_d. Details on selecting these factors and model validation procedures are provided in the methods section.

Initial attempts to predict logK_d using curve-fitting models yielded limited performance, with coefficients of determination

Please cite this article in press as: Zhou et al., Global flux of perfluoroalkyl acids from glaciers in a warming climate, One Earth (2025), https://doi.org/10.1016/j.oneear.2025.101453

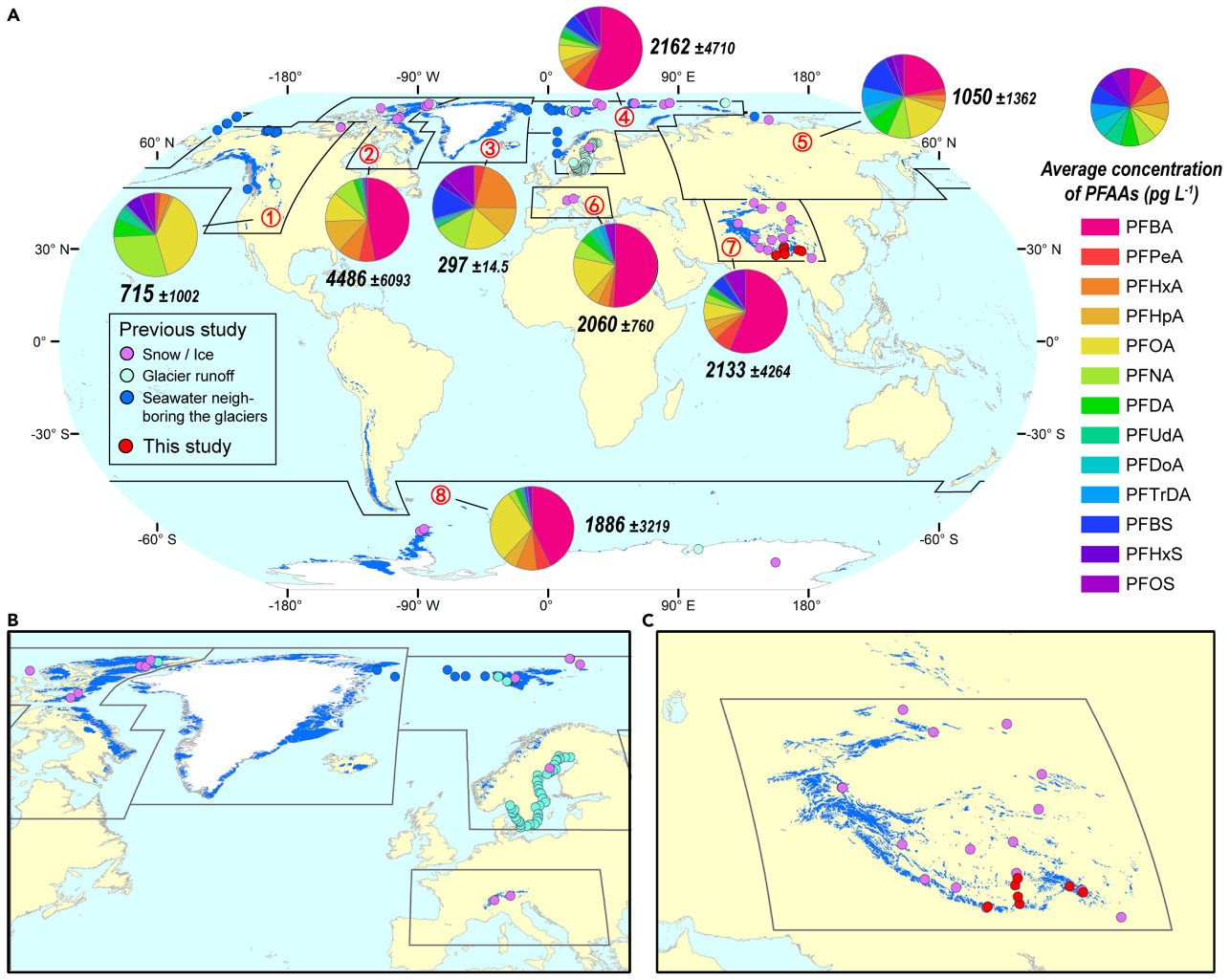

Figure 2. Average concentrations and compositions of 13 perfluoroalkyl acids in eight glacial regions and sampling sites in the Arctic and Asian regions

Average concentrations and compositions of 13 perfluoroalkyl acids (PFAAs) in (A) eight glacial regions and sampling sites in the (B) Arctic and (C) Asian regions. The dots represent sample locations in different glacial regions. Glaciers are shown in blue, ice sheets are shown in white, and the black lines indicate the outlines of different glacial regions from the Randolph Glacier Inventory. The eight glacial regions are ① West Canada and USA (WCUG), ② Arctic Canada (ACG), ③ Greenland ice sheet (GIS), ④ Arctic Europe (AEG), ⑤ North Asia (NAG), ⑥ Central Europe (CEG), ⑦ South and Central Asia (SCAG), and ⑧ Antarctic and Subantarctic ice sheet (AIS). The pie charts represent the composition of PFAAs in each glacial region, and bold numbers present the average concentration and standard deviation of PFAAs. The 13 PFAAs are perfluorobutanoic acid (PFBA), perfluoropentanoic acid (PFPeA), perfluorohexanoic acid (PFHxA), perfluoroheptanoic acid (PFHpA), perfluorooctanoic acid (PFOA), perfluorononanoic acid (PFNA), perfluorodecanoic acid (PFDA), perfluoroundecanoic acid (PFUdA), perfluorododecanoic acid (PFDoA), perfluorotridecanoic acid (PFTrDA), perfluorobutane sulfonic acid (PFBS), perfluorohexane sulfonic acid (PFHxS), and perfluorooctane sulfonic acid (PFOS).

(R^2) ranging from 0.48 to 0.64 (Note S1). To improve prediction accuracy, we developed several ML models, including support vector machines (SVMs), decision trees (DTs), random forests (RFs), and extreme gradient boosting (XGBoost). Among these, the XGBoost model (XGBoost-ML) outperformed others in both explanatory power and stability (R^2 = 0.95 for the training set and Q^2 = 0.85 for the test set). The best-performing XGBoost-ML showed strong agreement with field-measured logK_d for all individual PFAAs in the training set (Figure 3A). Almost all of the predicted logK_d in the test set fell within an order of magnitude (±1 range) of the measured values, except one outlier (Figure 3B, white squares), which was measured with high POC values (up to 10%) (Table S4).

In summary, the XGBoost-ML outperforms traditional curve-fitting methods and other ML models in predicting logK_d. With the combination of model-predicted logK_d with field-measured dissolved PFAA concentrations (Table S2), the concentrations of PFAAs on suspended particles across the eight global glacial regions were calculated. The results are provided in Table S5.

Global fluxes of PFAAs from glaciers

Using dissolved and estimated particle-bound concentrations (Tables S3 and S5) combined with modeled glacial runoff volumes, we quantified the annual release fluxes of individual

Please cite this article in press as: Zhou et al., Global flux of perfluoroalkyl acids from glaciers in a warming climate, One Earth (2025), https://doi.org/10.1016/j.oneear.2025.101453

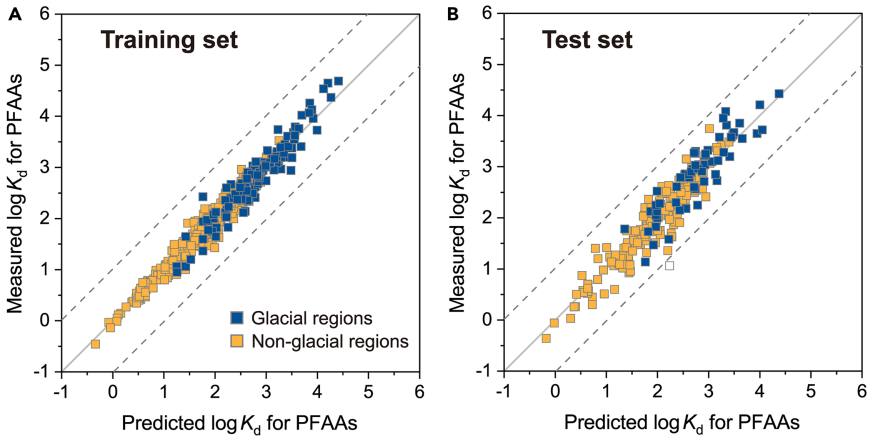

Figure 3. Comparison of the measured logK_d for perfluoroalkyl acids in glacial and non-glacial regions with the predicted logK_d driven from the XGBoost algorithm

(A) The training set and (B) the test set. The blue and yellow squares indicate the ratios of measured logK_d and predicted values that fall within ±1 log unit for samples from glacial and non-glacial regions, respectively. The white square represents the ratio of the measured logK_d and predicted logK_d that falls outside ±1 log unit, with only one datum observed in the non-glacial regions.

PFAAs from eight major glacial regions worldwide, with data listed in Table S6. Table 1 summarizes the release fluxes of Σ_{13}PFAAs via the dissolved phase and suspended particles for each region.

The total estimated global flux of Σ_{13}PFAAs was 3,547 ± 375 kg year^{-1}, with the dissolved phase contributing 3,117 ± 165 kg year^{-1} (~88%) and suspended particles accounting for the remaining 430 ± 210 kg year^{-1} (~12%) (Table 1). In most glacial regions, the contribution of suspended particles remained less than 15%. However, in sediment-rich systems such as the Greenland ice sheet (GIS), suspended particles contributed up to 51% of the total flux, likely due to high particle loads in glacial outflows.

Differences in the chain length of PFAAs influenced release fluxes in dissolved and particle-bound phases. In the dissolved phase, short-chain PFAAs dominated, with an estimated flux of 1,823 ± 97 kg year^{-1}, compared to 1,129 ± 61 kg year^{-1} for long-chain compounds (Table S6). In contrast, the particle-bound phase was enriched in long-chain PFAAs, which contributed 238 ± 63 kg year^{-1}, nearly three times the flux of short-chain compounds (87 ± 14 kg year^{-1}) (Table S6), consistent with their stronger sorption affinities.

Substantial regional variations in total PFAA fluxes were also observed (Table 1). The SCAG region contributed the highest load, with an estimated flux of 1,394 ± 86 kg year^{-1}, accounting for nearly 40% of global glacial PFAA export. This was followed by the ACG (698 ± 48 kg year^{-1}), Arctic Europe (AEG) (564 ± 25 kg year^{-1}), Western Canada and the USA (WCUG) (426 ± 15 kg year^{-1}), and GIS (316 ± 190 kg year^{-1}). Collectively, these five regions represented over 95% of the total global flux. High glacial runoff volumes, ranging from 212 to 547 km^3 year^{-1} (Table 1), and relatively high PFAA concentrations (Figure 1) contributed to their dominant role.

In contrast, smaller glaciers such as those in North Asia (NAG) and Central Europe (CEG) exhibited limited annual PFAA fluxes (<20 kg year^{-1}), due to both lower glacial runoff volumes (Table 1) and moderate PFAA levels (Figure 2). The Antarctic and Subantarctic ice sheet (AIS) also contributed modestly (118 ± 10 kg year^{-1}), consistent with its relatively isolated location from PFAA emission sources.

Priority locations of concern

As mentioned above, the Arctic and SCAG regions present hotspot export zones for PFAA releases from melting glaciers. To further identify the locations of concern that should be prioritized for protection, we compiled the data on PFAAs in water and sediment from these regions (Tables S7 and S8).

The average concentrations of Σ_{13}PFAAs in water (2 ng L^{-1}) and sediments (1 ng g^{-1}) were obtained and served as baselines for assessing priority locations of concern. Levels of concern are based on exceeding the average by one, two, and three times, respectively. Figure 4 illustrates priority locations of concern for PFAAs with relatively high concentrations in water or sediment in the Arctic and SCAG regions. Red circles on the map indicate sites influenced by water, while purple circles represent those influenced by sediment. The higher the concentration of PFAAs, the larger the buffer zone. Detailed locations of each site are available in Tables S7 and S8.

In the Arctic, locations of concern are categorized into four main regions: Svalbard, Arctic Europe, the Canadian Arctic basins, and the Chukchi Sea (Figure 4A). Svalbard exhibits elevated PFAA levels in both water and sediment, indicating a significant overlap in environmental risk. In Arctic Europe, areas of high concern are identified in coastal sediments along the Norwegian Sea and the Barents Sea. Additionally, northern Swedish glaciers are classified as high-concern sites due to high PFAA concentrations in glacial runoffs. In the Canadian Arctic basins, such as Lake Hazen and Lake B35, impacts on local wildlife, including polar bears and Arctic foxes, have been observed in surrounding areas such as Grise Fjord and Arviat (Figure 4A, orange triangle). Meanwhile, sediments near the coast of the Chukchi Sea indicate relatively high environmental risk.

Future release potential under climate warming

Apart from regional impacts, understanding how the release of PFAAs from glaciers change under future climate warming is also imperative. Figures 5A and 5B illustrate the future release potential of Σ_{13}PFAAs from global glaciers in the 21st century via dissolved and suspended-particle phases under three SSP scenarios, i.e., SSP126 (low emissions), SSP245 (intermediate emissions), and SSP585 (high emissions). The release potential refers to a predicted possibility of PFAA fluxes under future climate scenarios.

Under SSP126, the release potential of Σ_{13}PFAAs is expected to remain relatively stable by the end of the 21st century (Figures 5A and 5B, SSP126 scenario). In contrast, under SSP245—and especially under SSP585—the potential Σ_{13}PFAA

Please cite this article in press as: Zhou et al., Global flux of perfluoroalkyl acids from glaciers in a warming climate, One Earth (2025), https://doi.org/10.1016/j.oneear.2025.101453

Table 1. Release fluxes of perfluoroalkyl acids via the dissolved phase and suspended particles from glaciers in eight glacial regions globally, compared with the depositional fluxes

Glacial region	Glacial area (km^2)	Glacial runoff (km^3 $year^{-1}$)	ACSP (mg L^{-1})	Release fluxes (kg $year^{-1}$)				Depositional fluxes of $\sum_{10}$PFCAs estimated by the GEOS-Chem model (kg $year^{-1}$)[27]	
				Dissolved phase[a]	Suspended particles[a]	$\sum_{13}$PFAAs	$\sum_{10}$PFCAs	Minimum	Maximum
WCUG	101,249	400	182	380 ± 8.6 (89%)	46 ± 6.0 (11%)	426 ± 15	388 ± 13	16.9	79.6
ACG	146,016	212	97	683 ± 47 (98%)	14 ± 1.3 (2%)	698 ± 48	683 ± 47	17.5	81.8
GIS	1,718,000	547	881	153 ± 8.4 (49%)	162 ± 181 (51%)	316 ± 190	179 ± 42	96.2	206
AEG	88,498	146	91	520 ± 18 (92%)	44 ± 7.3 (8%)	564 ± 25	330 ± 11	14.2	102
NAG	2,410	7	91	9.1 ± 0.5 (85%)	1.7 ± 0.5 (15%)	11 ± 0.9	8.3 ± 0.6	0.39	2.89
CEG	2,075	9	356	18 ± 0.3 (88%)	2.6 ± 0.1 (12%)	21 ± 0.4	20 ± 0.3	3.32	3.32
SCAG	97,604	352	500	1,244 ± 73 (89%)	151 ± 13 (11%)	1,394 ± 86	1,159 ± 60	151	205
AIS	13,746,463	48	73	109 ± 9.0 (93%)	8.2 ± 1.1 (7%)	118 ± 10	116 ± 10	28.9	220
Total	–	–	–	3,117 ± 165 (88%)	430 ± 210 (12%)	3,547 ± 375	2,884 ± 184	329	900

WCUG, Western Canada and USA; ACG, Arctic Canada; GIS, Greenland ice sheet; AEG, Arctic Europe; NAG, North Asia; CEG, Central Europe; SCAG, South and Central Asia; AIS, Antarctic and Subantarctic ice sheet; ACSP, average concentration of suspended particles in each glacial region reported previously.

The areas of the GIS and AIS were obtained from Pfeffer et al.[28] and Liston and Winther,[29] respectively. The other data are available from the Randolph Glacier Inventory version 6.0 (http://www.glims.org/RGI/). The glacial runoffs of the GIS and AIS are available from Tedesco et al.[30] and Liston and Winther,[29] respectively, with the other data collected from Bliss et al.[31] The depositional fluxes of $\sum_{10}$PFCAs estimated by the GEOS-Chem model represent the average value for 2013–2015; the historical depositional fluxes might be much higher.

[a]Data presented as release fluxes (percentage of total fluxes).

fluxes exhibit increasing trends throughout the century. Under SSP585, the average release fluxes of Σ_{13}PFAAs via the dissolved phase could reach up to ~13,000 kg $year^{-1}$, and those via suspended particles may reach ~2,500 kg $year^{-1}$, which represents a 6-fold increase compared to 2020 levels (Figures 5A and 5B, SSP585 scenario). By 2040, the release potential is expected to be less than double those observed in 2020; however, after 2040, the rate of increase is projected to boom rapidly. These results identify the next 15 years as a critical window for global efforts to mitigate PFAA pollution and combat climate change.

Regionally, under SSP585, ACG and GIS are predicted to experience a nearly 10-fold increase in the release potential of dissolved PFAAs by the end of this century. In contrast, WCUG, AEG, SCAG, and AIS are expected to have about a 2-fold increase (Figure S2). For the suspended-particle phase, the release potential in ACG and GIS is projected to increase by ~8-fold, while WCUG, AEG, SCAG, and AIS are anticipated to experience about a 2-fold increase (Figure S3).

However, these estimates may be conservative, as they assume that the rate of sediment transport—and thus particle-associated PFAA flux—remains constant under future climate warming. Actually, glacial sediment export has already doubled over the past 30 years in regions such as the Arctic coastline and the Himalayas.[33] If this trend continues, doubling every 30 years, the release potential of Σ_{13}PFAAs associated with suspended particles in the Arctic (Greenland) region is expected to undergo an exponential increase, reaching approximately 50-fold above 2020 levels by 2100 under the SSP585 scenario (Figure 5C). In the SCAG region, particle-bound PFAA fluxes are also projected to rise substantially, with a nearly 10-fold increase over the same period (Figure 5D).

DISCUSSION

Although glaciers are increasingly recognized as secondary sources of pollutants, the magnitude and mechanisms of PFAA release, particularly via the particle-bound phase, have remained largely unresolved on a global scale. Our study addresses this gap by providing the first quantitative estimate of both dissolved and particle-bound PFAA releases from glaciers worldwide, revealing that glacial melt can export thousands of kilograms of legacy PFAAs to downstream ecosystems each year, with significant regional and chemical partitioning patterns.

In the following context, we first evaluate limitations of uncertainty in our global PFAA flux estimates. We then assess whether glaciers currently act as net sources or sinks of PFAAs by comparing the global patterns of release and depositional fluxes derived from the GEOS-Chem model. These glacial fluxes were further compared to global PFAA emission inventories to clarify their relative contribution and to identify locations of high concern. Beyond quantification, we explore the potential adverse effects of increased PFAA outflows, particularly the role of particle-bound transport. Finally, we discuss strategies for controlling future PFAA releases from glaciers under climate warming.

Limitations

Several sources of uncertainty may influence the accuracy of our global PFAA flux estimates. First, the limited number of sampled glaciers within each region may not fully capture spatial heterogeneity, potentially introducing bias when extrapolating to the regional scale. Temporal uncertainty also arises due to the seasonal variability of both meltwater runoff[34] and PFAA

Please cite this article in press as: Zhou et al., Global flux of perfluoroalkyl acids from glaciers in a warming climate, One Earth (2025), https://doi.org/10.1016/j.oneear.2025.101453

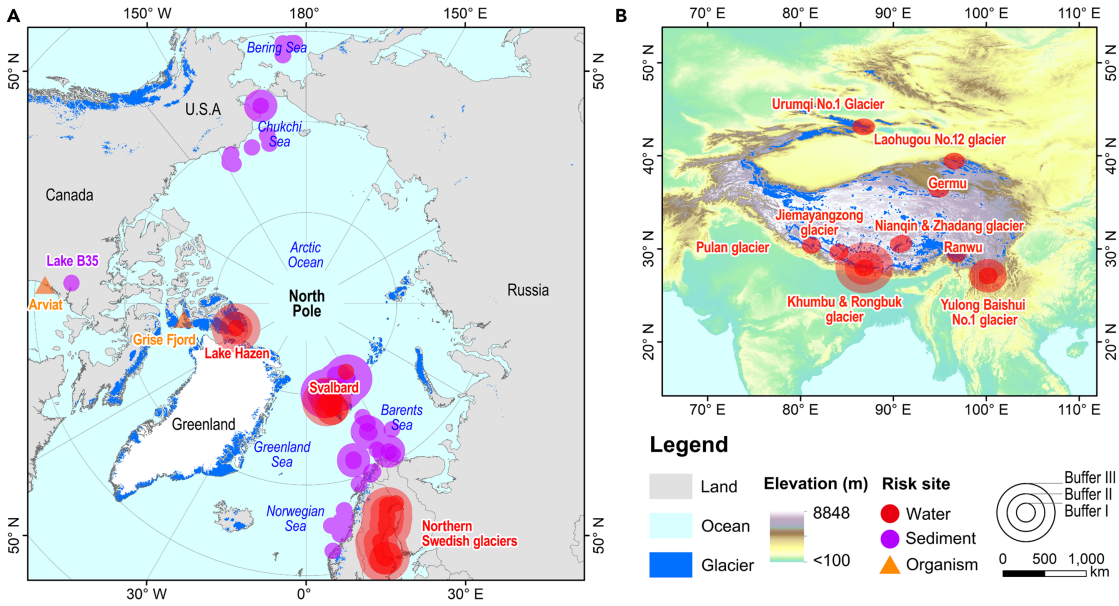

Figure 4. Geographical distribution of perfluoroalkyl acid areas of concern in the Arctic and South and Central Asia

Distribution of perfluoroalkyl acid (PFAA) areas of concern in (A) the Arctic and (B) the South and Central Asia. The red circle and purple circle represent the sites of concern for water and sediment, respectively. The orange triangles mark areas of potential biodiversity loss due to high PFAA levels found in polar bears and Arctic foxes, as reported in previous studies.[32] Detailed data for the buffer zone are provided in Tables S7 and S8, with average concentrations for water and sediment being approximately 2,000 pg/L and 1,000 pg/g, respectively. Buffer zones I, II, and III represent areas where PFAA concentrations in water and sediment exceed the regional average concentration by 1-fold, 2-fold, and more than 3-fold, corresponding to impact zones of 100 km, 200 km, and 300 km, respectively.

concentrations,[19] as most field campaigns were conducted during limited time windows. In some Arctic regions, the scarcity of glacial meltwater data led to the use of PFAA concentrations in adjacent seawater (Table S2), which may underestimate fluxes due to dilution effects. These factors likely contributed to the large standard deviations observed in both PFAA concentrations (Figure 2) and flux estimations (Table 1).

Second, data gaps in key regions remain. In particular, no observational data are currently available for Patagonia and the southern Andes. Glaciers in these regions are among the most rapidly retreating on Earth.[35] This lack of data would lead to an underestimation of global glacier-sourced PFAA fluxes. Moreover, geopolitical dynamics, such as international regulations on PFAA production, industrial substitution of legacy PFAAs, and the geographic relocation of manufacturing facilities, could alter emission patterns over time. However, due to the lack of reliable global models and transparent reporting, the influence of these political and economic factors could not be quantitatively assessed.

Finally, analytical uncertainties also exist. Perfluorobutanoic acid (PFBA), a prevalent short-chain PFAA, has been inconsistently reported in previous studies due to analytical challenges.[36,37] To assess the impact of its exclusion, we recalculated fluxes for Σ_{12}PFAAs (excluding PFBA), with total fluxes of 2,250 ± 306 kg year^{-1}, including 18% transported via suspended particles (Table S6). The regional flux ranking remained consistent—SCAG (536 ± 39 kg year^{-1}), AEG (449 ± 24 kg year^{-1}), and WCUG (426 ± 15 kg year^{-1})—but the total global flux was substantially lower, underscoring the importance of including PFBA in future assessments. Improved analytical techniques, such as high-resolution mass spectrometry,[38] are essential for accurately quantifying low-mass PFAAs and ensuring comparability across studies in the future.

Global patterns of release and depositional fluxes

Based on the field measurements, predicted logK_d, and modeled glacial runoffs, we estimated that glaciers globally release approximately 3,547 ± 375 kg year^{-1} of Σ_{13}PFAAs into downstream environments, with about 12% transported via suspended particles. While previous studies have only quantified dissolved-phase fluxes at the regional scale,[25,26] our study extends this assessment to the global scale and incorporates the often overlooked particle-bound phase.

To evaluate whether PFAA release is in balance with atmospheric inputs, we compared regional glacial output fluxes with deposition fluxes estimated by the GEOS-Chem global atmospheric chemistry model (Table 1)[27] and the estimates derived from ice core records in the same glacial regions (Table S9).[14,15,39–41] Deposition fluxes showed substantial regional variability, with AIS ≈ GIS ≈ SCAG > ACG ≈ WCUG > CEG ≈ NAG (Table 1). The high depositional fluxes in AIS and GIS were primarily due to their large glacial surface areas. In contrast, the comparable flux in SCAG can be linked to the high deposition concentration of PFAAs from nearby emission sources.[42,43]

Since GEOS-Chem model only include PFCAs, we focused on the comparison on Σ_{10}PFCAs (Table 1). Our results show that the global average glacial release fluxes of Σ_{10}PFCAs (~2,900 kg year^{-1}) were about 3–9 times higher than the modeled atmospheric deposition inputs (329–900 kg year^{-1}). Regionally, the

Please cite this article in press as: Zhou et al., Global flux of perfluoroalkyl acids from glaciers in a warming climate, One Earth (2025), https://doi.org/10.1016/j.oneear.2025.101453

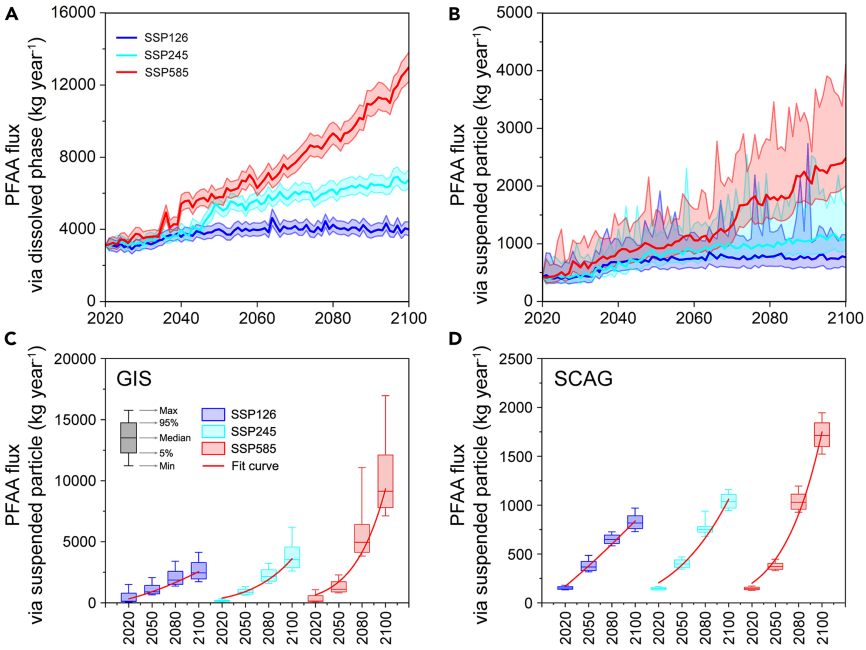

Figure 5. Future release potential of perfluoroalkyl acids from glaciers in eight glacial regions in 2020–2100 under three climate-change scenarios

Annual future release potential (kg year^{-1}) of perfluoroalkyl acids (PFAAs) from glaciers in eight glacial regions via (A) the dissolved phase and (B) suspended particles in 2020–2100 under three climate-change scenarios (SSP126, SSP245, and SSP585), and the release potential (kg year^{-1}) of PFAAs via suspended particles from glaciers in (C) the Greenland ice sheet (GIS) and (D) South and Central Asia (SCAG). The release potential refers to a predicted possibility of PFAA fluxes under future climate scenarios. The solid line in (A) and (B) presents the average value with a window of 1 year, and the shaded area indicates the range of minimum and maximum values. The line in the boxes of (C) and (D) is the median line, the edges of the boxes are the 5th and 95th percentile, and the whisker is the range within the minimum and maximum values. The difference in the time scales on the horizontal axis in part (C) and (D) compared with (A) and (B) is due to the assumption that the release of glacier meltwater sediment doubles every 30 years.[33]

glacial release flux exceeds the maximum depositional flux in all glacial regions except for the AIS. This was obvious in ACG and SCAG, where the export fluxes of Σ_{10}PFCAs were 6–8 times higher than the maximum import fluxes (Table 1), followed by CEG and WCUG, due to rapid glacier ablation.[31] These findings indicated that under climate warming most glaciers were experiencing a net loss of PFAAs.

By contrast, the maximum depositional fluxes for the AIS were about 2-fold higher than the current release fluxes of Σ_{10}PFCAs, suggesting that the AIS may still act as a temporary sink for PFAAs.[41] Therefore, accumulation of PFAAs in the AIS should be continuously monitored,[41,44] particularly concerning their adverse effects on sensitive Antarctic wildlife such as penguins.[45]

Intriguingly, based on results from the Devon, Meighen, Melville, and Agassiz ice caps in 2005,[46] the total depositional flux of just four PFCAs, namely PFOA, perfluorononanoic acid (PFNA), perfluorodecanoic acid (PFDA), and perfluoroundecanoic acid (PFUdA), to the Arctic (north of 65° N) was approximately 2,603 kg year^{-1}. This value is almost an order of magnitude higher than the estimated depositional fluxes for the Arctic regions (ACG + GIS + AEG = 128–390 kg year^{-1}) derived from the GEOS-Chem model for the period 2013–2015 (Table 1). The substantial decline in deposition flux during 2013–2015 may be attributed to the gradual phase-outs of PFAAs.[47] This discrepancy suggests that large amounts of PFAAs had already been deposited and stored in Arctic glaciers during earlier decades.

Known as "forever chemicals," PFAAs deposited on snow/ice are likely to undergo minimal degradation,[11] resulting in their long-term storage within the glaciers for decades to centuries.[48] With continuous global warming, the previously stored PFAAs in glaciers (aged ice) would be largely released at an increasing rate.[49,50]

Glacial fluxes compared to global PFAA emissions

While glaciers have been identified as secondary sources of PFAAs, their contribution remains limited in the context of global emissions. PFAAs have been widely used in industrial and household applications since the mid-20th century.[6] Under a high-emission scenario, global annual emissions of Σ_{10}PFCAs around 2020 were estimated at approximately 400 tons.[51] In comparison, the total glacial release fluxes of Σ_{10}PFCAs are approximately 2.9 tons per year (Table 1), representing only about 0.7% of annual global emissions and indicating a limited contribution. Similarly, the input of PFAAs to the Arctic via glacial meltwater is also minor compared to the hundreds of tons transported by sea-spray aerosols.[37]

Nevertheless, the local impact of glacial release on PFAA distribution and wildlife in glacial regions remains significant. As observed in Figure 4A, PFAA concentrations in Arctic fjords are higher than in other locations. The deep and narrow structure of fjords can restrict water circulation, leading to slower mixing and flushing, which causes PFAAs to accumulate in the fjord waters for extended periods. Similarly, PFAA levels in high-latitude Arctic fjord sediments are higher than in lower latitudes.[20] The unique geomorphology of Arctic fjords, characterized by deep valleys and significant sediment deposits, allows for more effective trapping and accumulation of PFAAs. Importantly, many of these fjords also sustain vital fisheries.[52] Therefore, the Arctic fjords should be of high concern in the Arctic regions.

In the SCAG region, high-level PFAA areas are predominantly located south of 33° N latitude (Figure 4B). The Khumbu and Rongbuk glaciers have the largest PFAA risk buffer zones, followed by the Yulong Baishui No. 1 glacier (Figure 4B). These glaciers are located in the monsoon-affected southern Tibetan Plateau (south of 33° N), where glacier melt rates are higher compared to the north.[53] Proglacial river sediments have been proven to be substantial sinks for PFAAs released by glacial

meltwater,[18] acting as important sources for the benthic food web. The export of PFAAs by meltwater and suspended particles has led to PFAAs being enriched in cold-water fish species in the Tibetan rivers (south of SCAG).[54] Consequently, particular attention should be given to headwater regions at glacier termini and adjacent catchments, as they are likely hotspots for PFAA contamination.

Adverse effects of increased PFAA outflows

With ongoing glacial retreat, the particle-bound fraction of PFAAs, especially bioaccumulative long-chain compounds, is expected to increase substantially. Our estimates suggest that fluvial suspended particles currently deliver 238 ± 63 kg year^{-1} of long-chain PFAAs globally (Table S6), a figure likely to grow as glacier erosion and sediment fluxes intensify under warming conditions.[33,55,56] For example, projections for Greenland indicate that sediment transport could double every 30 years,[33] leading to a 20- to 60-fold increase in particle-bound Σ_{13}PFAAs releases by 2100 under different SSP scenarios (Figure 5C). This sediment enrichment may eventually surpass meltwater as the dominant pathway of PFAA outflows, posing increasing risks to proglacial ecosystems.

Sediments serve as an important pathway for the entry of PFAAs into the food web (i.e., sediment-phytoplankton-zooplankton-Arctic char-seals-polar bears).[22–24] Bioaccumulation factors for long-chain PFAAs are approximately 30- to 50-fold from sediment to Arctic char,[23] 10- to 30-fold from char to ringed seals,[57] and up to 10-fold from seal to polar bear.[58] Under the worst-case warming scenario (SSP585), PFAA concentrations in polar bear liver tissues could rise from current levels of several μg g^{-1} to potentially mg g^{-1} concentrations (Figure S4). Although no official safe thresholds have been established for PFAAs in polar bears, such extremely high concentrations would exacerbate their health risks.

Polar bears are already listed on the International Union for Conservation of Nature Red List.[59] Rising PFAA concentrations under future warming scenarios could accelerate the decline of this keystone species, disrupt Arctic ecosystems, and contribute to broader biodiversity loss. Although the Arctic Monitoring and Assessment Program has already warned of increasing PFAA-related toxicity in polar organisms,[60] our work provides a quantitative amplification of this trend, specifically in the increased concentrations found in the livers of polar bears (Figure S4). This is critical for understanding and mitigating the environmental impact of PFAAs released from glacial sources.

Compared to the Arctic, the Tibetan Plateau (southern SCAG) presents a lower risk profile. The aquatic food chain in the plateau is generally shorter than that of the Arctic marine ecosystem, which limits the biomagnification of PFAAs.[54] However, glaciers on the Tibetan Plateau serve as the headwaters of major Asian rivers that support the livelihoods of over 2 billion people downstream.[53] Under future warming scenarios, accelerated glacial melt and enhanced sediment transport may increase the release of particle-bound PFAAs into these headwater systems. This could pose adverse impacts on ice-dwelling headwater species at the base of the food web, such as algae, copepods, and amphipods.[61] Such upstream ecological disturbances may cascade downstream, threatening water quality and aquatic biodiversity in major Asian rivers.

Controlling future PFAA releases from glaciers

To mitigate adverse impacts of future PFAA releases from glaciers, coordinated and immediate global actions are essential. Reducing greenhouse gas emissions remains the most critical step, as slowing the rate of climate warming directly reduces glacial melt rates and the remobilization of legacy PFAAs stored in ice. Lower emissions will not only stabilize climatic systems but also protect ecosystems from accelerated degradation due to rising temperatures.

In parallel, stronger global regulations on PFAS production and use are urgently needed. Current policies have largely targeted long-chain PFAAs and their precursors, but short-chain and emerging PFASs—many of which are poorly regulated or still unknown—are now dominant in the environment. Expanding regulatory frameworks to include these compounds is essential for protecting sensitive ecosystems, particularly polar and alpine regions where bioaccumulation risks remain high.

Policy oversight must also account for unintended consequences. For instance, the global transition from chlorofluorocarbons to short-lived substitutes under the Montreal Protocol has inadvertently accelerated atmospheric deposition of ultra-short-chain PFAAs, such as trifluoroacetic acid.[48,62] These substitutes, while beneficial for ozone protection, now contribute both to climate forcing and chemical contamination.[63] This underscores the need for integrated environmental governance, where solutions to one crisis do not amplify another.

As shown in Figures 5A and 5B, the world faces a narrow window of approximately 15 years to effectively curb glacier-derived PFAA release. A combined strategy of emissions reduction, PFAS regulation, and careful chemical substitution is essential. Without coordinated intervention, PFAA discharges from glaciers are projected to rise sharply, with long-term consequences for freshwater security, fisheries, biodiversity, and global pollutant burdens.

Finally, establishing long-term environmental and wildlife monitoring programs is crucial. These systems serve as early-warning networks, enabling the detection of rising PFAA levels and other ecological stress signals in fragile regions. Proactive monitoring not only informs risk assessment and response but also supports evidence-based policy decisions aimed at preventing irreversible ecological damage to the most fragile cryosphere on our planet.

METHODS

Study area and field sampling

Seven glaciers on the Tibetan Plateau (affiliated to part of SCAG) were investigated in the field, including the Rongbuk (RB), Qiangyong (QY), and Rijie Cojia (RC) glaciers in the Himalayan Mountains, the Korchung Gangri (KG) and Zhadang (ZD) glaciers in the Gangdise–Nyainqêntanglha Mountains, and the Galongla (GL) and Parlung No. 4 (PL) glaciers in the Hengduan Mountains (Figure 1). Among them, RB, ZD, KG, QY, and RC are continental valley glaciers, whereas the GL and PL are typical temperate glaciers. Details of these glacial regions, among which there are significant geographical, hydrological, and meteorological differences, are summarized in Table S10.

Meltwater sampling was conducted from July to August 2020, corresponding to the peak melting season. At each glacier,

Please cite this article in press as: Zhou et al., Global flux of perfluoroalkyl acids from glaciers in a warming climate, One Earth (2025), https://doi.org/10.1016/j.oneear.2025.101453

surface runoff samples (0–30 cm) were collected at three sites from the upstream to the downstream (Figure 1A). Approximately 20 L of water was collected at each site using pre-cleaned polypropylene bottles. Prior to use, all sampling bottles were rinsed three times with methanol and Milli-Q water. To minimize contamination, sampling materials containing fluoropolymer coatings or PFAS-related components were strictly avoided. *In situ* measurements of basic water quality parameters, including water temperature (T_w), pH, conductivity (σ), and dissolved oxygen (DO), were conducted during the sampling at the same site.

Analysis of PFAAs

Glacial runoff samples from seven glacial catchments on the Tibetan Plateau were analyzed for 13 target PFAAs. Upon analysis, all water samples were filtered through Whatman 0.7-μm glass fiber filters (GFFs) to separate suspended particles. The filtrates (2 L each) were subjected to solid-phase extraction (SPE) using Waters Oasis WAX cartridges (150 mg, 6 cm^3, 30 μm), while the retained GFFs were extracted by ultrasonic agitation using methanol to measure particle-bound PFAAs. Detailed extraction procedures are described in Notes S2 and S3.

Quantification of 13 PFAAs and internal standards (Table S11) were performed using high-performance liquid chromatography coupled with tandem mass spectrometry (HPLC-MS/MS; Thermo Fisher UltiMate 3000 and TSQ Quantiva triple quadrupole system), as described in Note S4. POC on the GFFs (the suspended particle samples) was measured using a Shimadzu 5000-A total organic carbon analyzer to support subsequent partitioning analysis.

All analytical procedures were conducted under strict quality assurance and quality control measures (Note S5). Field and procedural blanks prepared with Milli-Q water yielded concentrations below the method quantification limits (Table S12), confirming that sample contamination was negligible. Matrix spiked recoveries, obtained by spiking with 2,000 pg of internal standards, ranged from 52% to 81% for water samples and 42%–70% for suspended particle samples, with detailed values listed in Table S13.

Identification of glacial regions and data compilation

The identification of glacial regions was undertaken using version 6.0 of the Randolph Glacier Inventory (http://www.glims.org/RGI/). Eight major glacial regions were included in this study (Figure 2): (1), WCUG, (2) ACG, (3) GIS, (4) AEG, (5) NAG, (6) CEG, (7) SCAG, and (8) AIS.

To construct a global dataset of PFAA concentrations, we compiled published data for 13 PFAAs from 680 samples across 49 glaciers in these eight glacial regions (Figure 2). The dataset includes samples from glacial runoff, snow/ice, and seawater neighboring the glaciers. In addition, we combined our field measurements (n = 59) from seven glaciers on the Tibetan Plateau with the above published data to produce a global dataset (n = 739, Table S2). This integrated dataset offers the basis for the global-scale assessment of PFAA fluxes from glaciers.

Drivers of particle-water partition coefficient

The K_d is defined as the ratio of a chemical's concentration in the particle-bound phase (C_p) to that in the dissolved phase (C_w) (i.e., $K_d = C_p/C_w$). The logK_d data obtained from measurements of 13 PFAA concentrations in runoff water and suspended particles from the Tibetan glaciers is presented in Table S4. While K_d values are variable, they often respond to environmental factors and chemical properties of PFAAs.

To explore the key drivers of PFAA partitioning, we analyzed the relationships between logK_d and several environmental parameters, including pH, T_w, POC, σ, and DO, as well as molecular descriptors such as perfluorinated chain length and functional group type (i.e., carboxylates for PFCAs and sulfonates for PFSAs). Statistically significant correlations were observed between logK_d and both POC and T_w ($p < 0.05$), while no significant correlations were found for pH, DO, or σ (Table S14). These findings are consistent with previous studies highlighting the importance of organic carbon and water temperature in governing PFAS partitioning.[64]

In addition, we examined the influence of molecular hydrophobicity using theoretical ionic octanol-water partition coefficients (log$K_{ow\text{-}ionic}$), as reported by Hidalgo and Mora-Diez.[65] Given that glacial meltwaters are commonly alkaline[66] and PFAAs possess low pK_a values (typically <1.0), these compounds are expected to be fully dissociated to their anionic forms.[67] The log$K_{ow\text{-}ionic}$ values, which vary by carbon-chain length but are fixed for each compound, were significantly correlated with logK_d ($p < 0.01$, Figure S5), which suggests that log$K_{ow\text{-}ionic}$ can be a useful model predictor of logK_d, especially if combined with the aforementioned POC and T_w.

To support model development, we compiled a comprehensive dataset (n = 771), containing logK_d, T_w, POC, log$K_{ow\text{-}ionic}$, and PFAA type. These data were sourced from both glacial regions (n = 191) and non-glacial environments (e.g., inland watersheds and coastal areas; n = 580). All values were either directly measured or extracted from the previous literature, as listed in Table S4. Notably, T_w values were all below 19°C to represent relatively low-temperature environments, with data-screening criteria detailed in Note S1.

Prediction of K_d with ML models

Traditional curve-fitting methods showed limited performance in predicting logK_d. To overcome this limitation, we developed ML models to estimate logK_d, including SVMs, DTs, RFs, and XGBoost.

All ML models were implemented in Python v.3.9.7 using the *scikit-learn* module. Model performance was evaluated using multiple metrics: the coefficient of determination for the training set (R^2), the predictive Q^2 for the test set, and the mean absolute error (MAE) and mean squared error (MSE) for both sets. To ensure robustness and reproducibility, the dataset was randomly divided into training and test sets using sklearn.model_selection.train_test_split, with varying split ratios ranging from 5:95 to 50:50 and ten replicates for each ratio.

Among all models, XGBoost-ML (denoted as Xgb_A) exhibited the best overall performance, achieving the highest R^2 (0.95 ± 0.01) and Q^2 (0.85 ± 0.04), along with the lowest MAE and MSE for both the training set (0.138 ± 0.016 and 0.034 ± 0.008, respectively) and test set (0.241 ± 0.032 and 0.105 ± 0.030, respectively). Additionally, statistical analyses using Student's t tests showed no significant variation in predictive accuracy when increasing the proportion of the test set from 5% to 45% of the total dataset

(raw significance level $\alpha = 0.05$, Bonferroni-corrected significance level $\alpha = 0.0011$, number of tests = 45).

Based on these results, the XGBoost-ML (Xgb_A) was selected as the best-performing model for predicting logK_d. Further details regarding ML model development and comparative performance are provided in Note S1.

Glacial mass balance model

Glacial runoff was calculated using a water balance approach adapted from Bliss et al.[31] Within each glacial region, there are several subregions characterized by different meteorological and geological characteristics. In addition, there are several different landforms in each subregion, which might influence the melting rate of snow or ice, i.e., the degree-day factor for snow/ice. Therefore, the estimation for the monthly glacier runoff needs to account for variations among different subregions and landforms. The monthly average glacier runoff of each glacial region (Q) was calculated using

$$Q = \sum_{i=1}^{n} S_i \times (a_i + P_{liq,i} - R_i) \quad \text{(Equation 1)}$$

where S_i (km^2) is the effective area of the glacial region, which is computed by the annual average area of subregion i, included by the glacial region. a_i is the snow/ice melt of each month, $P_{liq,i}$ (mm) is the net accumulated liquid precipitation of each month, and R_i (%) is the potential of refreezing during melting of each month.

It was assumed that melting had a linear correlation with the monthly air temperature, a_i, if >0°C, and thus a_i was calculated using

$$a_i = f_{snow/ice} \times \int \max(T_i, 0) dt \quad \text{(Equation 2)}$$

where $f_{snow/ice}$, the degree-day factor for snow/ice ([mm water equivalent] day^{-1} °C^{-1}), is a constant that depends on the sample types, and T_i, the monthly air temperature (°C) above the glacier surface, is a random variable, which was computed using

$$T_i = T_{annual\ average} + (T_{summer} - T_{annual\ average}) \times \sin\left((i-4) \times \frac{2\pi}{12}\right) + \delta T_i \quad \text{(Equation 3)}$$

where the $T_{annual\ average}$ and T_{summer} were provided from previous studies.[31] δT_i is a random variable following normal distributions, with a mean value of 0°C. When i referred to winter (December to February) or summer (June to August) time, δT_i was the standard deviation of summer temperatures. Vice versa, when i referred to Spring (March to May) or Autumn (September to November) time, δT_i was the standard deviation of annual average temperatures.

Fluxes contributed by liquid precipitations, $P_{liq,i}$, were calculated using

$$P_{liq,i} = P_i \times \theta_{(T_i,0)} \quad \text{(Equation 4)}$$

where P_i is a random parameter following a normal distribution, with its mean value and standard deviation cited from previous publications,[66] and $\theta_{(T_i,0)}$ is a Heaviside function, which equals 1 when T_i is greater than 0 and equals 0 when T_i is less than or equal to 0.

R_i was estimated according to the linear relationship between R_i and air temperature (T_i) at different elevations, assuming that the snow meltwater frozen on the surface of the glacier (R_i) does not flow away. The estimation was conducted using

$$R_i = -0.69 \times T_i + 0.0096 \quad \text{(Equation 5)}$$

For each of eight glacial regions, 2,500 Monte Carlo simulations were conducted (Note S6). For each simulation, glacier runoff fluxes in 12 months were computed using the method stated above and then summed over to obtain the annual glacier runoff fluxes. One glacial region may be composed of several glaciers, while each of them might have a different composition of landforms: three types of landforms, namely the sample types, were considered, having different degree-day factors: $f_{snow/ice} = 1$ for "glacier runoff," $f_{snow/ice} = 2$ for "snow/ice," and $f_{snow/ice} = 4$ for "seawater neighboring the glaciers." Each sample type was chosen randomly for the simulation of the whole year, without bias.

Released flux estimation of PFAAs, dissolved part

The annual fluxes of 13 PFAAs in the dissolved phase were estimated for eight glacial regions using Monte Carlo simulations (Note S6). For each region and each PFAA, 2,500 simulations were conducted. Because a glacial region can consist of multiple subregions of varying sizes, the number of simulations allocated to each subregion is determined based on the respective area sizes within the larger region. For each simulation, the PFAA concentrations discharged in a subregion (C_w) were those of a sample randomly chosen from one of three sample types (ice/snow, glacier runoff, and seawater) (Table S2), with equal probability.

The glacial meltwater fluxes of the subregion from each sample type in each month were determined in the aforementioned glacial mass balance model, and the PFAA fluxes in dissolved phase of that month were the concentration of PFAAs times the corresponding runoff volume. Annual fluxes for each region were derived by summing monthly fluxes across all subregions.

Released flux estimation of PFAAs, suspended particle part

The annual fluxes of 13 PFAAs partitioned on suspended particles of the eight glacial regions were also estimated using Monte Carlo simulations (Note S6). Based on the predictions for logK_d by the XGBoost-ML and the reported mean PFAA concentrations in water of each glacial region, we obtained the concentration of PFAAs on suspended particles (C_p) (Table S5). The annual particulate PFAA fluxes from different glacial regions were then estimated by multiplying the mean C_p by the regional average glacial runoff and the mean suspended particle concentration (Table 1). The final flux estimates for all regions are presented in Table S6.

Future release potential of PFAAs

The projected future release fluxes of 13 PFAAs in both dissolved and particle-bound phases were estimated with the support of SSPs, which provided estimates of air temperature and precipitation from 2020 to 2100 (Figures S6 and S7). The modeling assumed there would be sufficiently large amounts of historical storage of PFAAs in glaciers.

Three SSP scenarios, namely SSP126, SSP245, and SSP585,[68,69] were utilized to represent low, intermediate, and high global warming scenarios, respectively. For each scenario, the annual and summer average air temperatures in each subregion were calibrated using the 2020 values as a baseline. This ensured that the projected temperature increases under different SSPs, relative to 2020, were maintained. Similarly, monthly precipitation values for each region were calculated based on the recorded data from 2020, such that changes in annual precipitation projected by the SSPs were consistently applied while preserving the seasonal distribution. Detailed calibration procedures are provided in Note S6.

The potential release fluxes of 13 PFAAs, both in the dissolved phase and on suspended particles, were estimated annually from 2020 to 2100 under the three climate warming scenarios (Figures 5A and 5B). For each year, 2,500 Monte Carlo simulations were conducted to account for variability and uncertainty. The modeling approach for 2021–2100 followed the same framework used for the baseline year 2020, ensuring methodological consistency across the entire simulation period.

Deposition and budget estimates of Σ_{10}PFCAs

Atmospheric deposition is the primary input pathway of PFAAs to glacier surfaces. As the GEOS-Chem model does not simulate PFSAs,[27] our analysis focuses on ten PFCAs with carbon-chain lengths from C4 to C13 (Σ_{10}PFCAs). Using the atmospheric depositional fluxes of Σ_{10}PFCAs generated by the GEOS-Chem model[27] along with glacier surface area data (Table 1), we estimated the deposition fluxes (input) of Σ_{10}PFCAs to global glaciers. By comparing this input with the predicted release fluxes (output) of Σ_{10}PFCAs, we evaluated the input-output budget of Σ_{10}PFCAs across the eight different glacial regions (Table 1).

The GEOS-Chem model (version 12.2) is a widely used, community-developed atmospheric chemistry model that incorporates reanalysis meteorological data to simulate the transport and deposition of pollutants. Σ_{10}PFCAs were included in the GEOS-Chem model with a detailed set of chemical reactions, emission inventories, prescribed meteorology, and wet and dry deposition schemes.[27] The model was then run at a horizontal resolution of $4^\circ \times 5^\circ$, with 46 vertical levels, using assimilated GEOS-FP meteorology data. This produced the modeled spatial distribution of the annual deposition of Σ_{10}PFCAs in 2013–2015 resulting from the inventory of degradation of precursor molecules and direct global emissions. Due to the observed long-term stability of atmospheric PFAA concentrations, e.g., perfluorooctane sulfonic acid, in polar regions over recent decades (Note S7),[12,70] we assumed the annual deposition fluxes of Σ_{10}PFCAs from 2013 to 2020 are the same.

The GEOS-Chem estimation contains a few uncertainties. These include incomplete emission inventories of short-chain PFAA replacements[71,72] and precursors,[17,51] unquantified contribution of sources such as sea-spray aerosols,[73,74] and limited understanding of atmospheric transformation mechanism.[75] Despite these limitations, the GEOS-Chem model offers a valuable basis for estimating large-scale deposition patterns of PFAAs to compare their input-output budget in remote glacial environments.

RESOURCE AVAILABILITY

Lead contact

Requests for further information and resources should be directed to and will be fulfilled by the lead contact, Xiaoping Wang (wangxp@itpcas.ac.cn).

Materials availability

This study did not generate new unique materials.

Data and code availability

The code and data required for Monte Carlo simulation of PFAA glacial runoff volumes, logK_d estimation for each situation based on trained XGBoost model, and the estimated release fluxes of PFAAs via dissolve phase and suspended particles are available in https://github.com/EssexHUBOYUAN/Glacial_runoff_PFAS_sims.

ACKNOWLEDGMENTS

This study was supported by the National Natural Science Foundation of China (41925032, 22022611, and 42107438), the Second Tibetan Plateau Scientific Expedition and Research Program (STEP) (2019QZKK0605), the Chinese Academy of Sciences Project for Young Scientists in Basic Research (YSBR-086), and the China Postdoctoral Science Foundation (2020M680696 and 2023T160659).

AUTHOR CONTRIBUTIONS

Conceptualization, X.W. and J.F.; methodology, Y.Z., B.H., and M.C.; investigation, L.W., M.C., and S.R.; formal analysis, B.H. and M.C.; visualization, Y.Z., B.H., and M.C.; writing – original draft, Y.Z. and B.H.; writing – review and editing, X.W., J.F., I.T.C., X.B., C.W., H.D., Z.W., T.A., D.L., K.C.J., and D.C.G.M.; funding acquisition, X.W., J.F., and Y.Z.

DECLARATION OF INTERESTS

The authors declare no competing interests.

SUPPLEMENTAL INFORMATION

Supplemental information can be found online at https://doi.org/10.1016/j.oneear.2025.101453.

Received: July 26, 2024
Revised: April 23, 2025
Accepted: August 21, 2025

REFERENCES

1. Persson, L., Carney Almroth, B.M., Collins, C.D., Cornell, S., de Wit, C.A., Diamond, M.L., Fantke, P., Hassellöv, M., MacLeod, M., Ryberg, M.W., et al. (2022). Outside the safe operating space of the planetary boundary for novel entities. Environ. Sci. Technol. *56*, 1510–1521. https://doi.org/10.1021/acs.est.1c04158.
2. Carney Almroth, B., Cornell, S.E., Diamond, M.L., de Wit, C.A., Fantke, P., and Wang, Z. (2022). Understanding and addressing the planetary crisis of chemicals and plastics. One Earth *5*, 1070–1074. https://doi.org/10.1016/j.oneear.2022.09.012.
3. Richardson, K., Steffen, W., Lucht, W., Bendtsen, J., Cornell, S.E., Donges, J.F., Drüke, M., Fetzer, I., Bala, G., von Bloh, W., et al. (2023). Earth beyond six of nine planetary boundaries. Sci. Adv. *9*, eadh2458. https://doi.org/10.1126/sciadv.adh2458.
4. Evich, M.G., Davis, M.J.B., McCord, J.P., Acrey, B., Awkerman, J.A., Knappe, D.R.U., Lindstrom, A.B., Speth, T.F., Tebes-Stevens, C., Strynar, M.J., et al. (2022). Per- and polyfluoroalkyl substances in the environment. Science *375*, eabg9065. https://doi.org/10.1126/science.abg9065.

5. Garrett, K.K., Brown, P., Varshavsky, J., and Cordner, A. (2022). Improving governance of "forever chemicals" in the US and beyond. One Earth *5*, 1075–1079. https://doi.org/10.1016/j.oneear.2022.10.003.

6. Glüge, J., Scheringer, M., Cousins, I.T., DeWitt, J.C., Goldenman, G., Herzke, D., Lohmann, R., Ng, C.A., Trier, X., and Wang, Z. (2020). An overview of the uses of per- and polyfluoroalkyl substances (PFAS). Environ. Sci. Process. Impacts *22*, 2345–2373. https://doi.org/10.1039/D0EM00291G.

7. Wang, Z., DeWitt, J.C., Higgins, C.P., and Cousins, I.T. (2017). A never-ending story of per- and polyfluoroalkyl substances (PFASs)? Environ. Sci. Technol. *51*, 2508–2518. https://doi.org/10.1021/acs.est.6b04806.

8. Sunderland, E.M., Hu, X.C., Dassuncao, C., Tokranov, A.K., Wagner, C.C., and Allen, J.G. (2019). A review of the pathways of human exposure to poly-and perfluoroalkyl substances (PFASs) and present understanding of health effects. J. Expo. Sci. Environ. Epidemiol. *29*, 131–147. https://doi.org/10.1038/s41370-018-0094-1.

9. Chen, M., Wang, C., Gao, K., Wang, X., Fu, J., Gong, P., and Wang, Y. (2021). Perfluoroalkyl substances in precipitation from the Tibetan Plateau during monsoon season: concentrations, source regions and mass fluxes. Chemosphere *282*, 131105. https://doi.org/10.1016/j.chemosphere.2021.131105.

10. Cousins, I.T., Johansson, J.H., Salter, M.E., Sha, B., and Scheringer, M. (2022). Outside the safe operating space of a new planetary boundary for per-and polyfluoroalkyl substances (PFAS). Environ. Sci. Technol. *56*, 11172–11179. https://doi.org/10.1021/acs.est.2c02765.

11. Zhou, Y., Wang, X., Wang, C., Ji, Z., Niu, X., and Dong, H. (2024). Fate of 'forever chemicals' in the global cryosphere. Earth Sci. Rev. *259*, 104973. https://doi.org/10.1016/j.earscirev.2024.104973.

12. Muir, D., Bossi, R., Carlsson, P., Evans, M., De Silva, A., Halsall, C., Rauert, C., Herzke, D., Hung, H., Letcher, R., et al. (2019). Levels and trends of poly- and perfluoroalkyl substances in the Arctic environment – An update. Emerging Contam. *5*, 240–271. https://doi.org/10.1016/j.emcon.2019.06.002.

13. Xie, Z., Wang, Z., Magand, O., Thollot, A., Ebinghaus, R., Mi, W., and Dommergue, A. (2020). Occurrence of legacy and emerging organic contaminants in snow at Dome C in the Antarctic. Sci. Total Environ. *741*, 140200. https://doi.org/10.1016/j.scitotenv.2020.140200.

14. Wang, X., Halsall, C., Codling, G., Xie, Z., Xu, B., Zhao, Z., Xue, Y., Ebinghaus, R., and Jones, K.C. (2014). Accumulation of perfluoroalkyl compounds in tibetan mountain snow: temporal patterns from 1980 to 2010. Environ. Sci. Technol. *48*, 173–181. https://doi.org/10.1021/es4044775.

15. Kirchgeorg, T., Dreyer, A., Gabrieli, J., Kehrwald, N., Sigl, M., Schwikowski, M., Boutron, C., Gambaro, A., Barbante, C., and Ebinghaus, R. (2013). Temporal variations of perfluoroalkyl substances and polybrominated diphenyl ethers in alpine snow. Environ. Pollut. *178*, 367–374. https://doi.org/10.1016/j.envpol.2013.03.043.

16. Ng, C., Cousins, I.T., DeWitt, J.C., Glüge, J., Goldenman, G., Herzke, D., Lohmann, R., Miller, M., Patton, S., Scheringer, M., et al. (2021). Addressing urgent questions for PFAS in the 21st century. Environ. Sci. Technol. *55*, 12755–12765. https://doi.org/10.1021/acs.est.1c03386.

17. Wang, Z., Boucher, J.M., Scheringer, M., Cousins, I.T., and Hungerbühler, K. (2017). Toward a comprehensive global emission inventory of C4–C10 perfluoroalkanesulfonic acids (PFSAs) and related precursors: focus on the life cycle of C8-based products and ongoing industrial transition. Environ. Sci. Technol. *51*, 4482–4493. https://doi.org/10.1021/acs.est.6b06191.

18. Zhou, Y., Wang, X., Chen, M., Fu, J., Zhu, T., Wang, C., Gong, P., Wang, L., and Ren, J. (2024). Proglacial river sediments are a substantial sink of perfluoroalkyl substances released by glacial meltwater. Commun. Earth Environ. *5*, 68. https://doi.org/10.1038/s43247-024-01223-y.

19. MacInnis, J.J., Lehnherr, I., Muir, D.C.G., St. Pierre, K.A., St. Louis, V.L., Spencer, C., and De Silva, A.O. (2019). Fate and transport of perfluoroalkyl substances from snowpacks into a lake in the High Arctic of Canada. Environ. Sci. Technol. *53*, 10753–10762. https://doi.org/10.1021/acs.est.9b03372.

20. MacInnis, J.J., Lehnherr, I., Muir, D.C.G., Quinlan, R., and De Silva, A.O. (2019). Characterization of perfluoroalkyl substances in sediment cores from High and Low Arctic lakes in Canada. Sci. Total Environ. *666*, 414–422. https://doi.org/10.1016/j.scitotenv.2019.02.210.

21. Rigét, F., Bignert, A., Braune, B., Dam, M., Dietz, R., Evans, M., Green, N., Gunnlaugsdóttir, H., Hoydal, K.S., Kucklick, J., et al. (2019). Temporal trends of persistent organic pollutants in Arctic marine and freshwater biota. Sci. Total Environ. *649*, 99–110. https://doi.org/10.1016/j.scitotenv.2018.08.268.

22. Lescord, G.L., Kidd, K.A., De Silva, A.O., Williamson, M., Spencer, C., Wang, X., and Muir, D.C.G. (2015). Perfluorinated and polyfluorinated compounds in lake food webs from the Canadian High Arctic. Environ. Sci. Technol. *49*, 2694–2702. https://doi.org/10.1021/es5048649.

23. Langberg, H.A., Breedveld, G.D., Slinde, G.A., Grønning, H.M., Høisæter, Å., Jartun, M., Rundberget, T., Jenssen, B.M., and Hale, S.E. (2020). Fluorinated precursor compounds in sediments as a source of perfluorinated alkyl acids (PFAA) to biota. Environ. Sci. Technol. *54*, 13077–13089. https://doi.org/10.1021/acs.est.0c04587.

24. Sonne, C., Desforges, J.-P., Gustavson, K., Bossi, R., Bonefeld-Jørgensen, E.C., Long, M., Rigét, F.F., and Dietz, R. (2023). Assessment of exposure to perfluorinated industrial substances and risk of immune suppression in Greenland and its global context: a mixed-methods study. Lancet Planet. Health *7*, e570–e579. https://doi.org/10.1016/S2542-5196(23)00106-7.

25. MacInnis, J.J. (2020). Elucidation of the Transport and Fate of Per-And Polyfluoroalkyl Substances in the High Arctic of Canada (Memorial University of Newfoundland).

26. Chen, M., Wang, C., Wang, X., Fu, J., Gong, P., Yan, J., Yu, Z., Yan, F., and Nawab, J. (2019). Release of perfluoroalkyl substances from melting glacier of the Tibetan Plateau: Insights into the impact of global warming on the cycling of emerging pollutants. JGR. Atmospheres *124*, 7442–7456. https://doi.org/10.1029/2019JD030566.

27. Thackray, C.P., Selin, N.E., and Young, C.J. (2020). A global atmospheric chemistry model for the fate and transport of PFCAs and their precursors. Environ. Sci. Proc. Imp. *22*, 285–293. https://doi.org/10.1039/c9em00326f.

28. Pfeffer, W.T., Arendt, A.A., Bliss, A., Bolch, T., Cogley, J.G., Gardner, A.S., Hagen, J.-O., Hock, R., Kaser, G., Kienholz, C., et al. (2014). The Randolph Glacier Inventory: a globally complete inventory of glaciers. J. Glaciol. *60*, 537–552. https://doi.org/10.3189/2014JoG13J176.

29. Liston, G.E., and Winther, J.-G. (2005). Antarctic surface and subsurface snow and ice melt fluxes. J. Clim. *18*, 1469–1481. https://doi.org/10.1175/JCLI3344.1.

30. Tedesco, M., Fettweis, X., Mote, T., Wahr, J., Alexander, P., Box, J.E., and Wouters, B. (2013). Evidence and analysis of 2012 Greenland records from spaceborne observations, a regional climate model and reanalysis data. Cryosphere *7*, 615–630. https://doi.org/10.5194/tc-7-615-2013.

31. Bliss, A., Hock, R., and Radić, V. (2014). Global response of glacier runoff to twenty-first century climate change. J. Geophys. Res. Earth Surf. *119*, 717–730. https://doi.org/10.1002/2013jf002931.

32. Martin, J.W., Smithwick, M.M., Braune, B.M., Hoekstra, P.F., Muir, D.C.G., and Mabury, S.A. (2004). Identification of long-chain perfluorinated acids in biota from the Canadian Arctic. Environ. Sci. Technol. *38*, 373–380. https://doi.org/10.1021/es034727+.

33. Zhang, T., Li, D., East, A.E., Walling, D.E., Lane, S., Overeem, I., Beylich, A.A., Koppes, M., and Lu, X. (2022). Warming-driven erosion and sediment transport in cold regions. Nat. Rev. Earth Environ. *3*, 832–851. https://doi.org/10.1038/s43017-022-00362-0.

34. Smith, T., and Bookhagen, B. (2018). Changes in seasonal snow water equivalent distribution in High Mountain Asia (1987 to 2009). Sci. Adv. *4*, e1701550. https://doi.org/10.1126/sciadv.1701550.

35. Hugonnet, R., McNabb, R., Berthier, E., Menounos, B., Nuth, C., Girod, L., Farinotti, D., Huss, M., Dussaillant, I., Brun, F., and Kääb, A. (2021). Accelerated global glacier mass loss in the early twenty-first century. Nature *592*, 726–731. https://doi.org/10.1038/s41586-021-03436-z.

36. Yeung, L.W.Y., Dassuncao, C., Mabury, S., Sunderland, E.M., Zhang, X., and Lohmann, R. (2017). Vertical profiles, sources, and transport of PFASs in the Arctic Ocean. Environ. Sci. Technol. *51*, 6735–6744. https://doi.org/10.1021/acs.est.7b00788.

37. Joerss, H., Xie, Z., Wagner, C.C., von Appen, W.J., Sunderland, E.M., and Ebinghaus, R. (2020). Transport of legacy perfluoroalkyl substances and the replacement compound HFPO-DA through the Atlantic Gateway to the Arctic Ocean-Is the Arctic a sink or a source? Environ. Sci. Technol. *54*, 9958–9967. https://doi.org/10.1021/acs.est.0c00228.

38. Abraham, K., El-Khatib, A.H., Schwerdtle, T., and Monien, B.H. (2021). Perfluorobutanoic acid (PFBA): No high-level accumulation in human lung and kidney tissue. Int. J. Hyg Environ. Health *237*, 113830. https://doi.org/10.1016/j.ijheh.2021.113830.

39. Pickard, H.M., Criscitiello, A.S., Spencer, C., Sharp, M.J., Muir, D.C.G., De Silva, A.O., and Young, C.J. (2018). Continuous non-marine inputs of per- and polyfluoroalkyl substances to the High Arctic: a multi-decadal temporal record. Atmos. Chem. Phys. *18*, 5045–5058. https://doi.org/10.5194/acp-18-5045-2018.

40. Kirchgeorg, T., Dreyer, A., Gabrielli, P., Gabrieli, J., Thompson, L.G., Barbante, C., and Ebinghaus, R. (2016). Seasonal accumulation of persistent organic pollutants on a high altitude glacier in the Eastern Alps. Environ. Pollut. *218*, 804–812. https://doi.org/10.1016/j.envpol.2016.08.004.

41. Garnett, J., Halsall, C., Winton, H., Joerss, H., Mulvaney, R., Ebinghaus, R., Frey, M., Jones, A., Leeson, A., and Wynn, P. (2022). Increasing accumulation of perfluorocarboxylate contaminants revealed in an Antarctic Firn Core (1958–2017). Environ. Sci. Technol. *56*, 11246–11255. https://doi.org/10.1021/acs.est.2c02592.

42. Wang, X., Chen, M., Gong, P., and Wang, C. (2019). Perfluorinated alkyl substances in snow as an atmospheric tracer for tracking the interactions between westerly winds and the Indian Monsoon over western China. Environ. Int. *124*, 294–301. https://doi.org/10.1016/j.envint.2018.12.057.

43. Zhou, Y., Yuan, G., Cong, Z., and Wang, X. (2021). Priorities for the sustainable development of the ecological environment on the Tibetan Plateau. Fundam. Res. *1*, 329–333. https://doi.org/10.1016/j.fmre.2021.03.006.

44. Casal, P., Zhang, Y., Martin, J.W., Pizarro, M., Jiménez, B., and Dachs, J. (2017). Role of snow deposition of perfluoroalkylated substances at coastal Livingston Island (Maritime Antarctica). Environ. Sci. Technol. *51*, 8460–8470. https://doi.org/10.1021/acs.est.7b02521.

45. Wells, M.R., Coggan, T.L., Stevenson, G., Singh, N., Askeland, M., Lea, M.-A., Philips, A., and Carver, S. (2024). Per-and polyfluoroalkyl substances (PFAS) in little penguins and associations with urbanisation and health parameters. Sci. Total Environ. *912*, 169084. https://doi.org/10.1016/j.scitotenv.2023.169084.

46. Young, C.J., Furdui, V.I., Franklin, J., Koerner, R.M., Muir, D.C.G., and Mabury, S.A. (2007). Perfluorinated acids in Arctic snow: New evidence for atmospheric formation. Environ. Sci. Technol. *41*, 3455–3461. https://doi.org/10.1021/es0626234.

47. Sheriff, I., Debela, S.A., Kabia, O.A., Ntoutoume, C.E., and Turay, M.J. (2020). The phase out of and restrictions on per-and polyfluoroalkyl substances: Time for a rethink. Chemosphere *251*, 126313. https://doi.org/10.1016/j.chemosphere.2020.126313.

48. Pickard, H.M., Criscitiello, A.S., Persaud, D., Spencer, C., Muir, D.C.G., Lehnherr, I., Sharp, M.J., De Silva, A.O., and Young, C.J. (2020). Ice core record of persistent short-chain fluorinated alkyl acids: Evidence of the impact from global environmental regulations. Geophys. Res. Lett. *47*, e2020GL087535. https://doi.org/10.1029/2020GL087535.

49. Muir, D., Gunnarsdóttir, M.J., Koziol, K., von Hippel, F.A., Szumińska, D., Ademollo, N., Corsolini, S., De Silva, A., Gabrielsen, G., and Kallenborn, R. (2025). Local sources versus long-range transport of organic contaminants in the Arctic: future developments related to climate change. Environ. Sci. Adv. *4*, 355–408. https://doi.org/10.1039/D4VA00240G.

50. Persaud, D., Criscitiello, A.S., Spencer, C., Lehnherr, I., Muir, D.C.G., De Silva, A.O., and Young, C.J. (2024). A 50 year record for perfluoroalkyl acids in the high arctic: implications for global and local transport. Environ. Sci. Proc. Imp. *26*, 1543–1555. https://doi.org/10.1039/D4EM00219A.

51. Wang, Z., Cousins, I.T., Scheringer, M., Buck, R.C., and Hungerbühler, K. (2014). Global emission inventories for C4-C14 perfluoroalkyl carboxylic acid (PFCA) homologues from 1951 to 2030, Part I: production and emissions from quantifiable sources. Environ. Int. *70*, 62–75. https://doi.org/10.1016/j.envint.2014.04.013.

52. Christiansen, J.S., Mecklenburg, C.W., and Karamushko, O.V. (2014). Arctic marine fishes and their fisheries in light of global change. Glob. Change Biol. *20*, 352–359. https://doi.org/10.1111/gcb.12395.

53. Yao, T., Bolch, T., Chen, D., Gao, J., Immerzeel, W., Piao, S., Su, F., Thompson, L., Wada, Y., Wang, L., et al. (2022). The imbalance of the Asian water tower. Nat. Rev. Earth Environ. *3*, 618–632. https://doi.org/10.1038/s43017-022-00299-4.

54. Zhou, Y., Zhuoga, S., Chen, Y., Wang, X., Fu, J., Zhou, W., and Gao, S. (2023). Optimizing the physiological pharmacokinetic model to rank the risks of persistent organic pollutants towards fish on the Tibetan Plateau. Sci. Total Environ. *893*, 164774. https://doi.org/10.1016/j.scitotenv.2023.164774.

55. Cook, K.L., Andermann, C., Gimbert, F., Adhikari, B.R., and Hovius, N. (2018). Glacial lake outburst floods as drivers of fluvial erosion in the Himalaya. Science *362*, 53–57. https://doi.org/10.1126/science.aat4981.

56. Patton, H., Hubbard, A., Heyman, J., Alexandropoulou, N., Lasabuda, A.P.E., Stroeven, A.P., Hall, A.M., Winsborrow, M., Sugden, D.E., Kleman, J., and Andreassen, K. (2022). The extreme yet transient nature of glacial erosion. Nat. Commun. *13*, 7377. https://doi.org/10.1038/s41467-022-35072-0.

57. Xiong, D. (2021). Bioaccumulation and Biomagnification of Perfluoroalkyl Substances (PFAS) in a Subarctic Ringed Seal Food Web in Lake Melville, Northern Labrador (Canada: University of Toronto (Canada)).

58. Boisvert, G., Sonne, C., Rigét, F.F., Dietz, R., and Letcher, R.J. (2019). Bioaccumulation and biomagnification of perfluoroalkyl acids and precursors in East Greenland polar bears and their ringed seal prey. Environ. Pollut. *252*, 1335–1343. https://doi.org/10.1016/j.envpol.2019.06.035.

59. Wiig, Ø., Amstrup, S., Atwood, T., Laidre, K., Lunn, N., Obbard, M., Regehr, E., and Thiemann, G. (2015). Ursus maritimus. The IUCN Red List of Threatened Species 2015. https://www.iucnredlist.org/species/22823/14871490.

60. AMAP (2021). Assessment 2020: POPs and chemicals of emerging arctic concern: influence of Climate Change. In Arctic Monitoring and Assessment Programme (AMAP) (Tromsø, Norway).

61. Bourquin, M., Peter, H., Michoud, G., Busi, S.B., Kohler, T.J., Robison, A.L., Styllas, M., Ezzat, L., Geers, A.U., Huss, M., et al. (2025). Predicting climate-change impacts on the global glacier-fed stream microbiome. Nat. Commun. *16*, 1264. https://doi.org/10.1038/s41467-025-56426-4.

62. Solomon, K.R., Velders, G.J.M., Wilson, S.R., Madronich, S., Longstreth, J., Aucamp, P.J., and Bornman, J.F. (2016). Sources, fates, toxicity, and risks of trifluoroacetic acid and its salts: Relevance to substances regulated under the Montreal and Kyoto Protocols. J. Toxicol. Environ. Health B *19*, 289–304. https://doi.org/10.1080/10937404.2016.1175981.

63. Zhou, Y., Wang, C., Dong, H., and Wang, X. (2024). Escalating global pollution of trifluoroacetic acid. Sci. Bull. *69*, 2483–2486. https://doi.org/10.1016/j.scib.2024.05.004.

64. Fabregat-Palau, J., Ershadi, A., Finkel, M., Rigol, A., Vidal, M., and Grathwohl, P. (2025). Modeling PFAS sorption in soils using machine learning. Environ. Sci. Technol. *59*, 7678–7687. https://doi.org/10.1021/acs.est.4c13284.

65. Hidalgo, A., and Mora-Diez, N. (2015). Novel approach for predicting partition coefficients of linear perfluorinated compounds. Theor. Chem. Acc. *135*, 18. https://doi.org/10.1007/s00214-015-1784-6.

66. Li, X., Wang, N., Ding, Y., Hawkings, J.R., Yde, J.C., Raiswell, R., Liu, J., Zhang, S., Kang, S., Wang, R., et al. (2022). Globally elevated chemical weathering rates beneath glaciers. Nat. Commun. *13*, 407. https://doi.org/10.1038/s41467-022-28032-1.

67. Rayne, S., and Forest, K. (2010). Theoretical studies on the pK∼ a∼ values of perfluoroalkyl carboxylic acids. Nat. Prec. *1*, 1. https://doi.org/10.1038/npre.2010.3829.2.

68. Rounce, D.R., Hock, R., Maussion, F., Hugonnet, R., Kochtitzky, W., Huss, M., Berthier, E., Brinkerhoff, D., Compagno, L., Copland, L., et al. (2023). Global glacier change in the 21st century: Every increase in temperature matters. Science *379*, 78–83. https://doi.org/10.1126/science.abo1324.

69. Tierney, J.E., Poulsen, C.J., Montañez, I.P., Bhattacharya, T., Feng, R., Ford, H.L., Hönisch, B., Inglis, G.N., Petersen, S.V., Sagoo, N., et al. (2020). Past climates inform our future. Science *370*, eaay3701. https://doi.org/10.1126/science.aay3701.

70. Wong, F., Shoeib, M., Katsoyiannis, A., Eckhardt, S., Stohl, A., Bohlin-Nizzetto, P., Li, H., Fellin, P., Su, Y., and Hung, H. (2018). Assessing temporal trends and source regions of per-and polyfluoroalkyl substances (PFASs) in air under the Arctic Monitoring and Assessment Programme (AMAP). Atmos. Environ. X. *172*, 65–73. https://doi.org/10.1016/j.atmosenv.2017.10.028.

71. Figuière, R., Miaz, L.T., Savvidou, E., and Cousins, I.T. (2025). An overview of potential alternatives for the multiple uses of per-and polyfluoroalkyl substances. Environ. Sci. Technol. *59*, 2031–2042. https://doi.org/10.1021/acs.est.4c09088.

72. Wang, Z., Cousins, I.T., Scheringer, M., Buck, R.C., and Hungerbühler, K. (2014). Global emission inventories for C4–C14 perfluoroalkyl carboxylic acid (PFCA) homologues from 1951 to 2030, part II: the remaining pieces of the puzzle. Environ. Int. *69*, 166–176. https://doi.org/10.1016/j.envint.2014.04.006.

73. Sha, B., Johansson, J.H., Salter, M.E., Blichner, S.M., and Cousins, I.T. (2024). Constraining global transport of perfluoroalkyl acids on sea spray aerosol using field measurements. Sci. Adv. *10*, eadl1026. https://doi.org/10.1126/sciadv.adl102.

74. Sha, B., Johansson, J.H., Tunved, P., Bohlin-Nizzetto, P., Cousins, I.T., and Salter, M.E. (2022). Sea spray aerosol (SSA) as a source of perfluoroalkyl acids (PFAAs) to the atmosphere: field evidence from long-term air monitoring. Environ. Sci. Technol. *56*, 228–238. https://doi.org/10.1021/acs.est.1c04277.

75. Altarawneh, M. (2021). A closer look into the contribution of atmospheric gas-phase pathways in the formation of perfluorocarboxylic acids. Atmos. Pollut. Res. *12*, 101255. https://doi.org/10.1016/j.apr.2021.101255.

One Earth, Volume *8*

Supplemental information

Global flux of perfluoroalkyl acids from glaciers in a warming climate

Yunqiao Zhou, Boyuan Hu, Xiaoping Wang, Jianjie Fu, Ian T. Cousins, Xi Bi, Lanxiang Wang, Mengke Chen, Chuanfei Wang, Huike Dong, Shaoting Ren, Zimeng Wang, Taicheng An, Dongfeng Li, Kevin C. Jones, and Derek C.G. Muir

Content

Supplemental Notes

Note S1. Partition coefficient (K_d) estimation by curve-fitting approaches and machine learning algorithms.

To predict the partition coefficient (K_d) of perfluoroalkyl acids (PFAAs) between water and suspended particles, curve-fitting approaches and machine learning (ML) algorithms were employed. The dataset used to train these models was compiled from newly measured data and previously published studies. This dataset comprised measured logK_d along with corresponding environmental parameters [water temperature (T_w), particulate organic carbon (POC), region types], and chemical properties [log$K_{ow\text{-}ionic}$, PFAA acid type (i.e., carboxylic and sulfonic acids)].

Given the diverse global water temperatures and the relatively low temperatures in glacial regions, it was essential to select data within a temperature range that closely reflects real-world conditions for the model. According to official estimates, sea surface temperatures in the Arctic Ocean could reach up to 18.6℃ under the SSP585 scenario for 2071-2100 (see https://climate-adapt.eea.europa.eu/en/metadata/indicators/sea-surface-temperature-1). Therefore, data from previous studies reporting water temperatures above 19℃ were excluded during data filtering. The final dataset consisted of previously published data (n=631) and the newly measured values from this study (n=140), categorized into three region types: glacial regions, inland watersheds, and coastal areas. Detailed data is listed in Table S4.

To evaluate and compare the model performance, three key metrics are employed: 1) R^2 score (R^2), which quantifies the proportion of variance in the target variable explained by the model; 2) Mean Squared Error (MSE), which measures the average squared difference between predicted and actual values (lower values indicate better performance); and 3) Mean absolute errors (MAE), which measures the average of the absolute differences and are used as performance for parameters tuning in the training and test sets. All models were implemented in Python 3.9.7 environment.

The step-by-step methodological workflow for tuning each model, including three curve-fitting approaches and four ML algorithms - support vector machine (SVM), decision tree (DT),

random forest (RF), and XGBoost - are detailed below:

(1) Curve-Fitting Approach

To model the relationship between logK_d and the other parameters in the dataset (Table S4), linear and polynomial functions were applied to the entire dataset. The c*urve_fit* function from *scipy.stats.optimize* was employed, and the three equations (Eq.1, 2 ,3) used were as follows. In each equation, a, b, c, and d represent the fitting coefficients.

- **Linear function**

$$\log K_d = a \times T_w + b \times \log K_{ow-ionic} + c \times \log POC + d \quad \text{(Eq. 1)}$$

Reason for use: Equation 1 represents a basic independent linear relationship between the feature variables (T_w, log$K_{ow\text{-}ionic}$, and logPOC) and logK_d. A linear model is often the first choice as it provides a simple and interpretable way to understand the relationship between variables. It assumes that each feature variable has a constant and independent effect on the response variable logK_d. This simplicity allows for a quick assessment of the direct influence of each variable on logK_d.

- **Polynomial function**

$$\log K_d = a \times T_w + (b_1 \times \log^3 K_{ow-ionic} + b_2 \times \log^2 K_{ow-ionic} + b_3 \times \log K_{ow-ionic}) + c \times \log POC + d \quad \text{(Eq. 2)}$$

Reason for use: Previous analysis indicated that there may or may not be a linear correlation between logK_d and log$K_{ow\text{-}ionic}$.[1] To account for potential non-linearity in the relationship between logK_d and log$K_{ow\text{-}ionic}$, Equation 2 was considered. By including higher-order terms of log$K_{ow\text{-}ionic}$ (cubic, quadratic, and linear), the model can capture more complex relationships that a simple linear model might miss. This allows for a more flexible fit to the data when the relationship between these two variables is not strictly linear.

$$\log K_d = (a_1 \times T_w{}^3 + a_2 \times T_w{}^2 + a_3 \times T_w) + (b_1 \times \log^3 K_{ow-ionic} + b_2 \times \log^2 K_{ow-ionic} + b_3 \times \log K_{ow-ionic}) + c \times \log POC + d \quad \text{(Eq. 3)}$$

Reason for use: When the water temperature (T_w) approaches 0, a phenomenon known as brine rejection occurs.[2] This suggests that the overall trend between logK_d and T_w might not be linear but monotonically increasing, in that, a cubic function would probe if there might be a saddle-like distort. Equation 3 takes this into account by including higher-order terms of T_w (cubic, quadratic, and linear) in addition to the higher-order terms of log$K_{ow\text{-}ionic}$. This allows the model to better capture the complex behavior of logK_d as T_w changes, especially near the critical temperature of 0.

Overall, curve-fitting approaches performed poorly on the entire dataset in all cases. Although increasing the model complexity (from Eq. 1 to Eq. 2 and then to Eq. 3) partially improved the explained variance, with R^2 values of 0.483, 0.594, and 0.636, respectively, the MAE values remained high (0.553, 0.524, and 0.521). This high MAE indicates that the parameters contribute to the logK_d interdependently and cannot be well-explained by linear or polynomial functions with independent terms. As a result, machine learning (ML) algorithms were applied to achieve better logK_d predictions.

(2) Machine Learning Algorithms

- **Support Vector Machine (SVM) model**

Model construction and hyperparameter tuning. The SVM model was constructed using the *sklearn.svm.SVR* module from the Scikit-learn library. To fine-tune its hyperparameters, the *GridSearchCV* algorithm with a 5-fold cross validation strategy was employed. The hyperparameters under optimization were 'C', 'degree', 'gamma' and 'tol'. The detailed list of candidate values for these hyperparameters is provided in Text S1-Table 1.

Note S1-Table 1. Candidate parameter values for gird search in Support Vector Machine hyperparameter tuning.

Hyperparameters	Values
C	0.001, 0.01, 0.03, 0.1, 0.3
degree	2, 3, 4, 5
gamma	0.001, 0.01, 0.03, 0.1, 0.3
tol	0.001, 0.01, 0.03, 0.1, 0.3

Note: This table lists the potential tuning values for the hyperparameters 'C', 'degree', 'gamma', and 'tol' used in the grid search process to optimize the SVM model. These values serve as the search space for identifying the optimal configuration.

Model performance evaluation and parameter selection. To evaluate the model performance, the MAE and its standard deviation across the five cross-validations folds were plotted. The results showed a clear trend: models with a lower standard deviation generally had a lower MAE. This relationship implies that greater model stability is often associated with higher predictive accuracy. To balance predictive accuracy and model stability, the grid parameter configuration corresponding to the 5th lowest MAE and the 4th lowest standard deviation was selected as the best-fitting setup. The visual representation of this selection process can be seen in Note S1-Figure 1, green dot.

Final optimized model. The final optimized parameters were determined as 'C'=0.03, 'degree'=4, 'gamma'=0.3, and 'tol'=0.03. When applied to the test set, the optimized model achieved an MAE of 0.3783, demonstrating relatively good predictive performance (Note S1-Figure 1, green dot with red edge).

- **Decision Tree (DT) model**

Model construction and hyperparameter tuning. The DT model was implemented using *sklearn.tree.DecisionTreeRegressor* from the Scikit-learn library. Hyperparameter optimization was conducted via *GridSearchCV* with a 5-fold cross-validation strategy. The tuning process involved four hyperparameters: 'max_depth', 'min_samples_split', 'min_samples_leaf', and 'min_weight_fraction_leaf'. A total of 1,350 parameter grids (derived from the Cartesian product of candidate values) were tested. The hyperparameters search space is detailed in Note

S1-Table 2.

Note S1-Table 2. Candidate parameter values for gird search in Decision Tree hyperparameter tuning.

Hyperparameters	Values
max_depth	4, 5, 6, 7, 8, 9, 10, 11, 12
min_samples_split	2, 3, 4, 5, 6
min_samples_leaf	1, 2, 3
min_weight_fraction_leaf	0, 0.1, 0.2, 0.3, 0.4, 0.5, 0.6, 0.7, 0.8, 0.9

Note: This table lists the candidate values for hyperparameters optimized via grid search in the Decision Tree (DT) model. The search space comprises 9 ('max_depth') × 5 ('min_samples_split') × 3 ('min_samples_leaf') × 10 ('min_weight_fraction_leaf') = 1,350 unique parameter combinations.

Model performance evaluation and parameter selection. Model performance was evaluated by plotting the MAE and its standard deviation across cross-validations folds. Top-performing models showed tightly clustered MAE scores but exhibited stability variations (standard deviation: 0.010-0.037). To balance predictive accuracy and stability, the grid configuration corresponding to the 98th lowest MAE (to avoid overfitting to the validation data) and the 1st lowest standard deviation (maximum stability) were selected as optimal (see Note S1-Figure 1, salmon red dots).

Final optimized model. The final optimized DT model parameters are 'max_depth'=7, 'min_samples_leaf'=1, 'min_samples_split'=5, 'min_weight_fraction_leaf'=0. This configuration achieved an MAE of 0.2980 on the test set (Note S1-Figure 1, salmon red dots with red edge).

- **Random Forest (RF) model**

Model construction and hyperparameter tuning. The RF model was constructed using the *sklearn.ensemble.RandomForestRegressor* from the Scikit-learn library. Hyperparameter optimization was carried out via GridSearchCV algorithm with a 5-fold cross-validation strategy. The hyperparameters under optimization were 'max_depth', 'min_samples_split', 'min_samples_leaf', and 'n_estimators'. The candidate values for these hyperparameters are presented Note S1-Table 3. Additionally, the parameter, 'boost_trap' was set for all the tested

grids (Note S1-Figure 1, steel blue dots). In total, 810 parameter grids were tested.

Note S1-Table 3. Candidate parameter values for gird search in Random Forest hyperparameter tuning.

Hyperparameters	Values
max_depth	4, 5, 6, 7, 8, 9, 10, 11, 12
min_samples_split	2, 3, 4, 5, 6
min_samples_leaf	1, 2, 3
n_estimators	50, 60, 70, 80, 90, 100

Note: This table lists the candidate values for the hyperparameters used in the grid search to tune the Random Forest model. The combination of these values forms the 810 parameter grids that were tested.

Model performance evaluation and parameter selection. To evaluate the model's performance, the MAE and their standard deviation across the five cross-validation folds were plotted. A clear trend was observed: smaller standard deviations were associated with lower MAE values. The best-performing grid points were closely clustered, yet there was significant variance in their stability. For MAE values less than 0.2564, the standard deviation ranged from 0.0104 to 0.0182 for MAE<0.2564. To balance predictive accuracy and model stability, the grid point corresponding to the 118th lowest MAE and 1st lowest standard deviation was selected as the optimal configuration.

Final optimized model. The final optimized parameters for the RF model are as follows: 'max_depth'=12, 'min_samples_leaf'=1, 'min_samples_split'=6, 'n_estimators'=90. When applied to the test set, this optimized model achieved an MAE of 0.2555 (Note S1-Figure 1, steel blue dots with red edge).

- **Extreme Gradient Boost (XGBoost)**

Two-Step Hyperparameter Tuning Strategy. The XGBoost model was optimized using a hybrid approach: initial tuning with the scikit-learn API (for rapid parameter screening) followed by fine-tuning with the Learning API (for advanced parameter control). This strategy addressed the trade-off between computational efficiency (scikit-learn API) and comprehensive

parameter optimization (Learning API).

Step 1: Initial Tuning with scikit-learn API

Model construction and hyperparameter tuning. Hyperparameters were tuned using *GridSearchCV* with 5-fold cross-validation. The search space included 'max_depth', 'eta', 'gamma', 'subsample', 'lambda' and 'alpha'. The parameter 'n_estimators' was fixed at 100 for all test grids. The specific candidate values for those parameters in grid search are listed in Note S1-Table 4. In total, 10,080 parameter grids were tested, as shown in Note S1-Figure 1, gold dots.

Note S1-Table 4. Candidate parameter values for gird search in XGBoost tuning (scikit-learn API).

Hyperparameters	Values
max_depth	5, 6, 7, 8, 9, 10
eta	0.1, 0.13, 0.16, 0.19
gamma	0.01, 0.02, 0.03
subsample	0.2, 0.3, 0.4, 0.5, 0.6, 0.7, 0.8
lambda	0, 0.1, 0.2, 0.3, 0.4
alpha	0, 0.01, 0.03, 1
n_estimators	100

Note: This table lists the candidate values for the hyperparameters used in the grid search to tune the Extreme Gradient Boost model. The combination of these values forms the 10,080 parameter grids that were tested.

Model performance evaluation and parameter selection. To evaluate the model performance, the MAE and its standard deviation across the five cross-validations were analyzed. The best-performing grids (MAE<0.2564) were closely clustered, but there was significant variation in their stability. The standard deviation of MAE for these grids ranged from 0.0051 to 0.0328 when MAE<0.2564.

Two specific grid points were selected for further tuning: 1) XGB_A, this grid corresponded to the 1st lowest MAE and the 2757th lowest standard (Note S1-Figure 1, gold dots with red edge). The parameter grid for XGB_A in the scikit-learn API was 'alpha'=0.03, 'eta'=0.1, 'gamma'=0.03, 'lambda'=0.3, 'max_depth'=7, 'subsample'=0.7, achieving an average MAE of 0.2346 and an MAE standard deviation of 0.0166; 2) XGB_B, this grid corresponded to the 572nd lowest MAE, 220th lowest standard deviation (Note S1-Figure 1, gold dots with red edge).

The parameter grid for XGB_B in the scikit-learn API was ‘alpha’=0.03, ‘eta’=0.1, ‘gamma’=0.02, ‘lambda’=0.4, ‘max_depth’=7, ‘subsample’=0.7, achieving an average MAE of 0.2399 and an MAE standard deviation of 0.0122.

Step 2: Fine-Tuning with Learning API

Model construction and hyperparameter tuning. In the Learning API, the parameters ‘colsample_bynode’, ‘learning_rate’, and ‘min_child_weight’ were turned through grid searching. The paramters ‘reg_lambda’, ‘reg_alpha’, ‘subsample’, ‘num_parallel_tree’, ‘max_depth’, and ‘gamma’, were fixed based on the two grid points selected in the scikit-learn API. The specific candidate values for the tunable parameters are listed in Note S1-Table 5.

Note S1-Table 5. Candidate parameter values for gird search in XGBoost tuning (Learning API).

Parameter	Values	
	XGB_A	XGB_B
colsample_bynode	0.1, 0.2, 0.3, 0.4, 0.5, 0.6, 0.7, 0.8, 0.9, 1	
learning_rate	0.003, 0.1, 0.3, 0.6, 1	
min_child_weight	1, 6, 11, 16, 21, 26	
num_boost_round	1000	
early_stopping_rounds	3	
reg_alpha	0.03	
subsample	0.7	
num_parallel_tree	100	
max_depth	7	
reg_lambda	0.3	0.4
gamma	0.03	0.02

For each gird configuration, the dataset was split using *sklearn.model_selection.train_test_split*, with 30% of the data allocated as the test set and a fixed random state to ensure reproducibility (training set: test set = 7:3). The MSE, MAE and R^2 score were recorded for both the training and test sets.

Parameter Selection and Final Performance (Note S1-Figure 2)**.** For XGB_A, the grid corresponding to the 13th lowest MAE of the test set was chosen. The optimized parameters were 'colsample_bynode'=0.8, 'learning_rate'=0.1, 'min_child_weight'=6, 'num_boost_round'=1000, 'early_stopping_rounds'=3, 'reg_alpha'=0.03, 'subsample'=0.7, 'num_parallel_tree'=100, 'max_depth'=7, 'reg_lambda'=0.3, 'gamma'=0.03, achieving a MAE of 0.2389 on the test set. For XGB_B, the grid corresponding to the 1st lowest MAE of the test set was selected. The optimized parameters were 'colsample_bynode'=1, 'learning_rate'=0.03, 'min_child_weight'=6, 'num_boost_round'=1000, 'early_stopping_rounds'=3, 'reg_alpha'=0.03, 'subsample'=0.7, 'num_parallel_tree'=100, 'max_depth'=7, 'reg_lambda'=0.4, 'gamma'=0.02, achieving a MAE of 0.2519 on the test set.

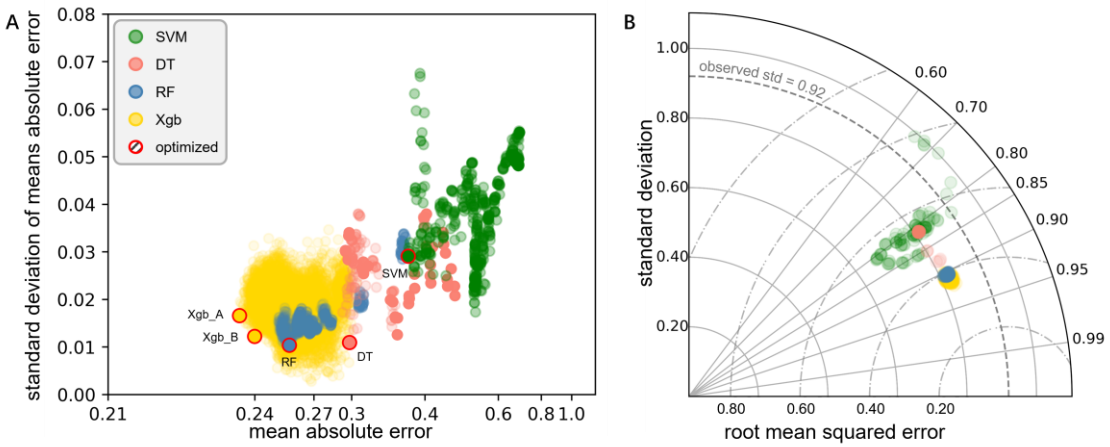

Note S1-Figure 1. Performance of tested machine learning methods by grid searching.
Note: A, scattering diagram of average mean absolute errors and standard deviations at 5-fold cross validation. The points corresponding to top 100 SVMs, top 100 DTs, top 250 RFs, and top 250 XGboost (Xgb) scored (minimum mean absolute error) models were scattered, of which the optimized models for each set were red circled. B, Tylor diagram of top 100 SVMs, top 100 DTs, top 250 RFs, and top 250 Xgb scored models. In terms of both mean absolute error and root mean squared error, Xgb models could achieve better performance than those of other 3 structures.

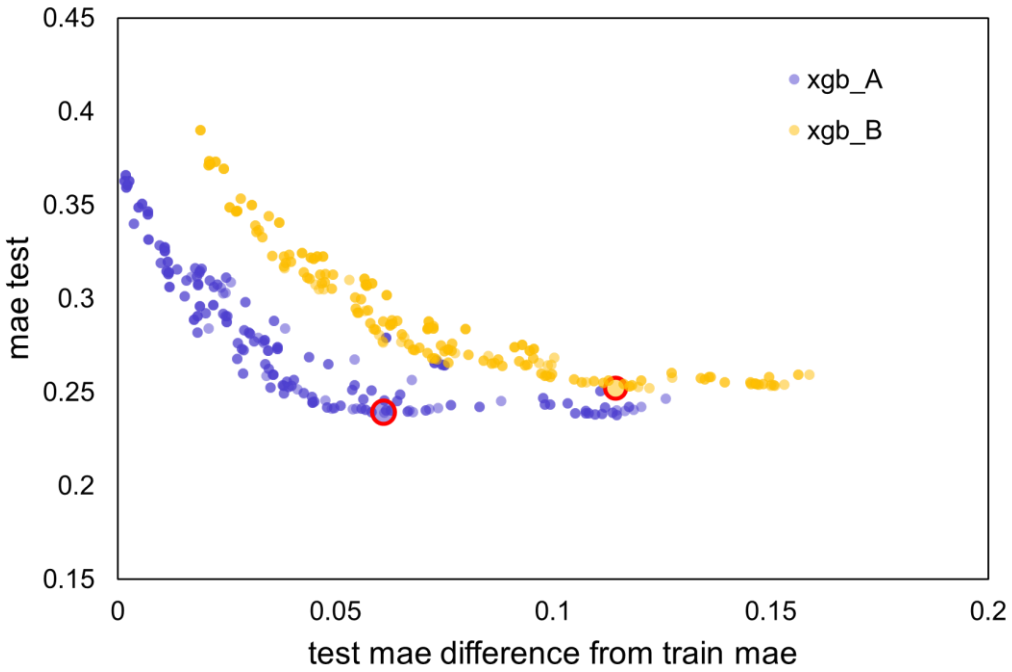

Note S1-Figure 2. Relationship between test set average mean absolute errors (MAE) and difference between test of MAE and train MAE.
Note: Under a fixed random splitting of the dataset, both XGB_A and XGB_B were further tuned based on the parameter grids obtained from the scikit-learn API. The red circled point refers to the local minimum of the test set MAE during the tuning of XGB_A, and that of XGB_B. Comparing the top 100 highest-scoring parameter grids of XGB_A and XGB_B, the

average test set MAE of XGB_A is 0.040 lower than that average of XGB_B ($p<0.0001$), suggesting that XGB_A is more robust than XGB_B.

Performance comparison of Machine Learning algorithms using Monte Carlo cross-validation

Optimized models —including SVM, DT, RF, and XGBoost (XGB_A and XGB_B)— were compared using 100-fold Monte Carlo cross-validation with test-to-train ratios ranging from 5:95 to 50:50. Performance metrics (R^2 score, MAE and MSE) across all models are summarized in Note S1-Figure 3, with detailed data listed in Note S1-Table 6.

Among the models, RF and XGBoost consistently outperformed DT and SVM across all validation scenarios. XGBoost outperformed RF in all cases except for one validation (test-to-train ratio=5:95), where no statistically significant difference was observed across six evaluation metrics (Student' t-test, $\alpha=0.05$) (Note S1-Figure 3). The stable performance of the RF and XGBoost model suggests that they are neither underfitted nor overfitted.

Final model selection. When comparing the test set performance scores, XGB_A and XGB_B exhibited nearly identical performance ($t<0.102$, $p>0.460$ for MAE; $t<0.117$, $p>0.453$ for MSE; $t<0.152$, $p>0.440$ for R^2). However, in terms of training set performance, XGB_B exhibited a closer consistency between training and test set performance compared to XGB_A (Note S1-Table 6). Finally, the XGB_B model was selected as the final model and trained by the whole dataset.

Model limitations. While the model successfully captured $\log K_d$ patterns using up to 5 parameters, a persistent performance gap between training and test sets —largely invariant to test size reduction—suggests unresolved noise unrelated to the selected features. Nevertheless, the model reduced $\log K_d$ variance to 0.24, sufficient for subsequent Monte Carlo simulations. This residual uncertainty aligns with known measurement variability in PFAA concentrations for suspended particles, rather than inherent model limitations.

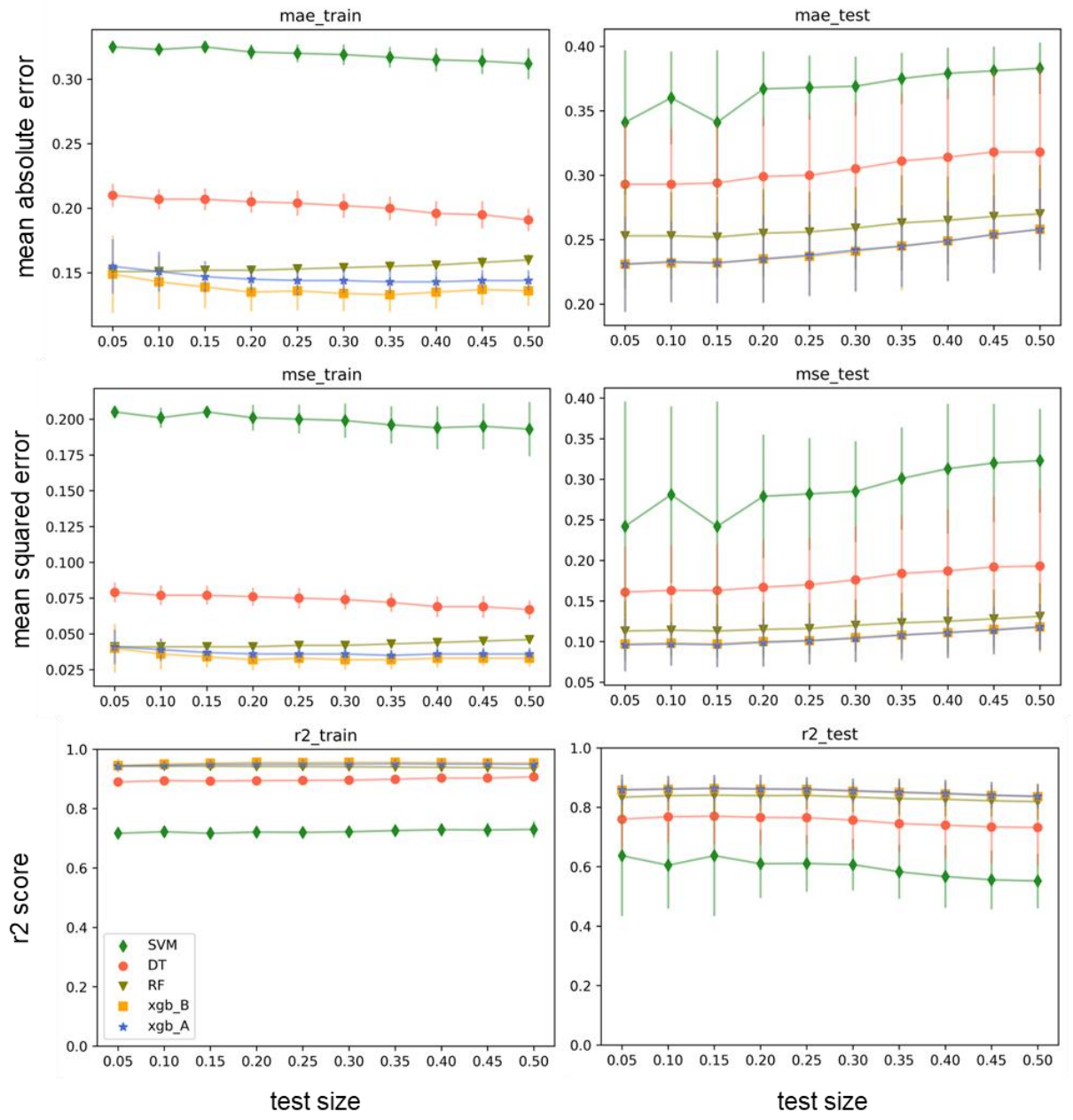

Note S1-Figure 3. Performance comparison of optimized Machine Learning algorithms across different metrics.

Note: The optimized models-SVM, DT, RF, XGBoost(A&B)-were evaluated using Monte Carlo cross-validated in ten different training and test set ratios for 30 times each. In each sub-diagram, scattered points represent the average value, and the vertical lines represent the ± 1 standard deviation.

Note S1-Table 6. Performance metrics (R^2, Mean Squared Error (MSE), Mean absolute errors (MAE)) on the training and test sets for the optimized machine learning models.

Model	Metric	R^2_train	R^2_test	MSE_train	MSE_test	MAE_train	MAE_test
XGB_A	Average	0.949	0.854	0.037	0.104	0.146	0.242
	SD	0.008	0.045	0.006	0.029	0.012	0.032
XGB_B	Average	0.953	0.853	0.034	0.105	0.138	0.241
	SD	0.011	0.046	0.008	0.030	0.016	0.032
RF	Average	0.941	0.832	0.042	0.120	0.154	0.259
	SD	0.003	0.054	0.002	0.035	0.003	0.035
DT	Average	0.897	0.754	0.074	0.176	0.202	0.305
	SD	0.010	0.102	0.007	0.068	0.009	0.052
SVM	Average	0.723	0.596	0.199	0.287	0.319	0.366
	SD	0.013	0.254	0.009	0.185	0.006	0.060

Note: SD represents the standard deviation.

Note S2. Extraction of PFAAs from water samples.

All the water samples, including glacial runoff, lake water and surface snow/ice (after natural melting), were filtered through Whatman glass fiber filters (GFF, 0.7 μm). Two liters (2L) of each filtered sample were spiked with 2000 pg of internal standards and then subjected to solid-phase extraction using Waters Oasis WAX cartridges (150 mg, 6 cm^3, 30 μm) as described in our previous study.[3] After preconditioning with 5 mL of methanol and 5 mL of distilled Milli-Q water, the solid-phase extraction cartridge was loaded with the water sample and eluted at about one to two drops per second. Each cartridge was then washed with 0.1% acetic acid and dried for 20 min under vacuum. The cartridges and filters were wrapped in Aluminum foil and sealed in airtight containers before storing at −20°C until elution. Before elution, each cartridge was air-dried for 30 min under vacuum. For this operation, an additional WAX cartridge was connected to the top of the sample cartridge to ensure that the air stream was free of PFAAs. The analytes were eluted from the WAX cartridges using 10 mL of methanol with 0.1% ammonium hydroxide. The extracts were then concentrated to 200 μL under a gentle nitrogen flow.

Note S3. Extraction of PFAAs from suspended particle samples.

The PFAAs in suspended particles were extracted with methanol following a previously published method with minor modifications.[4] In brief, the weighed and air-dried (in a natural state) suspended particle samples were spiked with 2000 pg of internal standards and placed into a 50-mL polypropylene centrifuge tube. Following the addition of 10 mL of methanol, the samples were shaken for 2 min to mix evenly, sonicated at 60°C for 30 mins, and then centrifuged at 6000 rpm for 15 min. The supernatant was then transferred to another tube. This process was performed in triplicate. The supernatants were combined (about 30 mL) and concentrated to 1−2 mL under a gentle nitrogen flow before dilution with 50 mL of Milli-Q water. The diluted sample was then loaded onto a preconditioned WAX cartridge and extracted using the same method as for the water samples.

Note S4. Instrumental analysis of target PFAAs in extracts.

The instrumental analysis procedure has been reported previously.[3,5] The extract (10 μL) was injected into an Acclaim 120 C18 column (5 μm, 100 Å, 150 mm × 4.6 mm) coupled with a ThermoFisher Scientific UltiMate TM 3000 dual-gradient high-performance liquid chromatography system and a ThermoFisher Scientific TSQ Quantiva triple quadrupole mass spectrometer. The mobile phases were (A) 10 mM ammonium acetate (pH 4) and (B) acetonitrile. The flow rate was set at 1 mL min^{-1}. The mobile phase gradient started at 10% B, held constant for 1.5 min, increased to 95% by 4 min, held constant until 8 min, returned to the initial condition by 8.5 min, and then balanced for 1.5 min. The mass spectrometer was operated in the negative ion electron spray ionizer mass spectrometry/mass spectrometry multiple reaction monitoring mode. The mass spectrometry parameters were set as follows: sheath gas, 40 units; auxiliary gas, 12 units; source voltage, 2500 V; vaporizer temperature, 350°C; capillary temperature, 400°C; and scan time, 0.01 s. Quantification was performed using the response factors calculated and applied to a seven-point calibration graph ranging from 0 to 20 ppb for individual analytes. All the target analytes are listed in Table S1.

Note S5. Quality assurance and quality control.

All the analytical procedures were monitored using strict quality assurance/control measures. To reduce contamination from the experimental equipment, contact with the vessel and fluorine-containing materials was avoided during the experimental and analytical processes. Field blanks and procedural blanks for water and suspended particle samples were diluted using Milli-Q water and clean fiber filters were used as alternative samples to monitor contamination during sample collection and solid-phase extraction. The analytes detected in the field blanks are listed in Table S12. The compounds were classified as not found when the signal-to-noise ratio (S/N) was <3. The method quantification limits (MQLs) were defined as the mean concentration of the procedural blanks plus three times the standard deviation of the blank response. If the chemicals were classified as not found in the blanks, then the MQLs were calculated with an S/N ratio of 10. The MQL ranges of all the targets are given in Table S12 and were similar to those reported previously.[6] The blank test indicated that the field sampling and experimental procedures did not result in contamination of the samples. Mean recoveries ranged from 52% to 81% and 42% to 70% for the water and suspended particle samples, respectively (Table S13). All the results were recovery-corrected.

Note S6. Monte Carlo simulation to the estimated release fluxes for PFAAs.

To estimate the virtual PFAA release fluxes in water phase and on suspended particles in eight glacier regions, Monte Carlo simulations (MCS) were performed to evaluate the mean values of fluxes and the uncertainties.

The MCS for PFAA release fluxes in the water phase contained 3 steps: 1) calibration of monthly precipitation, subregional air temperature, and effective glacier area by measured or documented data, 2) evaluation of monthly glacier runoff volume, and 3) computation of PFAA fluxes in water phase. Calibration of monthly precipitation was based on monthly precipitation data, the fifth generation of European Reanalysis (ERA5-Land) dataset published on the Climate Data Store (ERA5-Land monthly averaged data from 1950 to present (copernicus.eu)), including maximum, minimum, average, and standard deviation, which were assumed as the precipitation in 2020. The annual precipitation, as well as the corresponding standard deviations of annual participation from 2020 to 2100 found by SSP126, SSP245, and SSP585. The calibrated maximum, minimum, average, and standard deviation of each year were found by following equations:

$$\overline{p}_{c(m,year)} = (\overline{\mathrm{P}}_{SSP(year)} - \overline{\mathrm{P}}_{SSP(2020)})/12 + \overline{p}_{meas(m,2020)} \quad (5)$$

$$\delta p_{c(m,year)} = \frac{\delta \mathrm{P}_{SSP(year)}}{\delta \mathrm{P}_{SSP(2020)}} \times \delta p_{meas(m,2020)} \quad (6)$$

$$p_{\min,c(m,year)} = \max\left(\frac{\delta \mathrm{P}_{SSP(year)}}{\delta \mathrm{P}_{SSP(2020)}} \times (p_{\min,meas(m,year)} - \overline{p}_{meas(m,2020)}) + \overline{p}_{c(m,year)}, 0\right) \quad (7)$$

$$p_{\max,c(m,year)} = \frac{\delta \mathrm{P}_{SSP(year)}}{\delta \mathrm{P}_{SSP(2020)}} \times (p_{\max,meas(m,year)} - \overline{p}_{meas(m,2020)}) + \overline{p}_{c(m,year)} \quad (8)$$

where $p_{\min,c(m,year)}$, $p_{\max,c(m,year)}$, $\overline{p}_{c(m,year)}$, and $\delta p_{c(m,year)}$ are the calibrated monthly minimum, maximum, average and standard deviations of precipitation (mm) at given month and year, $(m, year)$, and likewise, the $p_{\min,meas(m,year)}$, $p_{\max,meas(m,year)}$, $\overline{p}_{meas(m,year)}$, and $\delta p_{meas(m,year)}$ are the monthly minimum, maximum, average and standard deviations of

precipitation (mm) at given month and year available in the Coupled Model Intercomparison Project 6 (CMIP6) datasets. The $\overline{\mathrm{P}}_{SSP(year)}$ and $\delta\mathrm{P}_{SSP(year)}$ are the annual average and standard deviations of precipitation found by SSP126, SSP245, or SSP585 in given year.

The subregional average summer air temperature and the annual average air temperature were assumed to rise equally through 2020 to 2100, while the pinpoint for calibration were the summer and annual average air temperature in 2020 evaluated by ERA5-Land dataset. Following computation were conducted,

$$T_{air,c(subregion,year)} = T_{air,meas(subregion,2020)} + T_{air,SSP(region,year)} - T_{air,SSP(region,2020)} \quad (9)$$

where the T_{air} referred to either the summer average temperature or annual average temperature (°C), and the subscribe *c*, *meas* and *SSP* referred to calibrated results, measured value in ERA5-Land dataset for year 2020, and simulated results by SSP126, SSP245, or SSP585, respectively. The *subregion* is under the corresponding category of the *region*. The uncertainty of the summer average temperature and annual average temperature were kept the same for all 80 years.

The effective glacier areas were calibrated based on measured annual average glacier runoff fluxes and the mean values of the simulated annual glacier runoff fluxes of each region. Effective factors for each region were computed as

$$r_{region} = \frac{\bar{\Phi}_{meas,region}}{\bar{\Phi}_{simed,region}} \quad (10)$$

where $\bar{\Phi}_{meas,region}$ (kg year^{-1}) were the average glacier runoff fluxes in given region, and $\bar{\Phi}_{simed,region}$ was the mean value of glacier runoff fluxes in given region in 2500 Monte Carlo simulations which were based on the method proposed by Bliss et al., with initial value of r_{region} as 1. The evaluated r_{region} are 0.7873, 2.9036, 4.2978, 0.1937, 4.1656, 3.2891, 1.0773, and 0.0049 for West Canada and USA, Arctic Canada, Greenland, Arctic Europe, North Asia, Central Europe, South and Central Asia, and Antarctic and Subantarctic ice sheet, respectively. The effective glacier area is the area measure in the version 6.0 of the RGI

(http://www.glims.org/RGI/) multiplied by the effective factor.

The monthly glacier runoff fluxes in each subregion were evaluated by Monte Carlo simulations of the method proposed by Bliss et al. 2500 simulations were conducted for each year, where the precipitation and the air temperature were randomly elected based on the gaussian distribution with corresponding mean value and standard deviation of the monthly precipitations and air temperatures. Since the precipitation should not be less than zero, if a negative precipitation was elected, an alternative election would replace it. In addition, the snow-ice melting index, $f_{snow/ice}$, was determined by the sample type. Those elected monthly precipitation, air temperature, and the melting index, were used in the flow work proposed by Bliss et al., as it has been described in the Glacier Runoff Model.

The annual PFAA fluxes of each region in water were the sum of its monthly fluxes. For each subregion there were 2500 samples randomly elected to extract the representative PFAA concentrations. The subregion they belonged to, as well as their sample type, were recorded, thereby the glacier runoff fluxes could associate with PFAA concentration by subregion and sample types. The monthly PFAA fluxes ($\Phi_{w-PFAS(m)}$, kg year^{-1}) were computed as follows

$$\Phi_{w-PFAS(m)} = \sum_{m=0}^{11} \sum_{\text{subregion} \in \text{region}} \Phi_{GR(m,\text{subregion,sample})} \times C_{w-PFAS(\text{sample})} \quad (11)$$

The $C_{w-PFAS(\text{sample})}$ (pg L^{-1}) is the corresponding PFAA concentration of the elected sample, and the $\Phi_{GR(m,\text{subregion,sample})}$ (km^3 year^{-1}) are the monthly glacier runoff fluxes of the *subregion* where the *sample* elected for that concentration in water belong to.

The MCS for PFAA release fluxes on suspended particles contained 5 steps: 1) calibration of monthly precipitations, monthly average air temperature, and effective glacier area by measured or documented data, 2) simulations for monthly environmental descriptors of logPOC, POC, and water temperature, 3) evaluation of monthly logK_d by optimized XGBoost algorithm, 4) evaluation of monthly glacier runoff volume, and 5) computation of PFAA fluxes on suspended particles. The calibration in the first step, the glacier runoff volume evaluation in fourth step, and annual PFAA flux calculation in final step were the same to the first, second, and third step for MCS for water phase, respectively.

The average concentrations of suspended particles (ACSP, mg L^{-1}) were fixed within each subregion (Table 1). The water temperatures were randomly elected based on gaussian distribution with mean value 2.5℃, and standard deviation 0.1℃. The results of MCS for PFAA fluxes in water phase and those for PFAA fluxes in suspended particles are in Table S6.

Of note, although we collected PFAAs from all glacial regions worldwide, even including some data from seawater neighboring the glaciers, PFAA concentration data are currently not available for large glaciers in Patagonia and the southern Andes. Glaciers in these regions are among the most rapidly retreating on Earth and this lack of data is likely to lead to an underestimation of the global release of PFAAs from glacial regions.

Note S7. PFAA levels in atmospheric particulate matter in remote regions

To date, the only long-term atmospheric observation in remote areas was conducted under the Arctic Monitoring and Assessment Programme (AMAP). From 2006 to 2015, air samples were collected at the Canadian High Arctic station of Alert, Nunavut, Canada (82°30′N, 62°20′W), the Norwegian-operated stations of Zeppelin, Svalbard, Norway (78°54′N, 11°53′E) and Andøya, Norway (62°16′N, 16°0′E) to monitor the variation of atmospheric PFAA levels.[7]

As perfluorooctane sulfonic acid (PFOS) was the first PFAA compound regulated under the Stockholm Convention, it might serve as a key indicator for the fluctuations of PFAA compounds in the atmosphere. Accordingly, Note S2-Figure 1 illustrates the seasonal variations and trends of PFOS at these three Arctic stations. PFOS levels at Alert are on the rise, with doubling times ranging from 2.5 to 3.7 years. In contrast, PFOS levels at Zeppelin exhibit an exceptional prolonged half-life ($t_{1/2}$) of 67 years. Meanwhile, at Andøya, PFOS concentrations are slowly decreasing with a $t_{1/2}$ of 11 years.

These data suggest that the concentrations of PFOS in the polar atmosphere have experienced a slight increase or slow decrease over recent years. This is not surprising because although the use of PFOS and its precursors have been largely phased out globally, they are still stored in stockpiles or being slowly released from products still in use, environmental media and waste streams (e.g., landfills). Moreover, there could well be a longer time-lag in concentration declines for PFOS in remote locations in response to the emission reductions in source regions. If the occurrence of PFAAs in remote locations is result of long-range oceanic transport,[8,9] and remobilization to the atmosphere in sea spray aerosol,[10,11] it will take many years for the atmospheric concentration to decline since long-range ocean transport is a slow process of the order of several years to decades, depending on the location of the source region.

In our expert opinion, given the multiple transport pathways for PFOS, atmospheric deposition of PFOS will continue in remote regions for the coming decades, resulting in a relatively stable concentration.

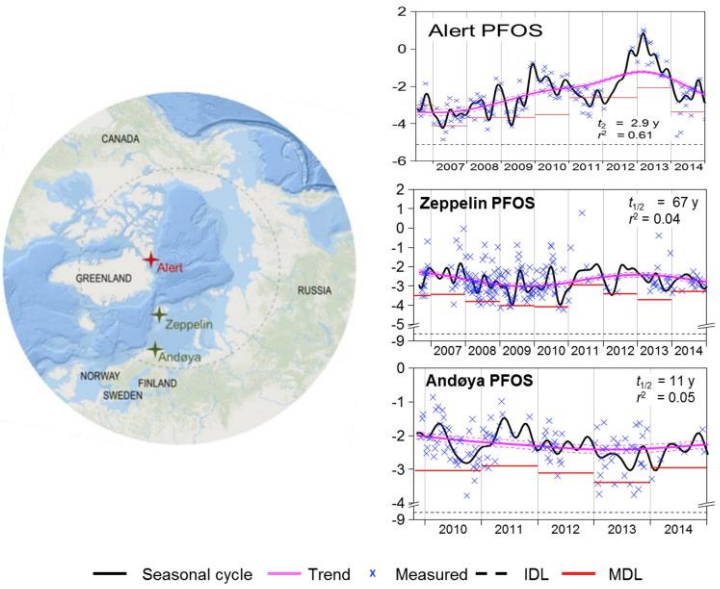

Note S7-Figure 1. Seasonal cycles and trends of PFOS in Alert, Zeppelin, Andoya.
Note: Doubling times (t_2) or half-lives ($t_{1/2}$) are shown in units of years (y). The measured data are shown as blue crosses, the black line is the seasonal cycle, and the pink line is the trend derived from the Digital Filtration model. Dash pink lines indicate the lower and upper 95% confidence limits of the trend. r^2 indicates the correlation coefficient between the trend and measured data. r^2 is only shown for statistically significant correlations at 95% confidence. The instrumental detection limit (IDL) and method detection limit (MDL) are shown as dash black and red lines, respectively. This figure is reproduced from Wong et al. (2018) [7] with permission under the CC BY-NC-ND license.

Supplemental Tables

Table S1. Physical and chemical parameters of the 13 PFAAs analyzed in this study.

Analyte	Acronym	CAS No.	Formula	Carbon chain length	Molecular structure	log$K_{ow\text{-}ionic}$[12]
Perfluorocarboxylic acids (PFCAs)						
Perfluorobutanoic acid	PFBA	375-22-4	C_3F_7COOH	C4	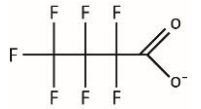	-2.78
Perfluoropentanoic acid	PFPeA	2706-90-3	C_4F_9COOH	C5	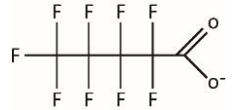	-2.25
Perfluorohexanoic acid	PFHxA	307-24-4	$C_5F_{11}COOH$	C6	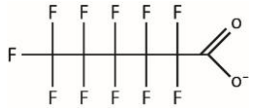	-1.78
Perfluoroheptanoic acid	PFHpA	375-85-9	$C_6F_{13}COOH$	C7	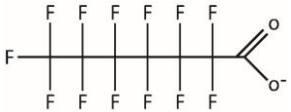	-1.23
Perfluoro-octanoic acid	PFOA	335-67-1	$C_7F_{15}COOH$	C8	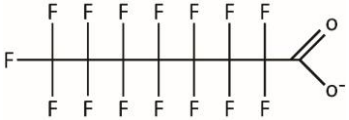	-0.76
Perfluorononanoic acid	PFNA	375-95-1	$C_8F_{17}COOH$	C9	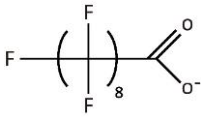	-0.25
Perfluorodecanoic acid	PFDA	335-76-2	$C_9F_{19}COOH$	C10	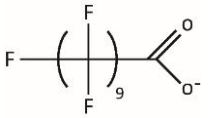	0.31

Analyte	Acronym	CAS No.	Formula	Carbon chain length	Molecular structure	log$K_{ow\text{-}ionic}$[12]
Perfluoroundecanoic acid	PFUdA	2058-94-8	$C_{10}F_{21}COOH$	C11	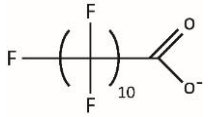	0.79
Perfluorododecanoic acid	PFDoA	307-55-1	$C_{11}F_{23}COOH$	C12	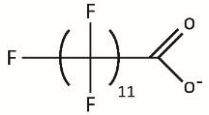	1.37
Perfluorotridecanoic acid	PFTrDA	72629-94-8	$C_{12}F_{25}COOH$	C13	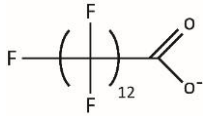	1.90
Perfluoroalkane sulfonic acids (PFSAs)						
Perfluorobutane sulfonic acid	PFBS	375-73-5	$C_4F_9SO_2O^-$	C4	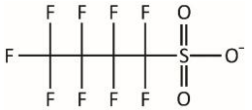	-3.55
Perfluorohexane sulfonic acid	PFHxS	355-46-4	$C_6F_{13}SO_2O^-$	C6	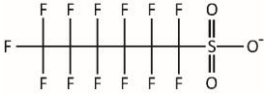	-2.50
Perfluorooctane sulfonic acid	PFOS	1763-23-1	$C_8F_{17}SO_2O^-$	C8	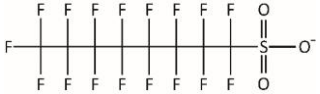	-1.49

Table S2. Dataset of the individual and total PFAA concentrations (pg L^{-1}) in snow/ice, meltwater, and neighboring seawater in global glacial regions.

Glacial region	Type	Year	Number(n)	PFBA	PFPeA	PFHxA	PFHpA	PFOA	PFNA	PFDA	PFUdA	PFDoA	PFTrDA	PFBS	PFHxS	PFOS	Σ_{13}PFAAs	Ref.
Western Canada and USA (WCUG)			**25**															
Near Alaskan glaciers	Seawater	2012	7	n.r.	<LOD	<LOD	4.29	32.3	11.0	2.14	<LOD	1.14	<LOD	1.57	2.29	15.6	70.3	[13]
Melville ice cap	Snow/ice	2005-2006	2	n.r.	n.r.	n.r.	n.r.	27.5	8.70	3.05	1.40	n.r.	n.r.	n.r.	n.r.	3.50	44.1	[14]
Near Alaskan glaciers	Seawater	2010-2014	4	1.40	27.8	72.9	12.6	22.0	<LOD	32.6	15.0	3.50	n.r.	0.50	116	132	436	[15]
Cedar Lake, Western Canada	Glacial runoff	2004	12	n.r.	n.r.	n.r.	n.r.	761	598	136	77.5	n.r.	n.r.	n.r.	n.r.	66.8	1639	[16]
Arctic Canada (ACG)			**179**															
Agassiz, Devon & Meighen ice cap	Snow/ice	2005-2006	4	n.r.	n.r.	n.r.	n.r.	24.6	10.2	3.23	2.25	n.r.	n.r.	n.r.	n.r.	2.33	42.6	[14]
Devon ice cap	Snow/ice	2015	37	<LOD	40.5	81.7	166	164	275	40.8	53.3	0.34	<LOD	0.30	0.49	39.8	862	[17]
Ice caps in the Garfield Range, Lake Hazen basin	Snow/ice	2008	3	n.r.	n.r.	n.r.	207	218	220	29.3	21.0	n.r.	n.r.	8.67	6.00	37.0	747	[18]
Ellesmere Island	Glacial runoff	2012-2014	25	1993	701	850	1060	1176	450	73.2	24.0	6.25	5.56	93.7	17.9	60.6	6512	[19]
Ellesmere Island	Snow/ice	2013	27	5467	387	513	1017	1703	1363	343	186	69.3	14.0	6.33	<LOD	133	11202	[20]
Devon ice cap	Snow/ice	2015-2017	83	370	n.r.	n.r.	n.r.	n.r.	n.r.	n.r.	n.r.	n.r.	n.r.	n.r.	n.r.	n.r.	370	[21]
Greenland ice sheet (GIS)			**10**															
Central Arctic	Seawater	2018	10	n.r.	<LOD	62.7	33.5	51.1	38.2	1.96	4.87	<LOD	<LOD	40.0	<LOD	37.4	270	[22]
Arctic Europe (AEG)			**245**															

Glacial region	Type	Year	Number(n)	PFBA	PFPeA	PFHxA	PFHpA	PFOA	PFNA	PFDA	PFUdA	PFDoA	PFTrDA	PFBS	PFHxS	PFOS	Σ_{13}PFAAs	Ref.
North Barents Sea (PS80/364, PS80/275, PS80/227, PS80/254)	Seawater	2012	3	n.r.	<LOD	4.00	11.0	16.7	12.3	<LOD	<LOD	<LOD	<LOD	8.67	5.00	22.3	80.0	[13]
Ice station (PS80/224, PS80/255)	Glacial runoff	2012	2	n.r.	<LOD	15.5	34.0	59.5	95.5	7.00	6.50	<LOD	<LOD	<LOD	<LOD	38.0	256	[13]
Ice station (PS80/360)	Snow/ice	2012	2	n.r.	<LOD	35.0	19.5	81.5	47.0	41.0	33.0	<LOD	<LOD	<LOD	<LOD	38.5	296	[13]
Ny-Ålesund	Glacial runoff	2014-2016	27	1970	<LOD	16.7	89.2	207	61.5	59.9	<LOD	17.9	<LOD	<LOD	119.6	248	2790	[23]
Ny-Ålesund	Seawater	2014-2016	4	530	710	1420	242.5	155	7.50	<LOD	<LOD	<LOD	<LOD	43.8	160	180	3449	[23]
Northern Swedish glacier	Glacial runoff	2013	44	1471	n.r.	448	428	905	766	431	198	90.3	n.r.	2150	1839	1050	9708	[24]
Northern Barents Sea	Seawater	-	5	126	39.2	83.2	336	600	172	444	86.8	105	16.8	<LOD	<LOD	31.2	2040	[25]
Nansen Basin	Glacial runoff	-	6	836	59.5	58.0	120	42.0	45.5	4.50	6.00	10.5	<LOD	<LOD	<LOD	<LOD	1185	[25]
	Snow/ice	-	40	1571	38.6	78.6	90.9	130	46.4	68.7	22.8	19.3	2.60	1070	<LOD	<LOD	3151	[25]
Transect from European continent to the Arctic and Fram Strait	Seawater	2018	30	n.r.	<LOD	56.7	38.7	66.1	37.6	9.72	9.23	2.80	<LOD	38.4	12.4	64.7	336	[22]
Isfjorden	Seawater	2006	3	57.2	352	55.7	14.6	74.4	38.6	<LOD	<LOD	<LOD	<LOD	<LOD	27.5	109	729	[26]

Glacial region	Type	Year	Number(n)	PFBA	PFPeA	PFHxA	PFHpA	PFOA	PFNA	PFDA	PFUdA	PFDoA	PFTrDA	PFBS	PFHxS	PFOS	Σ_{13}PFAAs	Ref.
Svalbard	Glacial runoff	2006	10	809	964	197	136	226	93.0	14.6	9.07	6.87	<LOD	<LOD	95.3	187	2738	[26]
Longyearbreen glacier	Snow/ice	2006	35	86.7	25.2	30.3	19.6	85.7	51.5	18.4	6.38	4.63	<LOD	<LOD	2.63	27.2	358	[26]
Kongsfjorden	Seawater	2016-2017	10	775	233	<LOD	52.9	<LOD	12.5	<LOD	<LOD	<LOD	<LOD	80.0	<LOD	<LOD	1153	[27]
Umeå N. Sweden	Snow/ice	2009	24	335	165	46.9	2.10	66.5	26.9	16.9	12.7	5.00	<LOD	98.7	25.1	20.50	821	[28]
North Asia (NAG)			**14**															
Arctic Ocean over the Nansen and	Seawater	2012	1	n.r.	<LOD	24.0	<LOD	30.0	39.0	<LOD	17.0	<LOD	<LOD	12.0	<LOD	18.0	140	[13]
Amundsen basins, close to Russia	Snow/ice	2012	1	n.r.	<LOD	109	49.0	294	253	142	92.0	88.0	<LOD	<LOD	18.0	343	1388	[13]
Chukchi Sea	Seawater	2010	12	175	24.2	7.58	36.6	178	86.8	89.3	38.1	12.0	84.2	168	<LOD	17.3	918	[29]
Central Europe (CEG)			**2**															
Colle Gnifetti	Snow/ice	2008	**1**	690	<LOD	60.0	40.0	300	<LOD	<LOD	<LOD	<LOD	<LOD	<LOD	<LOD	<LOD	1090	[30]
Alto dell'Ortles glacier	Snow/ice	2007	**1**	1410	60.0	110	160	380	220	120	<LOD	<LOD	<LOD	<LOD	<LOD	<LOD	2460	[31]
South and Central Asia (SCAG)			**194**															
Khumbu glacier	Snow/ice	2019	6	n.r.	n.r.	1352	<LOD	1752	n.r.	n.r.	n.r.	n.r.	n.r.	n.r.	n.r.	6260	9363	[32]
Khumbu glacier	Glacial runoff	2019	3	n.r.	n.r.	340	<LOD	1323	n.r.	n.r.	n.r.	n.r.	n.r.	n.r.	n.r.	413	2077	[32]
Altai	Snow/ice	2015	1	633	24.5	34.5	29.9	123	100	200	34.5	10.3	23.4	23.2	3.40	335	1576	[33]
Urumqi No. 1 glacier	Snow/ice	2016	1	588	38.6	38.4	34.2	325	98.3	453	22.5	12.3	3.40	15.5	6.80	698	2335	[33]
Kaerlike glacier	Snow/ice	2016	1	437	73.4	11.3	22.4	231	76.5	87.8	34.8	7.20	5.60	28.9	3.50	285	1305	[33]
Muztag glacier	Snow/ice	2016	1	454	103.6	29.9	89.3	234	75.3	69.2	17.9	4.50	1.50	25.2	2.90	233	1341	[33]
Laohugou No. 12 glacier	Snow/ice	2015	1	783	38.7	33.7	49.5	72.8	76.9	135	17.8	3.40	1.80	39.5	5.70	995	2252	[33]

Glacial region	Type	Year	Number(n)	PFBA	PFPeA	PFHxA	PFHpA	PFOA	PFNA	PFDA	PFUdA	PFDoA	PFTrDA	PFBS	PFHxS	PFOS	Σ_{13}PFAAs	Ref.
Germu	Snow/ice	2015	1	378	55.6	14.4	98.3	123	101	111	34.5	5.20	3.50	38.2	2.60	849	1815	[33]
Ali Glacier	Snow/ice	2016	1	95.5	34.9	56.2	87.3	137	129	231	29.5	4.70	3.50	5.50	3.60	295	1113	[33]
Shuanghu glacier	Snow/ice	2016	1	385	86.8	64.7	64.3	47.8	67.9	34.4	76.2	8.60	9.20	9.70	1.80	386	1242	[33]
Guoqu	Snow/ice	2015	1	283	79.5	12.3	67.4	103	98.7	64.5	33.4	3.70	6.50	6.90	2.80	110	872	[33]
Pulan glacier	Snow/ice	2016	1	222	99.3	34.2	83.4	634	230	233	15.3	8.50	4.20	25.4	3.60	278	1872	[33]
Nianqin glacier	Snow/ice	2015	1	184	65.8	44.3	65.3	589	384	221	26.4	8.30	3.50	13.7	4.70	273	1883	[33]
Jimayangzong glacier	Snow/ice	2016	1	395	78.6	27.5	27.8	765	188	342	26.7	6.90	2.50	43.5	3.60	110	2017	[33]
Ranwu	Snow/ice	2017	1	654	46.9	23.8	45.3	670	453	295	38.5	9.40	3.70	66.8	5.90	390	2702	[33]
East Rongbuk glacier	Snow/ice	2016	1	375	77.8	33.6	27.4	399	346	565	25.1	6.40	3.50	12.6	7.60	193	2071	[33]
Yulong, Baishui No. 1 glacier	Snow/ice	2017	1	745	96.4	43.2	105	1089	654	340	24.5	5.50	4.70	67.8	9.20	783	3968	[33]
Mt Zuoqiupu glacier	Snow/ice	2007	1	36.7	39.4	<LOD	<LOD	183	25.7	<LOD	<LOD	<LOD	<LOD	<LOD	<LOD	<LOD	285	[6]
Mt Muztagata glacie	Snow/ice	1999	1	<LOD	142	100	<LOD	243	42.2	50.0	9.97	33.1	<LOD	<LOD	<LOD	308	928	[6]
Zhadang glacier	Snow/ice	2010	8	1905	241	118	516	148	74.1	24.5	9.66	7.41	<LOD	<LOD	<LOD	44.1	3087	[6]
Zhadang glacier	Snow/ice	2017	12	541	155	61.4	78.6	1490	96.0	59.0	45.2	11.3	3.73	140	10.2	62.9	1412	[3]
Zhadang glacier	Glacial runoff	2017	89	641	170	46.7	79.4	63.7	33.6	18.1	4.97	9.63	2.79	59.9	14.6	69.4	1215	[3]
Korchung Gangri glacier	Glacial runoff	2019	8	714	59.2	55.2	63.7	46.4	40.8	8.70	9.81	1.54	0.32	52.3	10.9	33.6	1096	This study
Zhadang glacier	Glacial runoff	2019	8	599	110	43.5	45.3	123	59.2	39.6	14.0	9.69	1.19	34.1	8.42	55.6	1143	This study
Galongla glacier	Glacial runoff	2019	7	206	43.0	28.9	19.2	30.3	11.6	8.67	4.76	0.12	<LOD	45.0	3.38	109	510	This study

Glacial region	Type	Year	Number(n)	PFBA	PFPeA	PFHxA	PFHpA	PFOA	PFNA	PFDA	PFUdA	PFDoA	PFTrDA	PFBS	PFHxS	PFOS	Σ_{13}PFAAs	Ref.
Parlung No. 4 glacier	Glacial runoff	2019	8	272	33.4	15.5	26.6	24.8	13.0	2.92	2.70	0.38	<LOD	82.9	3.96	16.2	494	This study
Qiangyong glacier	Glacial runoff	2019	8	379	72.9	51.5	61.9	49.6	23.3	5.26	3.35	<LOD	<LOD	43.2	7.59	20.5	718	This study
Rijie Cojia glacier	Glacial runoff	2019	8	697	89.6	41.8	29.9	44.0	12.2	12.5	5.69	1.66	0.15	90.1	7.02	14.4	1046	This study
Rongbuk glacier	Glacial runoff	2020	12	4606	137	113	89.5	91.1	31.0	6.28	2.59	1.73	1.05	252	35.8	64.2	5431	This study
Antarctic and Subantarctic ice sheet (AIS)			**70**															
Livingston Island	Snow/ice	2014-2015	16	154	7.91	42.4	73.8	239	62.4	96.8	29.0	21.6	3.60	n.r.	1.79	62.9	795	[34]
Livingston Island	Glacial runoff	2014-2015	3	420	<LOD	7.07	27.3	38.7	22.0	6.63	5.70	1.73	0.61	n.r.	2.79	11.9	544	[34]
King George Island	Seawater	2011	10	22.2	58.3	199	2.81	3414	<LOD	0.00	13.4	4.07	90.2	3.16	<LOD	<LOD	3806	[35]
King George Island	Snow/ice	2011	4	522	73.9	309	<LOD	197	48.3	33.3	79.4	47.3	190	4.15	<LOD	<LOD	1504	[35]
King George Island	Glacial runoff	2011	5	2096	49.8	111	76.0	454	21.6	<LOD	2.32	<LOD	874	15.2	<LOD	<LOD	3699	[35]
Dome C	Snow/ice	2016	11	<LOD	175	221	183	359	73.1	30.5	7.94	3.92	2.14	24.0	5.95	46.2	1131	[36]
Larsemann Hills	Glacial runoff	2015-2016	21	<LOD	23.5	5.29	5.78	56.6	1.36	20.8	3.16	0.92	3.21	9.76	12.5	3.82	147	[37]

Note: Number (n) refers to the reported sample count. Concentrations of individual PFAAs in this table represent average values when n>1. “n.r.” indicates that the compound was not reported, while “<LOD” represents concentrations below the limit of detection (LOD).

Table S3. The average concentrations and standard deviation (SD) of individual and total PFAAs (pg L^{-1}) in the eight glacial regions calculated based on the global dataset.

Glacial region	Type	PFBA	PFPeA	PFHxA	PFHpA	PFOA	PFNA	PFDA	PFUdA	PFDoA	PFTrDA	PFBS	PFHxS	PFOS	Σ_{13}PFAAs
WCUG	Average	0.77	13.4	28.0	8.04	275	205	51.2	32.6	4.95	5.37	2.30	44.8	43.2	715
	SD	0.43	11.1	33.7	4.14	418	303	68.6	55.6	2.51	2.90	2.01	54.1	45.7	1002
ACG	Average	2112	276	378	570	518	390	82.0	53.6	22.2	6.77	24.1	6.46	46.0	4486
	SD	2562	477	518	718	836	563	153	87.5	39.7	9.70	50.2	11.9	67.0	6093
GIS	Average	-	12.4	62.7	33.5	51.1	38.2	1.96	4.87	1.81	2.55	40.0	10.0	37.4	297
	SD	-	6.83	0.00	0.00	0.00	0.00	0.00	0.00	0.98	1.36	0.00	5.33	0.00	14.5
AEG	Average	1219	112	109	71.7	139	61.9	44.7	35.9	15.1	2.87	118	97.0	135	2162
	SD	1903	217	309	107	236	164	132	55.8	30.9	3.33	667	594	290	4710
NAG	Average	231	25.8	26.4	37.5	177	94.7	87.9	43.2	20.2	80.6	147	32.2	46.5	1050
	SD	300	19.2	26.9	33.3	169	62.6	64.3	35.7	27.8	144	374	20.0	84.2	1362
ECG	Average	1047	38.2	85.2	100	340	141	78.1	54.9	43.6	44.2	-	-	87.5	2060
	SD	360	22.2	25.0	60.0	40.0	82.7	44.0	31.5	22.9	22.7	-	-	49.5	760
SCAG	Average	1203	145	88.8	87.5	152	69.0	43.4	22.8	8.31	3.22	117	14.4	179	2133
	SD	1817	89.7	224	93.0	341	79.2	71.6	37.2	6.30	3.40	152	12.9	1338	4264
AIS	Average	809	102	150	107	538	50.1	34.3	13.3	7.08	17.4	16.5	6.88	34.3	1886
	SD	915	104	127	93.9	1680	45.6	58.4	30.8	23.1	57.7	9.92	5.44	68.4	3219

Note: -, data not available. WCUG, Western Canada and USA; ACG, Arctic Canada; GIS, Greenland ice sheet; AEG, Arctic Europe; NAG, North Asia; CEG, Central Europe; SCAG, South and Central Asia; AIS, Antarctic and Subantarctic ice sheet. PFBA, perfluorobutanoic acid; PFPeA, perfluoropentanoic acid; PFHxA, perfluorohexanoic acid; PFHpA, perfluoroheptanoic acid; PFOA, perfluoro-octanoic acid; PFNA, perfluorononanoic acid; PFDA, perfluorodecanoic acid; PFUdA, perfluoroundecanoic acid; PFDoA, perfluorododecanoic acid; PFTrDA, perfluorotridecanoic acid; PFBS, perfluorobutane sulfonic acid; PFHxS, perfluorohexane sulfonic acid; and PFOS, perfluoro-octane sulfonic acid.

Table S4. The dataset of measured logK_d of individual PFAAs with the associated water temperature (T_w, °C), particulate organic carbon (POC, %)

Region type	Data count	logK_d of PFCAs (acid type: carboxylic acids)										logK_d of PFSAs (acid type: sulfonic acids)			T_w	POC	Ref.
		PFBA	PFPeA	PFHxA	PFHpA	PFOA	PFNA	PFDA	PFUdA	PFDoA	PFTrDA	PFBS	PFHxS	PFOS			
Glacial regions (n=191)	13	1.82	2.91	3.06	2.68	3.41	2.74	3.38	4.21	4.54	5.43	2.92	4.02	3.58	0.20	0.52	This study
	13	1.94	2.65	2.42	2.06	3.01	2.71	3.28	3.96	3.72	4.69	2.85	3.58	2.35	1.70	0.31	
	12	1.78	2.08	2.28	2.00	2.73	2.36	2.96	3.81	3.61	-	1.83	2.95	2.40	2.50	0.24	
	9	-	2.99	3.12	2.95	3.55	3.28	4.13	4.37	-	-	2.80	-	3.76	0.20	1.04	
	7	1.97	2.23	-	-	2.61	2.18	2.90	3.41	-	-	-	-	2.83	3.90	0.86	
	8	-	1.73	2.00	1.47	2.23	2.04	2.78	3.31	-	-	-	-	2.38	3.20	0.61	
	13	2.05	2.87	3.04	2.98	3.36	3.25	3.31	3.85	3.41	3.73	3.30	3.19	3.39	0.20	0.33	
	13	1.75	2.30	2.37	2.61	3.05	2.90	3.10	3.62	2.94	4.07	3.74	3.20	2.94	2.60	0.27	
	13	1.20	2.40	2.48	2.12	2.85	2.90	2.62	3.20	3.20	4.26	2.83	3.12	3.26	1.80	0.33	
	13	2.79	2.86	3.11	2.94	3.32	3.18	3.09	3.62	3.95	3.64	4.08	3.04	2.14	9.20	4.00	
	13	2.49	2.79	3.22	2.25	3.10	3.21	3.19	3.68	3.15	3.67	4.65	3.65	3.20	8.40	2.17	
	13	2.67	2.12	3.06	2.89	2.78	2.54	3.10	2.97	3.45	3.55	2.41	3.79	2.85	0.30	1.56	
	10	-	1.60	1.95	2.13	2.05	2.90	2.52	2.37	2.47	-	-	3.17	2.56	11.70	2.47	[38]
	7	-	1.37	2.13	2.13	2.60	-	2.51	-	-	-	-	2.73	2.49	11.70	2.47	
	7	-	1.14	-	-	1.58	2.79		2.90	2.67	-	-	3.20	3.03	11.70	2.47	
	7	-	2.43	1.77	1.65	2.03	3.00	2.69	-	-	-	-	-	3.03	11.70	2.47	
	8	-	1.06	-	1.82	2.52	3.33	2.73	-	3.03	-	-	2.73	2.87	12.30	2.49	
	2	-	1.65	-	-	-	-	-	-	-	-	-	-	2.60	12.30	2.49	
	3	-	-	-	2.25	2.13	-	-	-	-	-	-	-	3.27	12.30	2.49	
	1	-	-	-	-	-	-	-	3.09	-	-	-	-	-	14.81	0.30	[39]
	3	-	1.06	-	-	-	-	-	-	-	-	-	2.15	2.61	14.33	0.91	

	1	-	-	-	-	-	-	-	-	-	-	2.17	-	-	15.81	1.03	
	1	-	-	-	2.36	-	-	-	-	-	-	-	-	-	13.67	1.53	
	1	-	-	-	-	0.95	-	-	-	-	-	-	-	-	17.48	2.50	
	5	2.00	2.30	-	2.10	-	-	-	-	-	2.40	1.80	-	-	1.18	2.00	
	2	-	-	2.20	-	2.70	-	-	-	-	-	-	-	-	1.18	1.59	[40]
	5	2.00	2.20	-	2.20	2.20	-	-	-	-	-	1.80	-	-	3.55	1.59	
	1	-	-	2.20	-	-	-	-	-	-	-	-	-	-	3.55	2.00	
Inland watersheds (n=158)	4	-	-	-	-	0.45	2.13	2.96	-	-	-	-	-	2.36	15.00	12.32	
	4	-	-	-	-	0.30	2.19	3.15	-	-	-	-	-	2.22	15.00	11.54	
	4	-	-	-	-	0.47	2.10	2.79	-	-	-	-	-	2.20	15.00	11.09	
	4	-	-	-	-	0.57	2.12	2.69	-	-	-	-	-	2.21	15.00	10.23	
	4	-	-	-	-	0.49	1.94	2.72	-	-	-	-	-	2.45	15.00	10.19	
	4	-	-	-	-	0.63	2.06	2.45	-	-	-	-	-	2.66	15.00	9.78	
	4	-	-	-	-	0.77	1.76	2.48	-	-	-	-	-	2.68	15.00	12.03	
	4	-	-	-	-	0.72	1.78	2.46	-	-	-	-	-	2.62	15.00	12.32	
	4	-	-	-	-	0.56	1.62	2.34	-	-	-	-	-	2.68	15.00	13.24	
	4	-	-	-	-	0.70	1.94	2.74	-	-	-	-	-	2.67	15.00	12.79	[41]
	4	-	-	-	-	0.56	1.55	2.41	-	-	-	-	-	2.79	15.00	14.25	
	4	-	-	-	-	0.70	1.76	2.23	-	-	-	-	-	2.77	15.00	13.24	
	4	-	-	-	-	0.74	1.84	2.39	-	-	-	-	-	2.80	15.00	11.35	
	4	-	-	-	-	0.40	1.81	2.29	-	-	-	-	-	2.56	15.00	8.23	
	4	-	-	-	-	0.54	1.63	2.40	-	-	-	-	-	2.50	15.00	9.42	
	4	-	-	-	-	0.75	1.72	2.16	-	-	-	-	-	2.26	15.00	10.21	
	4	-	-	-	-	0.58	1.44	2.08	-	-	-	-	-	2.42	15.00	9.78	
	4	-	-	-	-	0.87	1.80	2.23	-	-	-	-	-	2.51	15.00	8.94	
	4	-	-	-	-	0.45	1.61	2.30	-	-	-	-	-	2.62	15.00	7.32	

	4	-	-	-	-	0.48	1.86	2.22	-	-	-	-	-	2.54	15.00	6.23	
	5	1.40	-	0.90	-	-	-	-	-	-	-	0.80	1.10	2.19	8.00	0.93	
	5	1.20	-	0.80	-	-	-	-	-	-	-	0.60	1.00	2.10	8.00	0.86	
	5	2.59	2.52	-	1.84	1.02	2.47	-	-	-	-	-	-	-	15.00	1.17	
	7	-	2.26	2.03	2.19	1.55	-	1.53	-	-	-	-	2.55	1.70	12.00	0.90	
	7	1.63	1.74	-	1.96	0.96	2.28	2.47	-	-	-	-	-	2.05	15.00	0.58	[42]
	5	2.48	2.33	-	1.80	1.00	-	2.18	-	-	-	-	-	-	13.00	1.19	
	6	2.37	1.06	-	2.01	1.07	2.22	2.39	-	-	-	-	-	-	12.00	0.80	
	7	1.92	2.05	-	1.93	1.35	-	2.97	3.37	-	-	-	2.74	-	15.00	1.06	
	4	1.67	1.95	-	1.47	0.84	-	-	-	-	-	-	-	-	12.00	0.85	
	7	2.18	1.90	-	1.78	1.18	-	2.57	-	3.02	-	-	-	2.21	15.00	1.33	
	7	-	-	2.18	1.43	1.91	2.47	-	-	2.49	-	-	2.47	2.73	18.89	0.87	[43]
Coastal areas (n=422)	3	-	-	-0.01	-	0.27	-	-	-	-	-	-	-	1.16	15.00	1.70	[44]
	3	-	-	-0.06	-	0.15	-	-	-	-	-	-	-	1.03	15.00	0.50	
	3	-	-	0.36	-	0.64	-	-	-	-	-	-	-	1.39	15.00	2.70	
	3	-	-	0.03	-	0.26	-	-	-	-	-	-	-	0.99	15.00	1.20	
	3	-	-	0.76	-	0.82	-	-	-	-	-	-	-	1.55	15.00	5.10	
	3	-	-	0.26	-	0.35	-	-	-	-	-	-	-	1.24	15.00	1.10	
	3	-	-	-0.36	-	0.05	-	-	-	-	-	-	-	0.66	15.00	0.30	
	3	-	-	0.50	-	0.42	-	-	-	-	-	-	-	1.48	15.00	3.60	
	3	-	-	-0.14	-	0.11	-	-	-	-	-	-	-	0.98	15.00	0.70	
	3	-	-	0.38	-	0.43	-	-	-	-	-	-	-	1.26	15.00	4.90	
	3	-	-	0.54	-	0.74	-	-	-	-	-	-	-	1.54	15.00	2.90	
	3	-	-	0.54	-	0.79	-	-	-	-	-	-	-	1.57	15.00	5.70	
	3	-	-	-0.46	-	-0.03	-	-	-	-	-	-	-	0.58	15.00	0.10	
	3	-	-	0.89	-	1.17	-	-	-	-	-	-	-	2.01	15.00	11.20	
	3	-	-	0.62	-	0.64	-	-	-	-	-	-	-	1.65	15.00	5.90	

3	-	-	0.45	-	0.52	-	-	-	-	-	-	-	1.55	15.00	3.30	
3	-	-	0.91	-	1.09	-	-	-	-	-	-	-	1.94	15.00	10.00	
3	-	-	0.79	-	1.05	-	-	-	-	-	-	-	1.85	15.00	10.10	
3	-	-	0.79	-	0.99	-	-	-	-	-	-	-	1.71	15.00	5.60	
11	1.28	1.69	0.92	-	2.96	2.44	2.54	3.02	2.27	-	1.75	1.83	2.47	9.58	0.77	
11	1.16	1.75	0.95	1.87	2.93	2.49	2.69	3.18	-	-	2.50	1.73	2.30	9.24	1.05	
12	1.30	1.55	1.11	1.95	2.75	2.35	2.60	3.07	1.70	-	1.94	1.46	2.52	10.42	3.53	
12	1.37	1.47	1.08	2.20	2.83	2.66	3.20	3.48	2.51	-	1.94	1.32	2.76	11.29	4.15	
11	-	1.65	1.30	2.56	2.91	2.62	2.79	3.38	2.47	-	2.02	1.79	2.77	11.16	4.98	
12	1.08	1.76	1.34	2.50	2.96	2.63	2.33	3.24	2.14	-	2.07	1.73	2.80	11.33	4.23	
10	1.02	-	1.25	-	3.02	2.32	2.85	3.01	2.03	-	1.92	1.63	2.78	10.89	4.86	
12	1.02	1.95	1.17	2.44	3.04	2.51	2.64	3.26	2.16	-	2.06	1.68	2.76	11.19	5.23	
12	1.18	1.70	1.15	2.35	3.07	2.69	2.41	3.37	2.16	-	2.06	1.46	2.70	10.45	4.35	
11	0.88	1.35	1.22	1.91	2.93	2.85	3.04	3.29	-	-	2.36	1.63	2.54	10.11	4.20	
8	1.11	1.79	1.23	2.32	-	-	2.73	-	2.07	-		1.75	2.18	9.25	3.33	
9	1.46	1.77	1.24	2.06	-	-	2.63	-	1.89	-	1.84	1.91	2.41	8.62	3.41	[45]
9	1.02	-	1.45	1.90	-	2.23	2.88	-	2.01	-	2.12	1.95	2.40	8.47	2.55	
8	1.35	1.16	1.64	-	-	2.85		-	2.22	-	2.15	1.83	2.00	8.03	2.00	
9	0.61	0.51	1.00	-	-	1.63	2.52	-	1.88	-	1.42	1.10	1.70	8.03	4.31	
7	-	-	-	2.25	-	2.82	2.88	-	1.75	-	1.97	2.03	2.56	8.24	1.67	
10	1.59	-	1.47	2.27	2.56	2.75	2.92	-	2.26	-	2.04	1.83	1.36	8.89	2.74	
10	1.23	2.08	1.35	2.41	2.86	-	2.83	-	2.61	-	2.63	1.87	2.75	10.36	2.14	
10	1.51	-	1.42	2.70	-	2.76	3.10	3.42	2.16	-	2.09	1.81	2.55	10.90	3.60	
10	1.16	1.78	1.25	2.36	2.71	-	2.64	-	2.49	-	2.08	1.57	2.73	10.83	4.29	
9	1.27	1.51	1.41	-		2.50	3.01	-	2.31	-	2.03	1.48	2.85	10.40	4.65	
9	1.34	-	1.37	-	2.98	2.46	2.98	-	2.04	-	1.97	1.75	2.58	10.17	3.84	
11	1.22	1.77	1.42	2.40	-	2.59	3.12	3.38	1.93	-	2.31	1.81	2.59	10.24	4.02	

9	1.23	-	1.09	2.24	2.55	-	2.64	-	1.75	-	1.75	1.62	2.41	9.40	4.14
9	1.14	-	1.30	-	2.68	2.31	2.98	-	1.76	-	2.07	1.61	2.61	8.03	3.95
11	1.41	-	1.81	2.41	2.82	2.54	3.02	3.31	1.70	-	2.32	1.75	1.63	8.85	3.51
10	-	1.78	1.43	2.22	-	2.76	2.41	3.74	1.84	-	1.95	1.93	2.49	9.75	2.29
11	-	1.25	1.75	2.10	3.05	2.65	2.73	3.52	1.47	-	1.83	2.01	2.84	8.45	1.29
10	0.99	0.91	1.93	2.22	-	2.35	2.89	-	1.51	-	1.72	1.84	2.70	7.95	1.74
10	1.42	1.44	1.01	-	2.74	2.20	2.79	-	2.03	-	2.09	1.40	2.38	10.15	4.97
10	1.47	1.41	0.89	-	2.79	2.46	2.59	-	1.73	-	2.08	1.75	2.44	11.32	6.48
10	1.51	1.69	1.26	-	2.83	2.53	2.54	-	1.97	-	2.17	1.59	2.31	11.16	4.90
10	1.11	1.25	1.06	2.25	2.84	-	2.58	-	1.88	-	1.74	1.55	2.41	11.02	6.17
11	1.49	1.00	1.37	2.23	2.50	2.58	2.93	-	1.83	-	1.97	1.72	2.09	10.64	5.13
11	1.60	1.52	1.20	1.71	2.72	2.47	2.91	-	1.90	-	2.14	1.84	2.06	10.69	2.32
10	1.09	1.26	1.55	2.11	-	2.60	2.81	-	2.02	-	2.21	1.73	2.32	9.19	1.54

Note: -, data not available. This dataset, which includes logK_d, T_w, POC values from glacial and non-glacial regions (inland watershed and coastal areas), was used to train the machine learning models discussed in the Methods section in the main manuscript and Note S1. The log$K_{ow\text{-}ionic}$ for each PFAAs used in the dataset is a constant which is available in Table S1.

Table S5. The average concentrations and standard deviation (SD) of individual and total PFAAs (pg g^{-1} dry weight) in suspended particles in the eight global glacial regions using XGBoost-ML established in this study.

Glacial region	Type	PFBA	PFPeA	PFHxA	PFHpA	PFOA	PFNA	PFDA	PFUdA	PFDoA	PFTrDA	PFBS	PFHxS	PFOS	Σ_{13}PFAAs
WCUG	Average	0.01	0.4	1.11	0.17	22.5	10.8	8.80	24.9	4.97	26.8	0.46	15.6	5.75	122
	SD	0.04	1.22	3.97	0.62	124	69.6	42.2	147	17.4	97.2	1.37	62.4	25.6	593
ACG	Average	7.72	4.49	8.38	7.99	32.8	14.2	4.37	10.1	2.57	4.3	2.8	0.97	3.87	104
	SD	11.9	9.79	14.3	12.8	64.9	25.4	9.93	20.6	5.54	7.65	7.09	2.21	7.07	199
GIS	Average	-	3.35	22.2	6.46	37.8	16.9	3.02	31	12.1	80.4	62.3	30.7	51.2	357
	SD	-	21.4	103	35.0	201	71.7	17.9	151	65.8	392	397	298	320	2075
AEG	Average	6.8	3.36	4.01	1.65	14.5	4.57	3.85	11	3.26	3.36	17.1	20.4	18.3	112
	SD	43.2	38.1	40.9	12.5	109	56.8	32.9	65.3	32.9	19.9	190	283	151	1075
NAG	Average	5.53	1.15	2.18	1.49	24.5	7.75	20	28.1	10.1	141	35.3	13.1	8.98	299
	SD	31.1	6.06	17.1	7.63	146	32.8	123	138	70.4	1086	429	58.7	61.3	2207
CEG	Average	15.0	2.31	7.46	5.39	82.1	20.3	15.9	40.6	19.8	113	-	-	30.3	352
	SD	11.6	2.28	5.52	5.23	54.3	19.2	15.5	36.8	18.1	102	-	-	27.2	298
SCAG	Average	34.6	11.4	9.59	5.35	36.7	9.4	18.9	41.7	15.5	28.4	48.5	12.2	77.9	350
	SD	67.7	12.1	33.0	8.19	106	14.5	39.9	92.2	18.7	44.6	83.6	16.6	751	1288
AIS	Average	3.42	1.38	2.27	1.00	26.8	1.71	2.52	3.72	1.25	15.7	1.59	0.78	1.28	63.4
	SD	10.6	4.15	7.30	2.91	187	4.95	9.48	18.9	7.53	110	3.87	2.22	5.82	375

Note: -, data not available. WCUG, Western Canada and USA; ACG, Arctic Canada; GIS, Greenland ice sheet; AEG, Arctic Europe; NAG, North Asia; CEG, Central Europe; SCAG, South and Central Asia; AIS, Antarctic and Subantarctic ice sheet. PFBA, perfluorobutanoic acid; PFPeA, perfluoropentanoic acid; PFHxA, perfluorohexanoic acid; PFHpA, perfluoroheptanoic acid; PFOA, perfluoro-octanoic acid; PFNA, perfluorononanoic acid; PFDA, perfluorodecanoic acid; PFUdA, perfluoroundecanoic acid; PFDoA, perfluorododecanoic acid; PFTrDA, perfluorotridecanoic acid; PFBS, perfluorobutane sulfonic acid; PFHxS, perfluorohexane sulfonic acid; and PFOS, perfluoro-octane sulfonic acid.

Table S6. Release fluxes (kg year^{-1}) of individual and total perfluoroalkyl acids (PFAAs) from the eight global glacial regions via the water-soluble phase and suspended particles.

Glacial regions	Type	Data	PFBA (C4)	PFPeA (C5)	PFHxA (C6)	PFHpA (C7)	PFOA (C8)	PFNA (C9)	PFDA (C10)	PFUdA (C11)	PFDoA (C12)	PFTrDA (C13)	PFBS (C4)	PFHxS (C6)	PFOS (C8)	Short-chain	Long-chain	$\sum_{12}$PFAAs	$\sum_{13}$PFAAs
WCUG	Water	Average	0.14	2.41	4.85	1.39	162	125	30.4	19.8	0.86	0.93	0.40	7.61	24.2	16.4	363	380	380
		SD	0.00	0.09	0.25	0.04	3.87	2.18	0.55	0.56	0.02	0.03	0.02	0.41	0.53	0.80	7.74	8.56	8.56
	Particle	Average	0.00	0.05	0.14	0.02	12.0	6.29	4.98	14.2	0.48	2.59	0.11	2.12	3.11	2.34	43.7	46.2	46.2
		SD	0.00	0.01	0.02	0.00	1.44	0.71	0.49	2.18	0.06	0.35	0.01	0.39	0.34	0.43	5.57	6.01	6.01
AGC	Water	Average	286	42.9	51.7	79.4	106	75.8	15.4	9.94	2.81	0.89	3.46	0.96	9.11	461	219	398	684
		SD	18.4	4.20	3.84	5.63	6.60	4.63	1.16	0.81	0.26	0.07	0.40	0.10	0.61	32.2	14.1	28.3	46.7
	Particle	Average	1.20	0.43	0.89	0.86	4.53	2.24	0.74	1.51	0.20	0.33	0.57	0.12	0.57	3.50	10.1	13.0	14.2
		SD	0.10	0.05	0.08	0.08	0.36	0.18	0.08	0.14	0.03	0.03	0.08	0.02	0.04	0.33	0.86	1.18	1.28
GIS	Water	Average	-	6.44	32.4	17.3	26.4	19.7	1.01	2.52	0.91	1.34	20.7	5.18	19.3	61.4	71.3	153	153
		SD	-	0.50	1.68	0.91	1.42	1.04	0.05	0.13	0.08	0.11	1.08	0.41	1.01	3.51	3.84	8.43	8.43
	Particle	Average	-	1.15	6.96	2.36	14.3	6.38	1.48	13.3	3.11	21.6	61.7	7.90	22.0	18.4	82.1	162	162
		SD	-	0.61	2.44	1.00	7.99	2.29	1.07	8.33	1.49	11.0	130	2.74	12.5	6.79	44.7	181	181
AEG	Water	Average	114	19.6	40.9	24.8	45.7	34.1	20.1	10.6	5.30	0.10	82.9	68.5	53.0	268	169	406	520
		SD	1.75	0.43	1.12	0.68	1.08	1.51	1.26	0.66	0.23	0.00	3.79	3.81	1.75	7.79	6.51	16.3	18.1
	Particle	Average	0.82	0.37	1.54	0.76	3.49	3.53	1.36	1.99	0.66	0.08	9.82	15.4	4.39	18.9	15.5	43.4	44.2
		SD	0.07	0.03	0.24	0.20	0.35	0.59	0.17	0.24	0.07	0.01	1.40	3.54	0.38	4.09	1.81	7.23	7.30
NAG	Water	Average	1.66	0.12	0.43	0.29	1.57	1.14	0.78	0.45	0.34	0.33	0.58	0.18	1.21	2.69	5.83	7.44	9.10
		SD	0.11	0.01	0.02	0.01	0.04	0.04	0.02	0.01	0.02	0.03	0.08	0.01	0.08	0.15	0.24	0.36	0.47
	Particle	Average	0.05	0.01	0.02	0.01	0.16	0.08	0.15	0.25	0.09	0.32	0.24	0.07	0.19	0.16	1.25	1.60	1.65
		SD	0.01	0.00	0.00	0.00	0.03	0.01	0.02	0.04	0.01	0.13	0.16	0.01	0.03	0.03	0.28	0.46	0.47
CEG	Water	Average	9.36	0.33	0.76	0.88	3.02	1.26	0.68	0.49	0.38	0.40	-	-	0.80	11.3	7.03	9.00	18.4
		SD	0.13	0.01	0.01	0.02	0.02	0.03	0.02	0.01	0.01	0.01	-	-	0.02	0.17	0.11	0.15	0.28
	Particle	Average	0.15	0.02	0.06	0.04	0.61	0.16	0.13	0.32	0.13	0.74	-	-	0.24	0.27	2.33	2.45	2.60

Glacial regions	Type	Data	PFBA (C4)	PFPeA (C5)	PFHxA (C6)	PFHpA (C7)	PFOA (C8)	PFNA (C9)	PFDA (C10)	PFUdA (C11)	PFDoA (C12)	PFTrDA (C13)	PFBS (C4)	PFHxS (C6)	PFOS (C8)	Short-chain	Long-chain	$\sum_{12}$PFAAs	$\sum_{13}$PFAAs
SCAG	Water	SD	0.00	0.00	0.00	0.00	0.01	0.01	0.00	0.01	0.00	0.02	-	-	0.01	0.01	0.07	0.08	0.08
		Average	829	54.4	41.7	35.6	67.2	25.1	15.6	7.36	2.52	1.12	56.9	7.54	99.2	968	218	414	1243
	Particle	SD	45.6	0.95	2.17	1.00	3.48	0.90	0.79	0.47	0.09	0.04	1.74	0.30	16.2	50.0	21.9	28.1	73.7
		Average	28.8	3.41	3.70	1.91	12.1	2.96	6.13	11.4	3.01	6.09	31.9	5.58	33.7	43.4	75.3	122	151
		SD	1.70	0.08	0.26	0.07	0.76	0.12	0.40	0.79	0.13	0.26	1.28	0.25	6.51	2.36	8.98	10.9	12.6
AIS	Water	Average	25.2	1.77	5.47	1.29	67.2	1.20	1.74	0.97	0.53	2.39	0.39	0.31	0.97	34.0	75.0	84.2	109
		SD	1.66	0.07	0.26	0.08	6.29	0.09	0.13	0.06	0.05	0.15	0.01	0.02	0.12	2.08	6.88	7.31	8.97
	Particle	Average	0.09	0.03	0.11	0.01	4.07	0.05	0.15	0.34	0.13	3.12	0.02	0.04	0.04	0.27	7.89	8.10	8.19
		SD	0.01	0.00	0.01	0.00	0.62	0.00	0.02	0.04	0.02	0.36	0.00	0.01	0.01	0.03	1.07	1.09	1.10
Total	Water	Average	1265	128	178	161	479	283	85.7	52.1	13.7	7.52	165	90.3	208	1823	1129	1852	3117
		SD	67.7	6.26	9.34	8.36	22.8	10.4	3.98	2.71	0.75	0.44	7.12	5.05	20.3	96.7	61.4	97.5	165
	Particle	Average	31.1	5.46	13.4	5.98	51.2	21.7	15.1	43.3	7.81	34.9	104	31.3	64.2	87.2	238	399	430
		SD	1.90	0.78	3.06	1.36	11.6	3.92	2.25	11.8	1.81	12.2	133	6.96	19.8	14.1	63.3	208	210

Note: WCUG, Western Canada and USA; ACG, Arctic Canada; GIS, Greenland ice sheet; AEG, Arctic Europe; NAG, North Asia; CEG, Central Europe; SCAG, South and Central Asia; AIS, Antarctic and Subantarctic ice sheet; PFBA, perfluorobutanoic acid; PFPeA, perfluoropentanoic acid; PFHxA, perfluorohexanoic acid; PFHpA, perfluoroheptanoic acid; PFOA, perfluoro-octanoic acid; PFNA, perfluorononanoic acid; PFDA, perfluorodecanoic acid; PFUdA, perfluoroundecanoic acid; PFDoA, perfluorododecanoic acid; PFTrDA, perfluorotridecanoic acid; PFBS, perfluorobutane sulfonic acid; PFHxS, perfluorohexane sulfonic acid; and PFOS, perfluoro-octane sulfonic acid. Short-chain PFAAs include C<8 perfluoroalkyl carboxylic acids (PFCAs) and C4 PFBS, whereas long-chain PFAAs comprise C⩾8 PFCAs, C6 PFHxS and C8 PFOS. Σ_{12}PFAAs refers to the sum of 12 PFAA compounds, excluding PFBA.

Table S7. The locations of concern with high PFAA levels in water in the Arctic and Tibetan Plateau

Region	Area	Location	°E	°N	PFAA concentration (pg/L)	Buffer Zone	Ref.
Arctic (>60°N)	Lake Hazen, Ellesmere Island	—	-72.54	80.88	6512	III	[19]
					11202		[20]
	Northern Swedish glacier	Pite älv	21.30	65.38	7410	III	[24]
		Skellefte älv	20.77	64.74	7810	III	
		Ume älv [Gubböle]	19.94	64.09	58340	III	
		Indalsälven	17.38	62.52	26400	III	
		Delångersån	17.09	61.64	59220	III	
		Gavleån	17.14	60.67	11168	III	
		Dalälven	21.29	65.38	5146	II	
		Torne älv	24.16	65.85	2151	I	
		Råne älv	21.97	66.02	3830	I	
		Öre älv	19.66	63.61	2107	I	
		Ljusnan	17.08	61.21	2570	I	
	Ny-Ålesund, Svalbard	W-NA03	11.89	78.92	8400	III	[23]
		W-NA05	11.92	78.92	7300	III	
		W-NA06	11.94	78.92	8900	III	
		W-NA07	11.92	78.92	9600	III	
		W-NA08	11.90	78.92	7100	III	
		W-NA15	11.86	78.92	6900	III	
		W-LI01	13.77	78.05	4110	II	
		W-NA04	11.85	78.93	3400	I	
	Nansen Basin, Svalbard	—	30.25	86.27	3151	I	[25]
	Longyearbyen, Svalbard	—	15.85	78.66	2738	I	[26]
South and Central Asia (SCAG)	Khumbu glacier	—	86.81	27.93	9363	III	[32]
	Rongbuk glacier	—	86.92	27.99	5431	III	This study
	Yulong, Baishui No. 1 glacier	—	100.20	27.11	3968	II	[33]
	Zhadang glacier	—	90.98	30.61	3087	I	[6]
	Ranwu	—	96.79	29.44	2702	I	
	Urumqi No.1 Glacier	—	86.81	43.11	2335	I	[33]
	Laohugou No.12 Glacier	—	96.56	39.43	2252	I	

Jimayangzong Glacier	—	84.15	29.66	2017	I
Nianqin Glacier	—	90.65	30.47	1883	I
Pulan glacier	—	81.18	30.37	1872	I
Germu	—	94.89	36.41	1815	I

Note: Buffer zones I, II, and III are defined based on PFAA concentrations being higher than the regional average (~2000 pg/L) by 1 time, 2 times, and more than 3 times, respectively, representing impact zones of 100 km, 200 km, and 300 km.

Table S8. The locations of concern with high PFAA levels in sediments in the Arctic

Region	Area	Location	°E	°N	PFAA concentration (pg/g)	Buffer Zone	Ref.
Arctic (>60°N)	Svalbard	HF 1	79.83	11.86	12090	III	46
		SF 2	79.72	11.08	2310	II	
		KN11	12.29	78.92	1830	I	
	Arctic Europe	P2002003	5.82	59.30	4400	III	47
		R3105	28.95	80.50	4100	III	
		R1887	22.13	80.17	3460	III	
		R1878	22.15	80.09	3440	III	
		P2002002	6.04	59.23	3000	II	
		R1653	25.53	74.39	2950	II	
		R431	16.75	71.86	2910	II	
		R1661	26.11	74.15	2360	II	
		P2002009	5.77	58.94	2320	II	
		R1331	29.20	71.32	2280	II	
		R422	16.91	72.04	2250	II	
		R2924	26.95	81.41	1920	I	
		R1312	29.91	70.86	1780	I	
		R3004	16.11	80.40	1760	I	
		R2770	27.16	75.12	1740	I	
		R2596	9.34	64.52	1740	I	
		R2183	8.41	64.28	1700	I	
		R1466	34.30	73.21	1690	I	
		R1872	22.25	80.04	1680	I	
		P2102007	21.13	69.99	1670	I	
		R3184	4.70	58.81	1670	I	
		R2438	6.49	65.36	1660	I	
		P2102015	21.33	70.06	1580	I	
		R2242	10.43	66.83	1450	I	
		R2338	9.08	65.72	1360	I	
		P2102008	20.76	69.85	1330	I	
		R223	16.33	69.26	1300	I	
		R2276	10.18	65.68	1290	I	
		P2005008	6.18	62.58	1290	I	
		R2969	22.17	81.50	1240	I	
		R498	25.84	72.10	1190	I	
		P2102019	21.73	70.04	1080	I	
		R2229	8.22	64.71	1060	I	

Region	Area	Location	°E	°N	PFAA concentration (pg/g)	Buffer Zone	Ref.
		P2002007	5.54	59.09	1030	I	
		R1627	26.42	76.02	1020	I	
		R2270	10.48	66.23	1000	I	
	Arctic Canadian basins	Lake B35	-94.95	64.02	1500	I	4
	Chukchi Sea	C11	-167.04	67.67	2670	II	48
		C04	-166.97	71.01	1570	I	
		S23	-152.24	71.93	1450	I	
		S25	-151.50	72.34	1360	I	
		S26	-152.45	72.70	1230	I	
		BB01	-176.52	61.29	1200	I	
		S21	-153.28	71.62	1170	I	
		NB01	-174.92	61.23	1110	I	
		R09	-167.06	71.96	1060	I	
		BB05	-174.67	62.54	1030	I	
		B13	182.52	61.29	1730	I	49
		C24	199.17	71.82	1540	I	

Note: Buffer zones I, II, and III are defined based on PFAA concentrations being higher than the regional average (~1000 pg/g) by 1 time, 2 times, and more than 3 times, respectively, representing impact zones of 100 km, 200 km, and 300 km.

Table S9. Comparison of depositional fluxes (ng m^{-2} $year^{-1}$) of PFAAs calculated by the GEOS-Chem model and firn/ice cores.

Glacial region	Depositional fluxes calculated by the GEOS-Chem model[50]		Depositional fluxes calculated by firn/ice cores			
	Value	Year	Value	Site	Year	Sample type[ref.]
Arctic Canada	120–560	2013–2015	45.3–313	Devon ice cap	2013–2015	Ice core[17]
Central Europe	1600	2013–2015	1091	Colle Gnifetti, Alps	2003–2007	Firn core[30]
			1860	Mt Ortles, Alps	2009	Firn core[31]
South and Central Asia	1550–2100	2013–2015	588	Mt Muztagata	1999	Snow core[6]
			420	Mt Zuoqiupu	2006	
Antarctic and Subantarctic ice sheet	2.1–16	2013–2015	30.7*	Kohnen Research Station, Antarctica	2013	Firn core[51]

Note: * Value excludes perfluorobutanoic acid (PFBA).

Table S10. Basic information about the seven glacial regions on the Tibetan Plateau.

Glacial region	Terminal altitude of glacier(m)	Basin area (km^2)	Area of glacier (km^2)	Annual precipitation (mm)	Annual evaporation (mm)	Glacier type	Influencing climate factors
Rongbuk glacier	~5150	298	203	266	-	Subcontinental	Controlled by the south west Indian monsoon
Zhadang glacier	~5500	58	1.9	415	1650	Subcontinental	Controlled by the Indian monsoon in summer and westerlies in winter
Korchung Gangri glacier	~5500	~34	~2.9	390	2046	Subcontinental	Controlled by the Indian monsoon in summer and westerlies in winter
Qiangyong glacier	~5000	-	7	388	2023	Subcontinental	Controlled by the Indian monsoon in summer and westerlies in winter
Rijie Cojia glacier	~5300	-	-	360	1981	Continental	Influenced by the westerly southern branch and the Indian monsoon
Galongla glacier	3880	-	2.7	1697 (June–September)	-	Temperate	Mainly influenced by the Indian monsoon
Parlung No. 4 glacier	4650	-	11.7	970	-	Temperate	Mainly influenced by the Indian monsoon

Note: -, data not available.

Table S11. Target analytes and internal standards used in this study.

Analyte	Formula	Supplier	Purity (%)	Precursor ion [*m*/*z*]	Product ion [*m*/*z*]	Collision energy (V)
PFBA	C_3F_7COOH	ABCR	99	212.9	**168.7**, 119.0	8, 15
PFPeA	C_4F_9COOH	Alfa Aesar	98	262.8	**218.9**, 70.0	5, 13
PFHxA	$C_5F_{11}COOH$	Fluka	97	312.9	**268.8**, 119.0	5, 15
PFHpA	$C_6F_{13}COOH$	Lancaster Synthesis	98	362.9	**318.9**, 169.0	9, 16
PFOA	$C_7F_{15}COOH$	Lancaster Synthesis	95	412.9	**368.9**, 169.0	8, 19
PFNA	$C_8F_{17}COOH$	Lancaster Synthesis	97	462.9	**418.9**, 219.0	10, 18
PFDA	$C_9F_{19}COOH$	Lancaster Synthesis	97	512.9	**469.0**, 269.0	8, 17
PFUdA	$C_{10}F_{21}COOH$	ABCR	96	562.9	**519.0**, 269.0	8, 18
PFDoA	$C_{11}F_{23}COOH$	Alfa Aesar	96	612.9	**568.9**, 269.0	10, 20
PFTrDA	$C_{12}F_{25}COOH$	Wellington Laboratories	>98	663.1	**618.9**, 169.0	11, 35
PFBS	$C_4F_9SO_2O^-$	Fluka	97	298.9	**79.8**, 99.0	33,31
PFHxS	$C_6F_{13}SO_2O^-$	Fluka	98	398.9	**79.8**, 99.0	38, 35
PFOS	$C_8F_{17}SO_2O^-$	Wellington Laboratories	>98	498.9	**79.7**, 99.0	48, 43
[$^{13}C_4$]-PFBA	[2,3,4-$^{13}C_3$]$F_7{}^{13}COOH$	Wellington Laboratories	>98	216.8	**171.8**	8
[$^{13}C_2$]-PFHxA	C_4F_9[2-^{13}C]$F_2{}^{13}COOH$	Wellington Laboratories	>98	314.9	**269.9**, 119.0	10, 15
[$^{13}C_4$]-PFOA	C_4F_9[2,3,4-$^{13}C_3$]$F_6{}^{13}COOH$	Wellington Laboratories	>98	416.9	**371.8**, 169.0	7, 15

Analyte	Formula	Supplier	Purity (%)	Precursor ion [*m*/*z*]	Product ion [*m*/*z*]	Collision energy (V)
[$^{13}C_5$]-PFNA	C_4F_9[2,3,4,5-$^{13}C_4$]$F_8{}^{13}$COOH	Wellington Laboratories	>98	467.9	**423.0**, 219.0	10, 16
[$^{13}C_2$]-PFDA	$C_8F_{17}{}^{13}CF_2{}^{13}$COOH	Wellington Laboratories	>98	514.9	**469.8**, 269.0	15, 17
[$^{13}C_2$]-PFUdA	$C_9F_{19}{}^{13}CF_2{}^{13}$COOH	Wellington Laboratories	>98	564.9	**519.8** 269.0	10, 18
[$^{13}C_4$]-PFOS	C_4F_9[1,2,3,4-$^{13}C_4$]$F_8SO_2O^-$	Wellington Laboratories	>98	502.9	**79.5**, 99.0	49,41

Note: product ions in bold font were used for quantification.

Table S12. Instrumental limits of detection (iLOD) and quantification (iLOQ), average blank levels, and method quantification limits (MQL) for water (pg L^{-1}). and suspended particle (pg g^{-1}) samples.

Analyte	iLOD (S/N=3)	iLOQ (S/N=10)	Mean procedural blanks of water samples	MQL for water samples	Mean field blanks of water samples	Mean procedural blanks of suspended particle samples	MQL of suspended particle samples	Mean field blanks of suspended particle samples
PFBA	0.3	4.2	0.9±0.7	3.0	12.1±1.6	3.2±1.4	10.6	11.8±1.7
PFPeA	0.2	9.4	0.5±0.4	1.5	1.1±0.3	0.8±0.6	3.2	3.8±0.7
PFHxA	0.3	3.2	0.6±0.2	1.2	1.2±0.4	1.0±0.2	1.6	2.0±0.6
PFHpA	0.2	5.7	0.7±0.4	2.0	1.3±0.4	0.5±0.4	1.7	0.8±0.4
PFOA	0.2	4.2	0.6±0.3	1.4	0.4±0.1	1.0±0.1	1.3	1.4±0.5
PFNA	0.1	5.7	0.5±0.3	1.5	1.3±0.2	1.0±0.1	1.3	2.6±1.4
PFDA	0.3	2.6	0.6±0.2	1.2	1.6±0.2	0.8±0.1	1.1	1.4±0.8
PFUdA	0.2	4.6	0.6±0.3	1.5	0.3±0.1	0.9±0.3	1.8	2.8±1.6
PFDoA	0.5	7.9	0.5±0.4	1.7	1.4±0.2	1.2±0.5	2.7	2.4±1.0
PFTrDA	0.1	1.0	1.1±0.1	1.4	0.9±0.7	0.8±0.5	2.3	1.6±0.8
PFBS	0.1	1.7	0.2±0.1	0.5	0.8±0.2	1.3±0.6	3.1	8.0±1.9
PFHxS	0.3	1.5	0.9±0.5	2.4	10.7±0.2	0.7±0.3	1.6	2.6±1.4
PFOS	0.1	4.3	0.2±0.1	0.6	0.2±0.1	1.8±0.5	3.2	9.4±1.9

Note: PFBA, perfluorobutanoic acid; PFPeA, perfluoropentanoic acid; PFHxA, perfluorohexanoic acid; PFHpA, perfluoroheptanoic acid; PFOA, perfluoro-octanoic acid; PFNA, perfluorononanoic acid; PFDA, perfluorodecanoic acid; PFUdA, perfluoroundecanoic acid; PFDoA, perfluorododecanoic acid; PFTrDA, perfluorotridecanoic acid; PFBS, perfluorobutane sulfonic acid; PFHxS, perfluorohexane sulfonic acid; and PFOS, perfluoro-octane sulfonic acid.

Table S13. Statistical recoveries for water and suspended particle samples.

Mass labeled compounds	Water (%)				Suspended particles (%)			
	Min.	Max.	Mean	SD	Min.	Max.	Mean	SD
[$^{13}C_4$]-PFBA	40	90	52	24	44	108	70	15
[$^{13}C_2$]-PFHxA	41	99	65	23	31	86	57	14
[$^{13}C_4$]-PFOA	37	106	72	22	25	85	51	15
[$^{13}C_4$]-PFOS	47	96	72	21	34	79	55	9
[$^{13}C_5$]-PFNA	34	121	70	21	28	80	50	13
[$^{13}C_2$]-PFDA	42	125	81	30	20	73	43	13
[$^{13}C_2$]-PFUdA	32	115	70	25	66	66	42	13

Note: Prior to extraction, samples were spiked with 2,000 pg of a recovery standard mix. The recoveries of each mass labeled compounds in different samples were assessed by comparing the peak areas to their initial values. [$^{13}C_4$]-PFBA, perfluoro-n-[1,2,3,4-$^{13}C_4$] butanoic acid; [$^{13}C_2$]-PFHxA, perfluoro-n-[1,2-^{13}C2] hexanoic acid; [$^{13}C_4$]-PFOA, perfluoro-n-[1,2,3,4-$^{13}C_4$] octanoic acid; [$^{13}C_4$]-PFOS, perfluoro-1-[1,2,3,4-$^{13}C_4$] octane sulfonate; [$^{13}C_5$]-PFNA, perfluoro-n-[1,2,3,4,5-$^{13}C_5$] nonanoic acid; [$^{13}C_2$]-PFDA, perfluoro-n-[1,2-$^{13}C_2$] decanoic acid; [$^{13}C_2$]-PFUdA, perfluoro-n-[1,2-$^{13}C_2$] undecanoic acid.

Table S14. Correlation analysis between logK_d and the influencing factors in glacial runoffs on the Tibetan Plateau.

Analyte	pH	Water temperature (T_w) (°C)	Particulate organic carbon (POC) (%)	Conductivity (σ) (μs cm^{-1})	Dissolved oxygen (DO) (mg L^{-1})
PFBA	0.311	0.498	**0.692****	−0.017	−0.287
PFPeA	0.200	0.183	**0.411***	−0.365	−0.036
PFHxA	0.363	0.239	**0.523****	−0.361	−0.052
PFHpA	0.410	−0.082	**0.453***	0.051	0.034
PFOA	0.184	0.033	0.245	−0.159	0.001
PFNA	0.290	0.157	**0.428***	−0.052	−0.099
PFDA	0.470	−0.242	0.267	−0.218	0.109
PFUdA	0.085	−0.079	0.197	−0.296	−0.016
PFDoA	−0.472	0.214	0.240	−0.607	−0.034
PFTrDA	−0.872	−0.331	0.024	−0.381	0.443
PFBS	0.502	**0.736****	**0.577****	0.541	0.298
PFHxS	−0.086	−0.093	0.214	−0.313	0.344
PFOS	0.436	−0.405	0.109	−0.174	0.146

Note: ** p <0.01; * p <0.05; PFBA, perfluorobutanoic acid; PFPeA, perfluoropentanoic acid; PFHxA, perfluorohexanoic acid; PFHpA, perfluoroheptanoic acid; PFOA, perfluoro-octanoic acid; PFNA, perfluorononanoic acid; PFDA, perfluorodecanoic acid; PFUdA, perfluoroundecanoic acid; PFDoA, perfluorododecanoic acid; PFTrDA, perfluorotridecanoic acid; PFBS, perfluorobutane sulfonic acid; PFHxS, perfluorohexane sulfonic acid; and PFOS, perfluoro-octane sulfonic acid.

Supplemental Figures

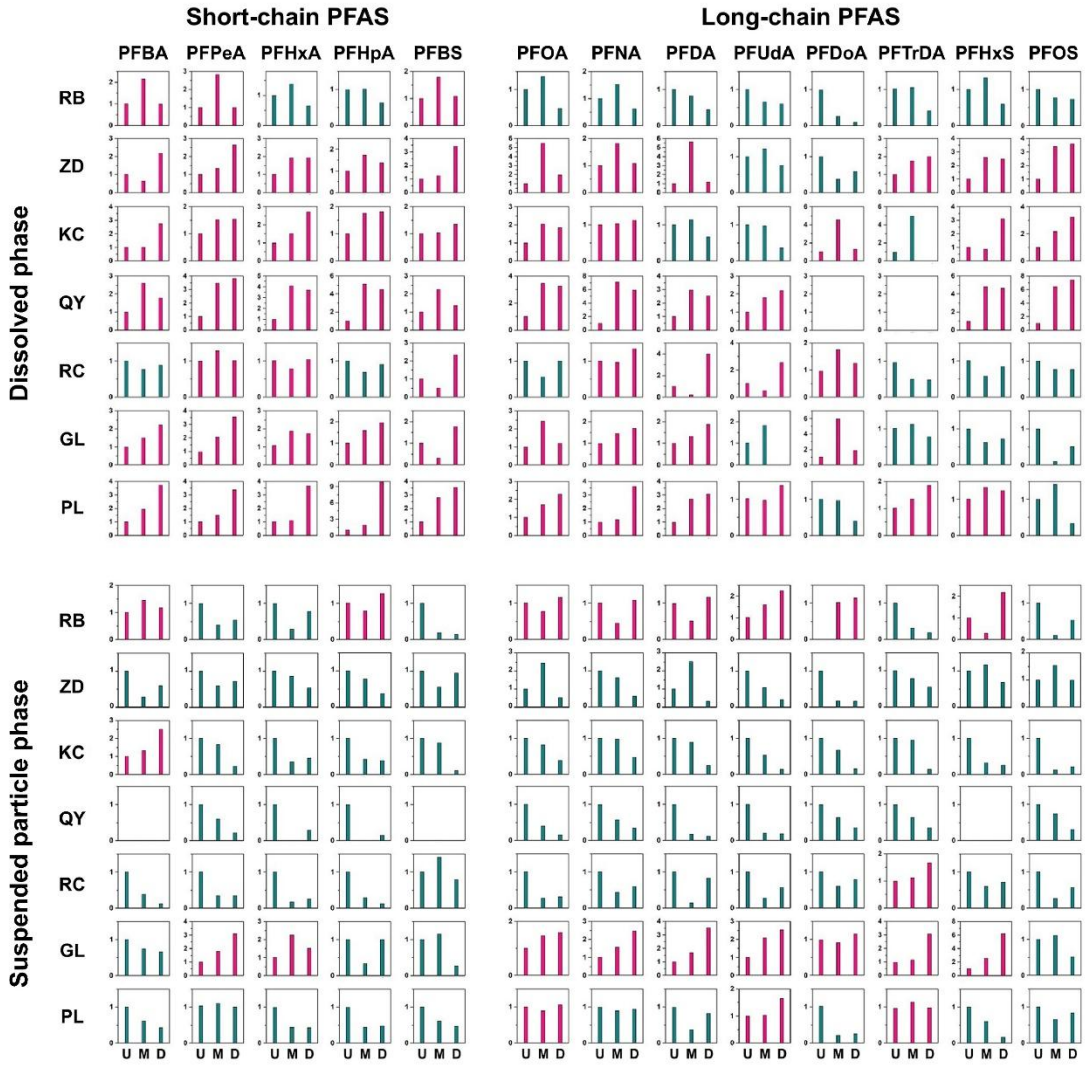

Figure S1. Dissolved and particle-bound perfluoroalkyl acids (PFAAs) in glacial runoff from upstream to downstream sites.

Note: The seven glacial regions are: RB, the Rongbuk glacier; KG, the Korchung Gangri glacier; ZD, the Zhadang glacier; GL, the Galongla glacier; PL, the Parlung No. 4 glacier; QY, the Qiangyong glacier; and RC, the Rijie Cojia glacier. U, M, and D represent the upstream, midstream, and downstream sampling sites, respectively. The ordinate represents the ratio of the PFAA concentration at each sampling site to the original concentration upstream. Pink represents an increasing trend from upstream to downstream, whereas dark green represents a decreasing trend. A null box (missing values) in QY indicates that the concentration of the individual PFAA in meltwater or suspended particles is below the limit of detection.

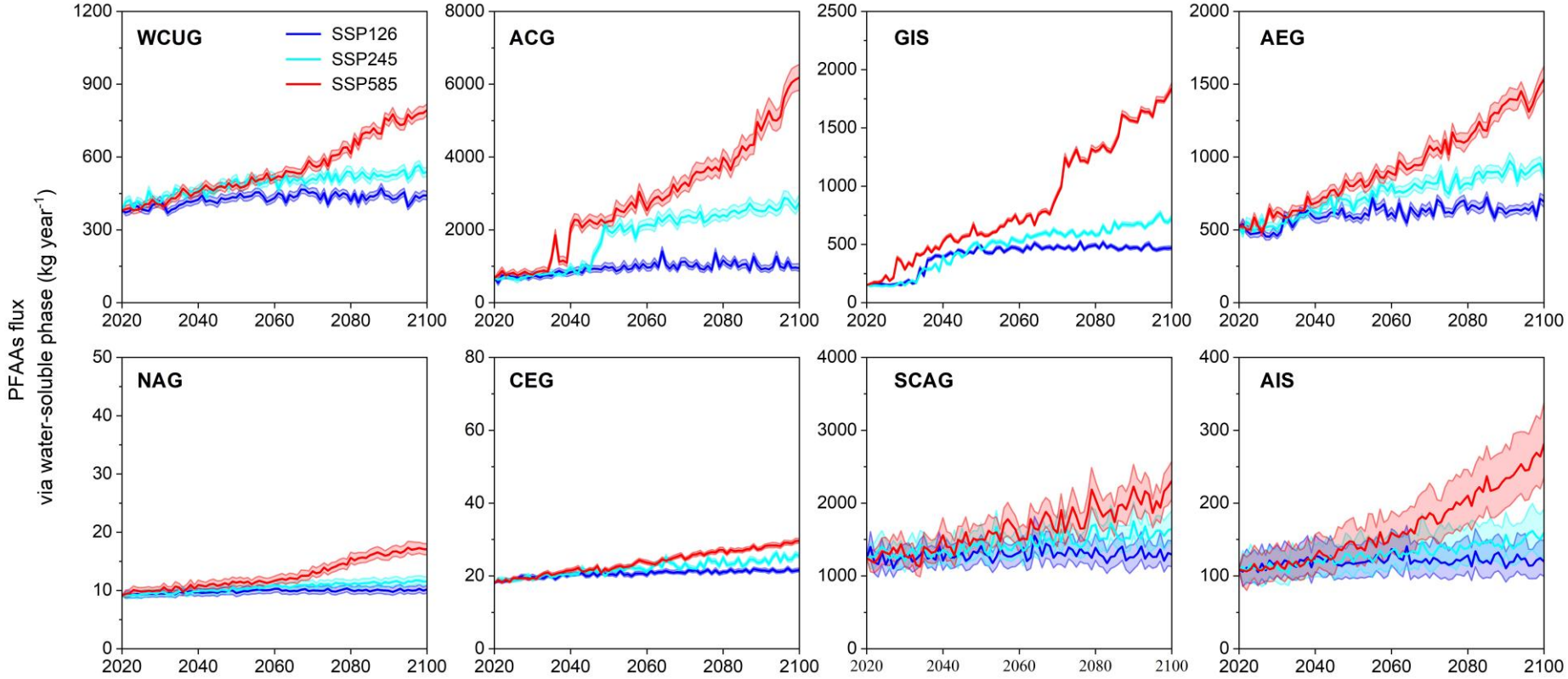

Figure S2. Annual release fluxes (kg year^{-1}) of PFAAs from glaciers in eight glacial regions via the water-soluble phase in 2020-2100 under three climate change scenarios (SSP126-blue line, SSP 245-bright blue line and SSP 585-red line).

Note: The solid line presents the average value with a window of one year and the shaded area indicates the range of minimum and maximum values. WCUG, West Canada and USA; ACG, Arctic Canada; GIS, the Greenland ice sheet; AEG, Arctic Europe; NAG, North Asia; CEG, Central Europe; SCAG, South and Central Asia; and AIS, the Antarctic and Subantarctic ice sheet.

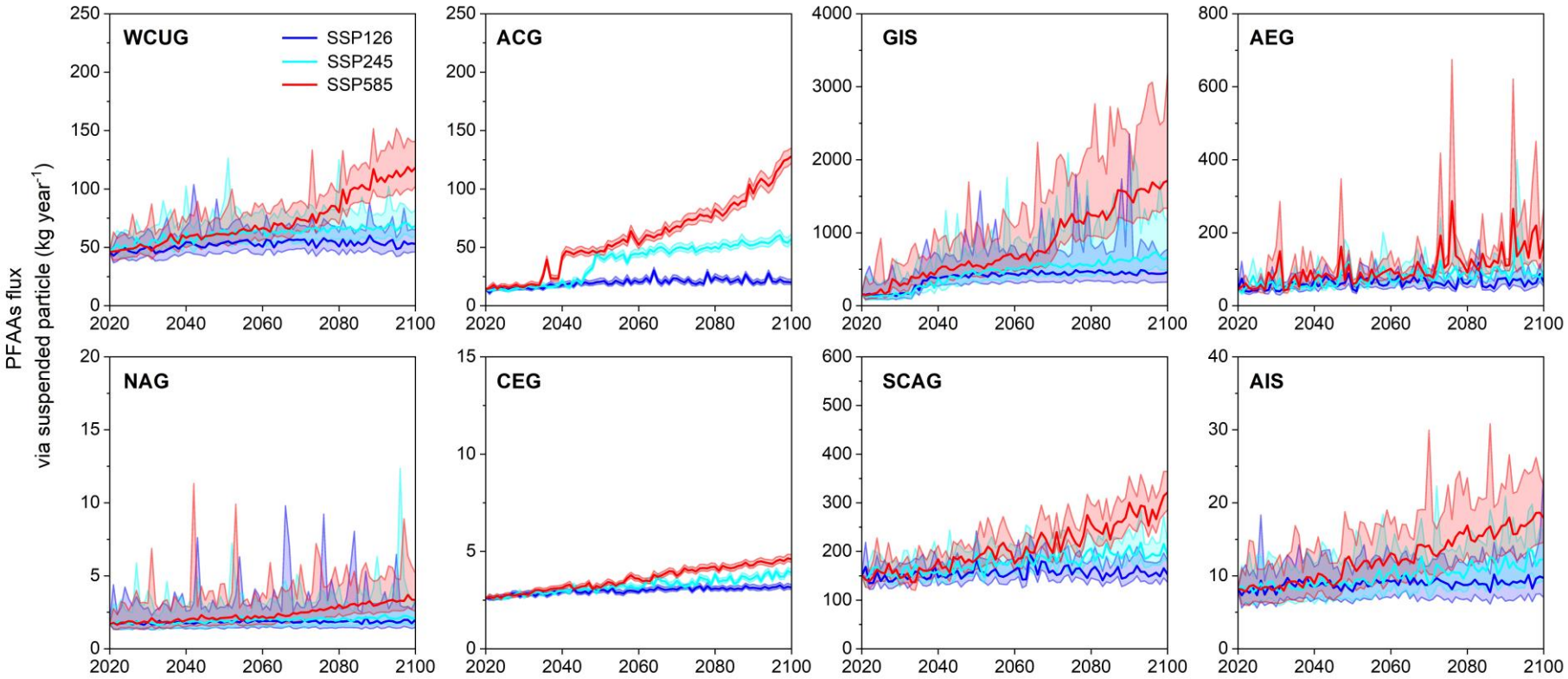

Figure S3. Annual release fluxes (kg year^{-1}) of PFAAs from glaciers in eight glacial regions via the suspended particles in 2020-2100 under three climate change scenarios (SSP126-blue line, SSP 245-bright blue line and SSP 585-red line).

Note: The solid line presents the average value with a window of one year and the shaded area indicates the range of minimum and maximum values. WCUG, West Canada and USA; ACG, Arctic Canada; GIS, the Greenland ice sheet; AEG, Arctic Europe; NAG, North Asia; CEG, Central Europe; SCAG, South and Central Asia; and AIS, the Antarctic and Subantarctic ice sheet.

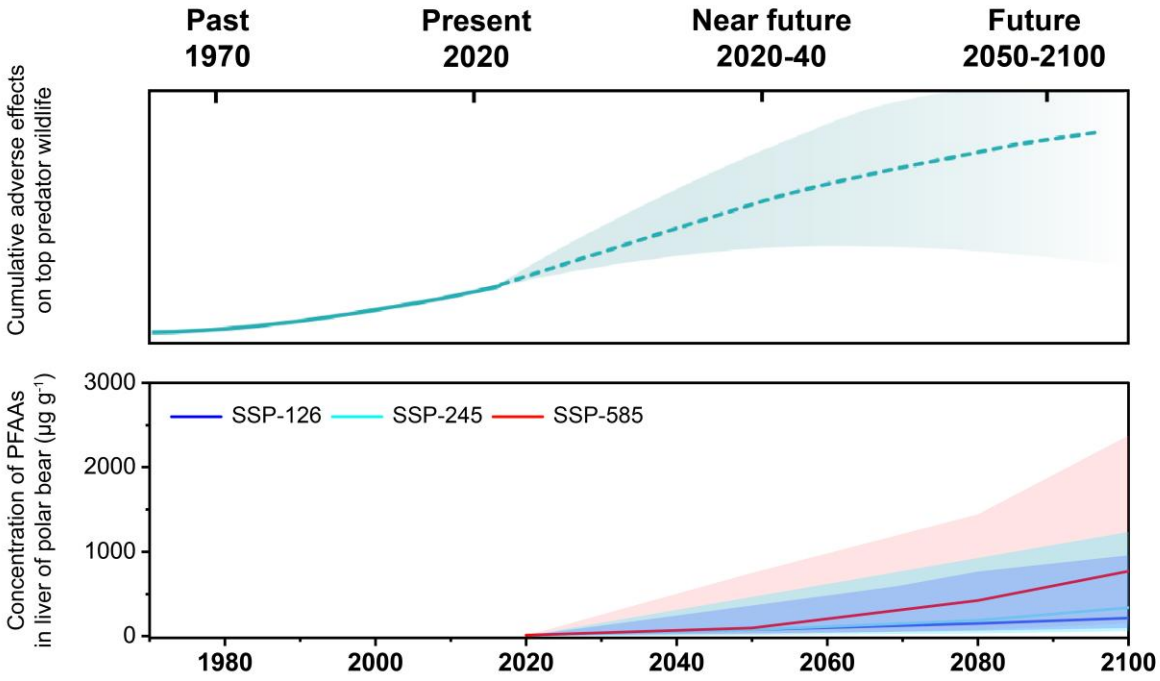

Figure S4. Projected changes in cumulative adverse effects on top predator wildlife and PFAA concentrations in polar bear for the period from 1970-2020 (past to present) and 2020-2100 (near future to future).

Note: The upper part is modified from the AMAP Assessment 2020 (available at AMAP Assessment 2020: POPs and Chemicals of Emerging Arctic Concern: Influence of Climate Change | AMAP)

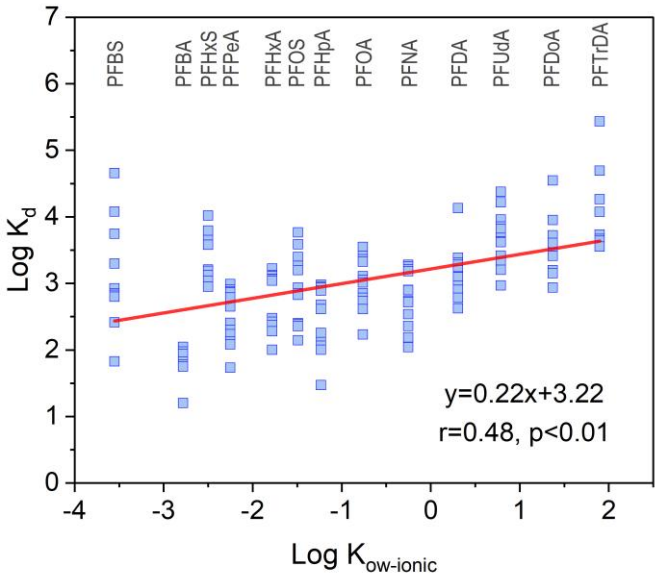

Figure S5. The correlations of log$K_{ow\text{-}ionic}$ and logK_d for individual PFAAs measured in meltwater on the Tibetan Plateau.

Note: PFBA, perfluorobutanoic acid; PFPeA, perfluoropentanoic acid; PFHxA, perfluorohexanoic acid; PFHpA, perfluoroheptanoic acid; PFOA, perfluoro-octanoic acid; PFNA, perfluorononanoic acid; PFDA, perfluorodecanoic acid; PFUdA, perfluoroundecanoic acid; PFDoA, perfluorododecanoic acid; PFTrDA, perfluorotridecanoic acid; PFBS, perfluorobutane sulfonic acid; PFHxS, perfluorohexane sulfonic acid; and PFOS, perfluoro-octane sulfonic acid.

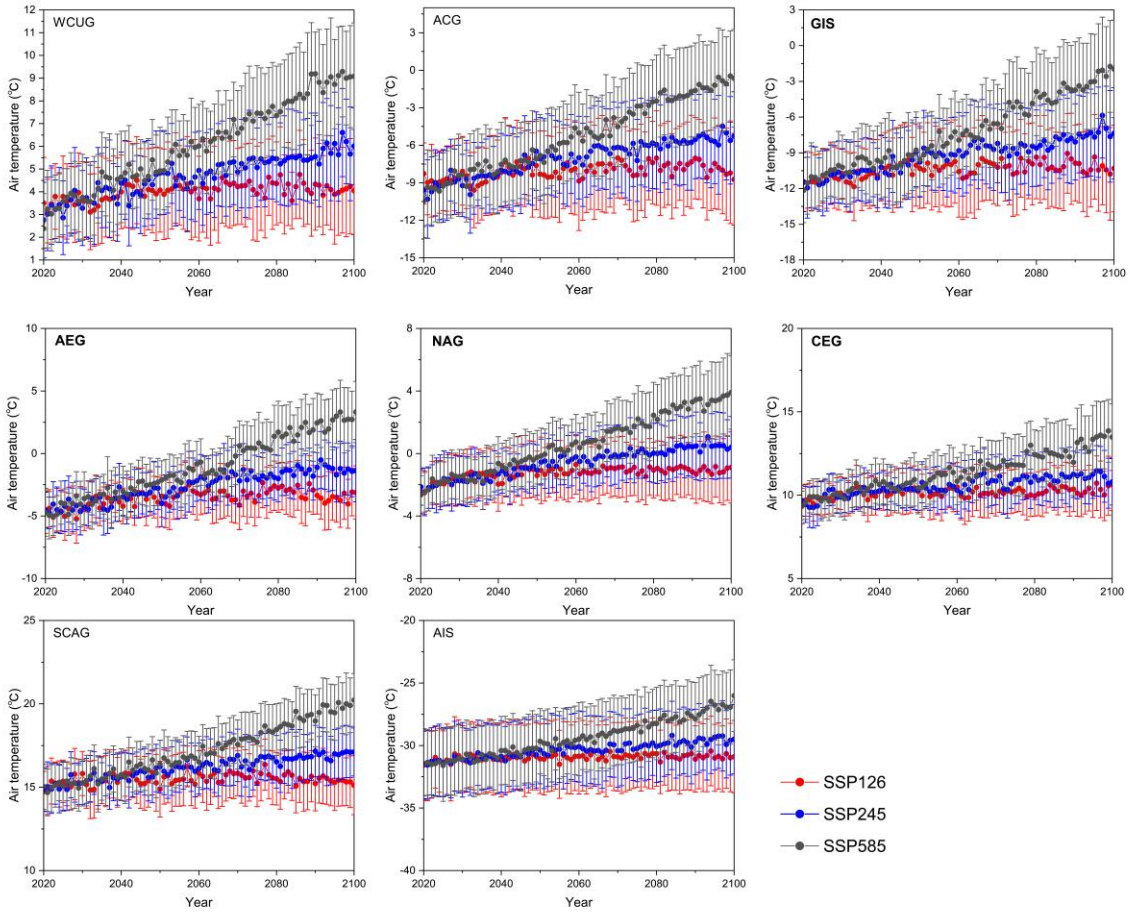

Figure S6. Annual air temperature in three scenarios from the 14 CMIP6 datasets for the eight glacial regions studied.

Note: WCUG, Western Canada and USA; ACG, Arctic Canada; GIS, Greenland ice sheet; AEG, Arctic Europe; NAG, North Asia; CEG, Central Europe; SCAG, South and Central Asia; AIS, Antarctic and Subantarctic ice sheet.

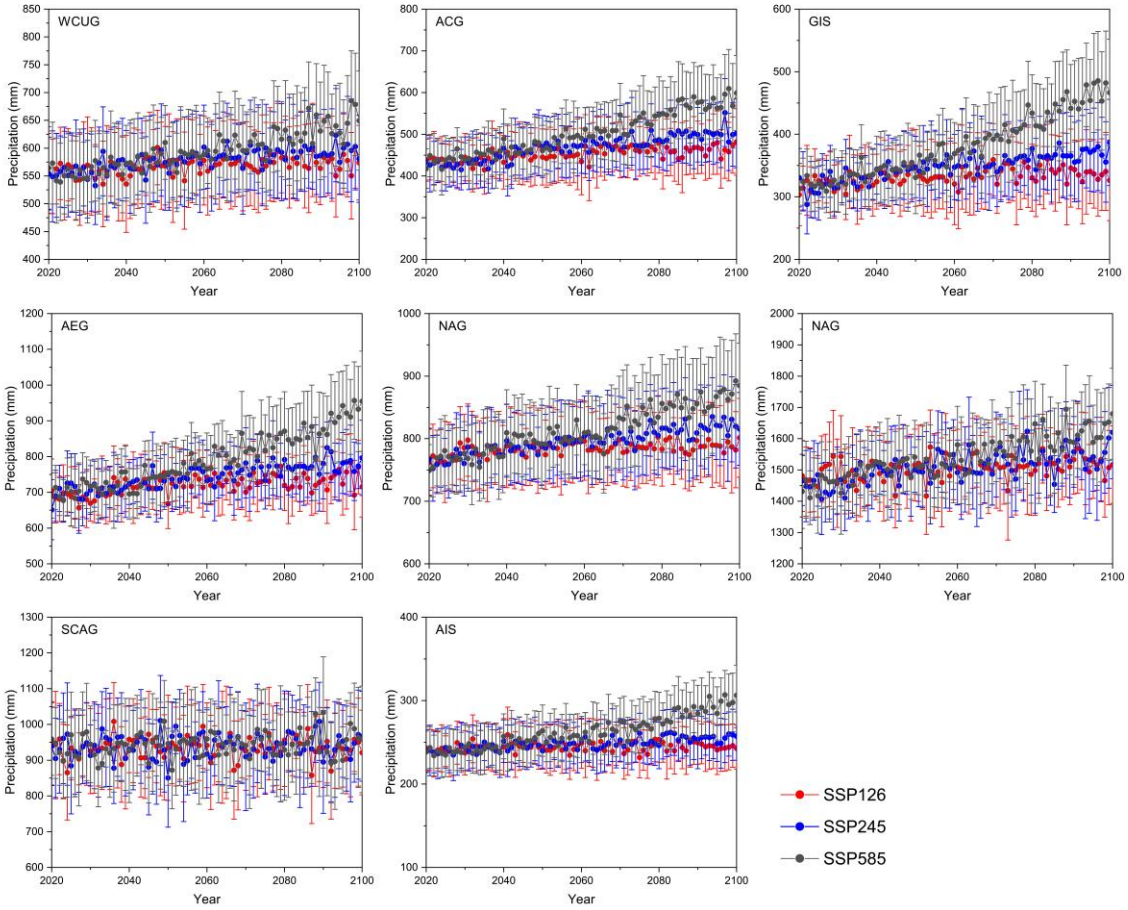

Figure S7. Annual precipitation in three scenarios from the 14 CMIP6 datasets for the eight glacial regions studied.

Note: WCUG, Western Canada and USA; ACG, Arctic Canada; GIS, Greenland ice sheet; AEG, Arctic Europe; NAG, North Asia; CEG, Central Europe; SCAG, South and Central Asia; AIS, Antarctic and Subantarctic ice sheet.

Supplemental References:

1. Zhao, P., Xia, X., Dong, J., Xia, N., Jiang, X., Li, Y., and Zhu, Y. (2016). Short- and long-chain perfluoroalkyl substances in the water, suspended particulate matter, and surface sediment of a turbid river. Sci. Total Environ. *568*, 57-65. https://doi.org/10.1016/j.scitotenv.2016.05.221.
2. Vrbka, L., and Jungwirth, P. (2005). Brine rejection from freezing salt solutions: A molecular dynamics study. Phys. Rev. Lett. *95*, 148501. https://doi.org/10.1103/PhysRevLett.95.148501.
3. Chen, M., Wang, C., Wang, X., Fu, J., Gong, P., Yan, J., Yu, Z., Yan, F., and Nawab, J. (2019). Release of perfluoroalkyl substances from melting glacier of the Tibetan Plateau: Insights into the impact of global warming on the cycling of emerging pollutants. J Geophys. Res. Atmos. *124*, 7442-7456. https://doi.org/10.1029/2019JD030566.
4. MacInnis, J.J., Lehnherr, I., Muir, D.C.G., Quinlan, R., and De Silva, A.O. (2019). Characterization of perfluoroalkyl substances in sediment cores from High and Low Arctic lakes in Canada. Sci. Total. Environ. *666*, 414-422. https://doi.org/10.1016/j.scitotenv.2019.02.210.
5. Gao, K., Zhuang, T.F., Liu, X., Fu, J.J., Zhang, J.X., Fu, J., Wang, L.G., Zhang, A.Q., Liang, Y., Song, M.Y., and Jiang, G.B. (2019). Prenatal exposure to per- and polyfluoroalkyl Substances (PFASs) and association between the placental transfer efficiencies and dissociation constant of serum proteins–PFAS complexes. Environ. Sci. Technol. *53*, 6529-6538. https://doi.org/10.1021/acs.est.9b00715.
6. Wang, X., Halsall, C., Codling, G., Xie, Z., Xu, B., Zhao, Z., Xue, Y., Ebinghaus, R., and Jones, K.C. (2014). Accumulation of perfluoroalkyl compounds in tibetan mountain snow: temporal patterns from 1980 to 2010. Environ. Sci. Technol. *48*, 173-181. https://doi.org/10.1021/es4044775.
7. Wong, F., Shoeib, M., Katsoyiannis, A., Eckhardt, S., Stohl, A., Bohlin-Nizzetto, P., Li, H., Fellin, P., Su, Y., and Hung, H. (2018). Assessing temporal trends and source regions of per-and polyfluoroalkyl substances (PFASs) in air under the Arctic Monitoring and Assessment Programme (AMAP). Atmos. Environ. *172*, 65-73. https://doi.org/10.1016/j.atmosenv.2017.10.028.
8. Yamashita, N., Taniyasu, S., Petrick, G., Wei, S., Gamo, T., Lam, P.K., and Kannan, K. (2008). Perfluorinated acids as novel chemical tracers of global circulation of ocean waters. Chemosphere *70*, 1247-1255. https://doi.org/10.1016/j.chemosphere.2007.07.079.
9. Muir, D., Gunnarsdóttir, M.J., Koziol, K., von Hippel, F.A., Szumińska, D., Ademollo, N., Corsolini, S., De Silva, A., Gabrielsen, G., and Kallenborn, R. (2025). Local sources versus long-range transport of organic contaminants in the Arctic: future developments related to climate change. Environ. Sci.: Adv. *4*, 355-408. https://doi.org/10.1039/D4VA00240G.
10. Sha, B., Johansson, J.H., Tunved, P., Bohlin-Nizzetto, P., Cousins, I.T., and Salter, M.E. (2021). Sea spray aerosol (SSA) as a source of perfluoroalkyl acids (PFAAs) to the atmosphere: field evidence from long-term air monitoring. Environ. Sci. Technol. *56*,

228-238. https://doi.org/10.1021/acs.est.1c04277.
11. Sha, B., Johansson, J.H., Salter, M.E., Blichner, S.M., and Cousins, I.T. (2024). Constraining global transport of perfluoroalkyl acids on sea spray aerosol using field measurements. Sci. Adv. *10*, eadl1026. https://doi.org/10.1126/sciadv.adl102.
12. Hidalgo, A., and Mora-Diez, N. (2015). Novel approach for predicting partition coefficients of linear perfluorinated compounds. Theor. Chem. Acc. *135*, 18. https://doi.org/10.1007/s00214-015-1784-6.
13. Yeung, L.W., Dassuncao, C., Mabury, S.A., Sunderland, E.M., Zhang, X.P., and Lohmann, R. (2017). Vertical profiles, sources, and transport of PFASs in the Arctic Ocean. Environ. Sci. Technol. *51*, 6735-6744. https://doi.org/10.1021/acs.est.7b00788.
14. Young, C.J., Furdui, V.I., Franklin, J., Koerner, R.M., Muir, D., and Mabury, S.A. (2007). Perfluorinated acids in Arctic snow: New evidence for atmospheric formation. Environ. Sci. Technol. *41*, 3455-3461. https://doi.org/10.1021/es0626234.
15. Muir, D., and Miaz, L.T. (2021). Spatial and temporal trends of perfluoroalkyl substances in global ocean and coastal waters. Environ. Sci. Technol. *55*, 9527-9537. https://doi.org/10.1021/acs.est.0c08035.
16. Loewen, M., Wania, F., Wang, F., and Tomy, G. (2008). Altitudinal transect of atmospheric and aqueous fluorinated organic compounds in Western Canada. Environ. Sci. Technol. *42*, 2374-2379. https://doi.org/10.1021/es702276c.
17. Pickard, H.M., Criscitiello, A.S., Spencer, C., Sharp, M.J., Muir, D.C.G., De Silva, A.O., and Young, C.J. (2018). Continuous non-marine inputs of per- and polyfluoroalkyl substances to the High Arctic: a multi-decadal temporal record. Atmos. Chem. Phys. *18*, 5045-5058. https://doi.org/10.5194/acp-18-5045-2018.
18. Veillette, J., Muir, D.C., Antoniades, D., Small, J.M., Spencer, C., Loewen, T.N., Babaluk, J.A., Reist, J.D., and Vincent, W.F. (2012). Perfluorinated chemicals in meromictic lakes on the northern coast of Ellesmere Island, High Arctic Canada. Arctic, 245-256. https://www.jstor.org/stable/41758932.
19. MacInnis, J., De Silva, A.O., Lehnherr, I., Muir, D.C., Pierre, K.A.S., Louis, V.L.S., and Spencer, C. (2022). Investigation of perfluoroalkyl substances in proglacial rivers and permafrost seep in a high Arctic watershed. Environ. Sci. Proc. Imp. *24*, 42-51. https://doi.org/10.1039/D1EM00349F.
20. MacInnis, J.J., Lehnherr, I., Muir, D.C., St. Pierre, K.A., St. Louis, V.L., Spencer, C., and De Silva, A.O. (2019). Fate and transport of perfluoroalkyl substances from snowpacks into a lake in the High Arctic of Canada. Environ. Sci. Technol. *53*, 10753-10762. https://doi.org/10.1021/acs.est.9b03372.
21. Pickard, H.M., Criscitiello, A.S., Persaud, D., Spencer, C., Muir, D.C., Lehnherr, I., Sharp, M.J., De Silva, A.O., and Young, C.J. (2020). Ice core record of persistent short-chain fluorinated alkyl acids: Evidence of the impact from global environmental regulations. Geophys. Res. Lett. *47*, e2020GL087535. https://doi.org/10.1029/2020GL087535.
22. Joerss, H., Xie, Z., Wagner, C.C., von Appen, W.J., Sunderland, E.M., and Ebinghaus, R. (2020). Transport of legacy perfluoroalkyl substances and the replacement compound HFPO-DA through the Atlantic Gateway to the Arctic Ocean-Is the Arctic a sink or a

source? Environ. Sci. Technol. *54*, 9958-9967. https://doi.org/10.1021/acs.est.0c00228.

23. Skaar, J.S., Raeder, E.M., Lyche, J.L., Ahrens, L., and Kallenborn, R. (2019). Elucidation of contamination sources for poly- and perfluoroalkyl substances (PFASs) on Svalbard (Norwegian Arctic). Environ. Sci. Pollut. Res. *26*, 7356-7363. https://doi.org/10.1007/s11356-018-2162-4.
24. Nguyen, M.A., Wiberg, K., Ribeli, E., Josefsson, S., Futter, M., Gustavsson, J., and Ahrens, L. (2017). Spatial distribution and source tracing of per- and polyfluoroalkyl substances (PFASs) in surface water in Northern Europe. Environ. Pollut. *220*, 1438-1446. https://doi.org/10.1016/j.envpol.2016.10.089.
25. Garnett, J., Halsall, C., Vader, A., Joerss, H., Ebinghaus, R., Leeson, A., and Wynn, P.M. (2021). High concentrations of perfluoroalkyl acids in arctic seawater driven by early thawing sea ice. Environ. Sci. Technol. *55*, 11049-11059. https://doi.org/10.1021/acs.est.1c01676.
26. Kwok, K.Y., Yamazaki, E., Yamashita, N., Taniyasu, S., Murphy, M.B., Horii, Y., Petrick, G., Kallerborn, R., Kannan, K., Murano, K., and Lam, P.K. (2013). Transport of perfluoroalkyl substances (PFAS) from an arctic glacier to downstream locations: implications for sources. Sci. Total Environ. *447*, 46-55. https://doi.org/10.1016/j.scitotenv.2012.10.091.
27. Ademollo, N., Spataro, F., Rauseo, J., Pescatore, T., Fattorini, N., Valsecchi, S., Polesello, S., and Patrolecco, L. (2021). Occurrence, distribution and pollution pattern of legacy and emerging organic pollutants in surface water of the Kongsfjorden (Svalbard, Norway): Environmental contamination, seasonal trend and climate change. Mar. Pollut. Bull. *163*, 111900. https://doi.org/10.1016/j.marpolbul.2020.111900.
28. Codling, G., Halsall, C., Ahrens, L., Del Vento, S., Wiberg, K., Bergknut, M., Laudon, H., and Ebinghaus, R. (2014). The fate of per- and polyfluoroalkyl substances within a melting snowpack of a boreal forest. Environ. Pollut. *191*, 190-198. https://doi.org/10.1016/j.envpol.2014.04.032.
29. Cai, M., Zhao, Z., Yin, Z., Ahrens, L., Huang, P., Cai, M., Yang, H., He, J., Sturm, R., Ebinghaus, R., and Xie, Z. (2012). Occurrence of perfluoroalkyl compounds in surface waters from the North Pacific to the Arctic Ocean. Environ. Sci. Technol. *46*, 661-668. https://doi.org/10.1021/es2026278.
30. Kirchgeorg, T., Dreyer, A., Gabrieli, J., Kehrwald, N., Sigl, M., Schwikowski, M., Boutron, C., Gambaro, A., Barbante, C., and Ebinghaus, R. (2013). Temporal variations of perfluoroalkyl substances and polybrominated diphenyl ethers in alpine snow. Environ. Pollut. *178*, 367-374. https://doi.org/10.1016/j.envpol.2013.03.043.
31. Kirchgeorg, T., Dreyer, A., Gabrielli, P., Gabrieli, J., Thompson, L., Barbante, C., and Ebinghaus, R. (2016). Seasonal accumulation of persistent organic pollutants on a high altitude glacier in the Eastern Alps. Environ. Pollut. *218*, 804-812. https://doi.org/10.1016/j.envpol.2016.08.004.
32. Miner, K.R., Clifford, H., Taruscio, T., Potocki, M., Solomon, G., Ritari, M., Napper, I.E., Gajurel, A.P., and Mayewski, P.A. (2021). Deposition of PFAS 'forever chemicals' on Mt. Everest. Sci. Total Environ. *759*, 144421. https://doi.org/10.1016/j.scitotenv.2020.144421.

33. Wang, X., Chen, M., Gong, P., and Wang, C. (2019). Perfluorinated alkyl substances in snow as an atmospheric tracer for tracking the interactions between westerly winds and the Indian Monsoon over western China. Environ. Int. *124*, 294-301. https://doi.org/10.1016/j.envint.2018.12.057.
34. Casal, P., Zhang, Y.F., Martin, J.W., Pizarro, M., Jimenez, B., and Dachs, J. (2017). Role of snow deposition of perfluoroalkylated substances at coastal Livingston Island (Maritime Antarctica). Environ. Sci. Technol. *51*, 8460-8470. https://doi.org/10.1021/acs.est.7b02521.
35. Cai, M., Yang, H., Xie, Z., Zhao, Z., Wang, F., Lu, Z., Sturm, R., and Ebinghaus, R. (2012). Per- and polyfluoroalkyl substances in snow, lake, surface runoff water and coastal seawater in Fildes Peninsula, King George Island, Antarctica. J. Hazard. Mater. *209-210*, 335-342. https://doi.org/10.1016/j.jhazmat.2012.01.030.
36. Xie, Z.Y., Wang, Z., Magand, O., Thollot, A., Ebinghaus, R., Mi, W.Y., and Dommergue, A. (2020). Occurrence of legacy and emerging organic contaminants in snow at Dome C in the Antarctic. Sci. Total Environ. *741*, 140200. https://doi.org/10.1016/j.scitotenv.2020.140200.
37. Shan, G., Xiang, Q., Feng, X., Wu, W., Yang, L., and Zhu, L. (2021). Occurrence and sources of per- and polyfluoroalkyl substances in the ice-melting lakes of Larsemann Hills, East Antarctica. Sci. Total Environ. *781*, 146747. https://doi.org/10.1016/j.scitotenv.2021.146747.
38. Wu, J., Zhuang, Y., Dong, B., Wang, F., Yan, Y., Zhang, D., Liu, Z., Duan, X., Bo, Y., and Peng, L. (2024). Spatial heterogeneity of per-and polyfluoroalkyl substances caused by glacial melting in Tibetan Lake Nam Co due to global warming. J. Hazard. Mater. *478*, 135468. https://doi.org/10.1016/j.jhazmat.2024.135468.
39. Chen, Y., Wei, L., Luo, W., Jiang, N., Shi, Y., Zhao, P., Ga, B., Pei, Z., Li, Y., and Yang, R. (2023). Occurrence, spatial distribution, and sources of PFASs in the water and sediment from lakes in the Tibetan Plateau. J. Hazard. Mater. *443*, 130170. https://doi.org/10.1016/j.jhazmat.2022.130170.
40. Zhang, X., Hu, T., Yang, L., and Guo, Z. (2018). The investigation of perfluoroalkyl substances in seasonal freeze–thaw rivers during spring flood period: a case study in Songhua River and Yalu River, China. B. Environ. Contam. Tox. *101*, 166-172. https://doi.org/10.1007/s00128-018-2381-x.
41. Cao, Y., Cao, X., Wang, H., Wan, Y., and Wang, S. (2015). Assessment on the distribution and partitioning of perfluorinated compounds in the water and sediment of Nansi Lake, China. Environ. Monit. Assess. *187*, 1-9. https://doi.org/10.1007/s10661-015-4831-9.
42. Mussabek, D., Ahrens, L., Persson, K.M., and Berndtsson, R. (2019). Temporal trends and sediment–water partitioning of per-and polyfluoroalkyl substances (PFAS) in lake sediment. Chemosphere *227*, 624-629.
43. Li, J., Li, X., Zhu, Y., Wang, L., Ren, S., An, R., Zhang, Q., and Wang, G. (2025). The first survey of legacy and emerging per-and polyfluoroalkyl substances (PFAS) in Hulun Lake, China: Occurrence, sources, and environmental impacts. Emerg. Contam. *11*, 100431. https://doi.org/10.1016/j.emcon.2024.100431.

44. Oliver, D.P., Navarro, D.A., Baldock, J., Simpson, S.L., and Kookana, R.S. (2020). Sorption behaviour of per-and polyfluoroalkyl substances (PFASs) as affected by the properties of coastal estuarine sediments. Sci. Total Environ. *720*, 137263. https://doi.org/10.1016/j.scitotenv.2020.137263.
45. Li, W., Liu, X., Mao, H., and Wang, S. (2023). Concentration, distribution, and bioconcentration of short-and long-chain perfluoroalkyl substances in the water, suspended particulate matter, and surface sediment of a typical semi-enclosed bay. Sci. Total Environ. *890*, 164416. https://doi.org/10.1016/j.scitotenv.2023.164416.
46. Saritha, V., Krishnan, K., and Mohan, M. (2023). Perfluorooctanoic acid in the sediment matrices of Arctic fjords, Svalbard. Mar. Pollut. Bull. *192*, 115061. https://doi.org/10.1016/j.marpolbul.2023.115061.
47. Boitsov, S., Bruvold, A., Hanssen, L., Jensen, H.K., and Ali, A. (2024). Per-and polyfluoroalkyl substances (PFAS) in surface sediments of the North-east Atlantic Ocean: A non-natural PFAS background. Environ. Adv. *16*, 100545. https://doi.org/10.1016/j.envadv.2024.100545.
48. Kahkashan, S., Wang, X., Chen, J., Bai, Y., Ya, M., Wu, Y., Cai, Y., Wang, S., Saleem, M., and Aftab, J. (2019). Concentration, distribution and sources of perfluoroalkyl substances and organochlorine pesticides in surface sediments of the northern Bering Sea, Chukchi Sea and adjacent Arctic Ocean. Chemosphere *235*, 959-968. https://doi.org/10.1016/j.chemosphere.2019.06.219.
49. Lin, Y., Jiang, J.-J., Rodenburg, L.A., Cai, M., Wu, Z., Ke, H., and Chitsaz, M. (2020). Perfluoroalkyl substances in sediments from the Bering Sea to the western Arctic: Source and pathway analysis. Environ. Int. *139*, 105699. https://doi.org/10.1016/j.envint.2020.105699.
50. Thackray, C.P., Selin, N.E., and Young, C.J. (2020). A global atmospheric chemistry model for the fate and transport of PFCAs and their precursors. Environ. Sci. Proc. Imp. *22*, 285-293. https://doi.org/10.1039/c9em00326f.
51. Garnett, J., Halsall, C., Winton, H., Joerss, H., Mulvaney, R., Ebinghaus, R., Frey, M., Jones, A., Leeson, A., and Wynn, P. (2022). Increasing accumulation of perfluorocarboxylate contaminants revealed in an Antarctic Firn Core (1958–2017). Environ. Sci. Technol. *56*, 11246-11255. https://doi.org/10.1021/acs.est.2c02592.